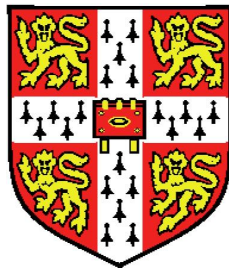


# Theoretical study of polar complex oxide heterostructures



Nicholas C. Bristowe

Selwyn College

University of Cambridge

This dissertation is submitted for the degree of

*Doctor of Philosophy*



## Declaration

This dissertation is the result of my own work and includes nothing which is the outcome of work done in collaboration except where specifically indicated in the text.

The limit on length prescribed by the Department of Physics Degree Committee, University of Cambridge, is not exceeded by this thesis.

## Acknowledgements

There are several people who have been involved in this research, providing much appreciated academic and technical advice for me over the past three and a half years. My supervisors Peter Littlewood and Emilio Artacho cannot be thanked enough for their excellent supervision and encouragement. Without their support and guidance this thesis would not have been possible.

I would like to thank Massimiliano Stengel and especially Miguel Pruneda for hosting me during my research visit to UAB (Barcelona, Spain) for a total duration of 3 months. In addition thanks to Thomas Fix, Mark Blamire and Frank Schoofs from the Materials Science Department (Cambridge, UK) for a productive collaboration.

The Engineering and Physical Sciences Research Council, Selwyn College and HPC Europa 2 are acknowledged for their financial support. CamGRID and the HPC facilities in Cambridge, the Spanish Supercomputer Network and HPC Europa are acknowledged for the use of their computing resources. Mark Calleja deserves particular mention for his technical support using CamGRID.

My family and friends deserve a special mention for their unfaltering encouragement and generosity throughout. A heartfelt thanks to Olivia Haddow for her selfless support and unfailing kindness.

Finally I would like to acknowledge insightful scientific discussions with H. Y. Hwang, J. F. Scott, G. Catalan, N. D. Mathur, J. Junquera, W. E. Pickett, M. A. Carpenter, S A T Redfern, P Ordejón, D Vanderbilt, J. Iñiguez, M. Bibes, V. Garcia, X. Moya, C. Ocal, S. Kalinin and S. Streiffer.

# Abstract

The wide range of physical properties exhibited in complex oxides make them an attractive option for scientific investigation and device applications. Interfaces between these oxides can introduce novel phenomena absent in the bulk of each material. An example is the electrically conducting interface between  $\text{LaAlO}_3$  (LAO) and  $\text{SrTiO}_3$  (STO), both insulators in bulk form. The interface conductivity is quasi-two-dimensional (a 2DEG) and under certain conditions magnetic and/or superconducting, however its origin is still debated.

This thesis aims to provide helpful guidelines, using basic theoretical principles, towards understanding the possible origins of the 2DEG in LAO/STO. First principles calculations of a model system, elucidate the importance of polarisation and electrostatics in these heterostructures. The net charge at the LAO-STO interface is argued to be precisely as what one would obtain by taking the formal charges of the ions, irrespective of covalency, and despite both materials being centrosymmetric. The interfacial net charge, or equivalently the LAO formal polarisation, requires charge screening which calculations show can be possible via an electronic transfer between neighbouring interfaces. It is additionally predicted that the LAO polarisation can induce one-dimensional electron gasses at the step edges of vicinal LAO-STO systems. The polarisation and electronic screening arguments for these perovskites, are shown to extend to very different materials with different symmetries, specifically two dimensional honeycomb compounds.

Finally the effects of surface defects are explored in thin films of LAO, and a prototypical ferroelectric,  $\text{BaTiO}_3$  (BTO). Surface redox processes such as oxygen vacancies, induced by the electric field within the film, can donate electrons to the buried interface, screening the polarisation charges. This process is found to be favourable for both systems, and is argued to be the likely origin of the 2DEG at the LAO-STO interface, and the origin of ferroelectric stability and tunnelling electroresistance at a BTO heterostructure in agreement with experiments.

## Publications arising from this thesis

- **N. C. Bristowe**, E. Artacho and P. B. Littlewood, *Phys. Rev. B* **80** (2009) 045425 “Oxide superlattices with alternating  $n$  and  $p$  interfaces” (Chapter 4)
- **N. C. Bristowe**, P. B. Littlewood and E. Artacho, *J. Phys.:Condens. Matter* **23** (2011) 081001 “The net charge at interfaces between insulators” (Chapter 3)
- **N. C. Bristowe**, P. B. Littlewood and E. Artacho, *Phys. Rev. B* **83** (2011) 205405 “Surface defects and conduction in polar oxide heterostructures” (Chapter 7)
- **N. C. Bristowe**, M. Stengel, P. B. Littlewood, J. M. Pruneda and E. Artacho, *Phys. Rev. B* **85** (2012) 024106 “Electrochemical ferroelectric switching: Origin of polarization reversal in ultrathin films” (Chapter 8)
- **N. C. Bristowe**, T. Fix, M. Blamire, P.B. Littlewood and E. Artacho, *Phys. Rev. Lett.* **108** (2012) 166802 “Proposal of a one-dimensional electron gas in the steps at the  $\text{LaAlO}_3$ - $\text{SrTiO}_3$  interface” (Chapter 5)
- A. Kumar, S. Jesse, C. W. Bark, **N. C. Bristowe**, E. Artacho, P. B. Littlewood, C. Eom, S. Kalinin, *ACS Nano* **6** (2012) 3841 “Probing surface and bulk electrochemical processes on the  $\text{LaAlO}_3$ - $\text{SrTiO}_3$  interface” (Chapters 7 and 8 aided discussions for this publication)

# Contents

<b>1</b>	<b>Introduction</b>	<b>1</b>
1.1	Oxides, interfaces and polarity . . . . .	2
1.1.1	Perovskites and derivatives . . . . .	2
1.1.2	Ferroelectrics . . . . .	4
1.1.3	Interfaces . . . . .	9
1.2	The $\text{LaAlO}_3/\text{SrTiO}_3$ interface . . . . .	14
1.2.1	Interface transport and the polar catastrophe . . . . .	14
1.2.2	The role of oxygen partial pressure . . . . .	16
1.2.3	$\text{LaAlO}_3$ thickness dependence . . . . .	17
1.2.4	Field effects . . . . .	21
1.2.5	Electronic properties . . . . .	22
1.2.6	Possible origins . . . . .	24
1.3	Aims and Objectives . . . . .	27
<b>2</b>	<b>Theoretical Methods</b>	<b>31</b>
2.1	Density functional theory . . . . .	32
2.1.1	The Kohn-Sham Formalism . . . . .	32
2.1.2	Basis set . . . . .	35
2.1.3	The pseudopotential approximation . . . . .	36
2.1.4	Periodic solids . . . . .	37
2.1.5	Ionic forces and the Hellmann-Feynman theorem . . . . .	37
2.2	Theory of polarisation . . . . .	38

## CONTENTS

---

2.2.1	Problem with Clausius-Mossotti . . . . .	38
2.2.2	Polarisation as an adiabatic flow of current . . . . .	39
2.2.3	Berry phase theory of polarisation . . . . .	40
2.2.4	Mapping on to Wannier centres . . . . .	42
2.2.5	Polarisation as a multivalued vector - the quantum . . . . .	43
<b>3</b>	<b>The net charge at interfaces between insulators</b>	<b>45</b>
3.1	Introduction . . . . .	46
3.2	Basic argument . . . . .	46
3.3	Formal discussion . . . . .	48
3.3.1	Symmetry considerations . . . . .	51
3.4	Formal versus effective polarisation . . . . .	51
3.4.1	Polarisation quanta and symmetry . . . . .	52
3.5	Further implications . . . . .	53
3.5.1	Non-centrosymmetric non-ferroelectric materials . . . . .	53
3.5.2	Polarisation quanta and relative polarisation . . . . .	53
3.5.3	Interface effects . . . . .	54
3.5.3.1	Internal rearrangements: intermixing . . . . .	54
3.5.3.2	Extrinsic processes: non-stoichiometry . . . . .	57
3.6	Final remarks and conclusions . . . . .	57
<b>4</b>	<b>Oxide superlattices with alternating <math>n</math> and <math>p</math> interfaces</b>	<b>59</b>
4.1	Introduction and methods . . . . .	60
4.2	Results and discussion . . . . .	62
4.2.1	Model of charged plates . . . . .	65
4.2.2	Chemical charge at interfaces . . . . .	68
4.2.3	Insulator to metal transition . . . . .	68
4.2.4	Extending the model to other systems . . . . .	70
4.3	Final remarks and summary . . . . .	71

<b>5</b>	<b>Proposal of a one-dimensional electron gas in the steps at the LaAlO<sub>3</sub>-SrTiO<sub>3</sub> interface</b>	<b>73</b>
5.1	Introduction . . . . .	74
5.2	Results and discussion . . . . .	76
5.2.1	Polarisation model . . . . .	76
5.2.2	DFT calculations . . . . .	77
5.2.3	Charge transfer model . . . . .	80
5.2.4	Phases of the electron gas . . . . .	82
5.3	Final remarks and conclusions . . . . .	83
<b>6</b>	<b>Polarisation classes of two-dimensional honeycomb compounds</b>	<b>85</b>
6.1	Introduction . . . . .	86
6.2	Results and discussion . . . . .	87
6.2.1	Polarisation classes . . . . .	87
6.2.2	Superlattices . . . . .	89
6.3	Final remarks and conclusions . . . . .	94
<b>7</b>	<b>Surface defects and conduction in polar oxide heterostructures</b>	<b>97</b>
7.1	Introduction . . . . .	98
7.2	Model . . . . .	101
7.3	Discussion . . . . .	103
7.3.1	Interface carrier density . . . . .	103
7.3.2	Electric field in LAO: pinning of potential drop . . . . .	105
7.3.3	Onset of conduction: electron trapping . . . . .	105
7.4	Final remarks and conclusions . . . . .	107
7.5	Model parameters . . . . .	108
7.5.1	The vacancy-vacancy interaction term, $\alpha$ . . . . .	108
7.5.2	The dielectric constant, $\epsilon$ . . . . .	109
7.5.3	The surface/interface chemistry term, $C$ . . . . .	109

## CONTENTS

---

<b>8</b>	<b>Chemical and electrochemical ferroelectric switching</b>	<b>111</b>
8.1	Introduction . . . . .	112
8.2	Methods . . . . .	114
8.3	Discussion . . . . .	115
8.3.1	The pristine system . . . . .	115
8.3.2	Chemical switching . . . . .	117
8.3.3	Electrochemical switching . . . . .	118
8.3.4	Magnetoelectric coupling . . . . .	120
8.3.5	Tunneling Electroresistance . . . . .	121
8.4	Conclusions . . . . .	123
8.5	Structural details . . . . .	124
<b>9</b>	<b>Conclusions and outlook</b>	<b>129</b>

# Chapter 1

## Introduction

### Chapter Summary

Complex oxides display a wide variety of physical properties, from insulating to superconducting, paraelectric to ferroelectric and non-magnetic to ferromagnetic. In some cases the order parameters associated with these properties are coupled, offering further functionality such as colossal magnetoresistance, and magnetoelectricity. Often only subtle alterations in structure, chemistry or external parameters can drive the system between these various phases. This makes complex oxide materials an appealing area for scientific investigation and device applications. Ongoing advances in epitaxial growth of oxides allows for even further possibilities by growth of multifunctional heterostructures. In some cases, novel and unexpected interfacial phenomena of two-dimensional character is observed, such as the two-dimensional electron gas (2DEG) at an interface between two band insulators,  $\text{LaAlO}_3$  (LAO) and  $\text{SrTiO}_3$  (STO). This chapter introduces a small selection of bulk and interfacial properties of complex oxides, with a particular interest on the effects of polarisation in heterostructured systems, including the LAO-STO interface.

### 1.1 Oxides, interfaces and polarity

#### 1.1.1 Perovskites and derivatives

Transition metal oxides range from the simplest binary monoxides, to more complex ternary and higher order structures. Possibly the most widely studied family is the perovskite structure with chemical formula  $ABX_3$ . The name perovskite originates with the mineral  $CaTiO_3$  first discovered in 1839 and named after the mineralogist Perovski. The ideal cubic-symmetry oxide perovskite structure can be viewed as a body centre B cation inside an octahedral cage of O (forming the face centres), with the A cation occupying the cube corners (see figure 1.1). The environment and role of the A and B cations are very different. The B cation can be a transition metal with its  $d$  electrons bonding with  $p$  electrons from the six neighbouring oxygens. The A cation is usually a non-transition metal which provides the necessary number of electrons for these bonds. Hence there exists a mixture of covalent bonding between B and O, and ionic bonding between A and B-O units.

The ideal cubic structure is unstable towards several types of symmetry lowering structural distortions. In many cases this is due to the stringent requirement of the A and B relative ionic sizes. This can be described by the Goldschmidt tolerance,

$$t = \frac{r_A + r_O}{\sqrt{2}(r_B + r_O)} \quad (1.1)$$

where  $r_A$ ,  $r_B$  and  $r_O$  are the ionic radii of A, B and O respectively. If the tolerance factor is 1 the ionic radii of O just touch the cations and the structure is expected to adopt the ideal cubic structure. When  $r_A$  is smaller than ideal and hence the tolerance factor is less than 1, the system is unstable towards rotations of neighbouring  $BO_6$  octahedra in opposite directions (see figure 1.1). These so-called antiferrodistortive rotations (AFD) appear in order to fill space left by the smaller than ideal A cation as in for example  $CaTiO_3$ . Various possible rotation patterns are described in, for example, ref. (1). If instead  $r_B$  is smaller

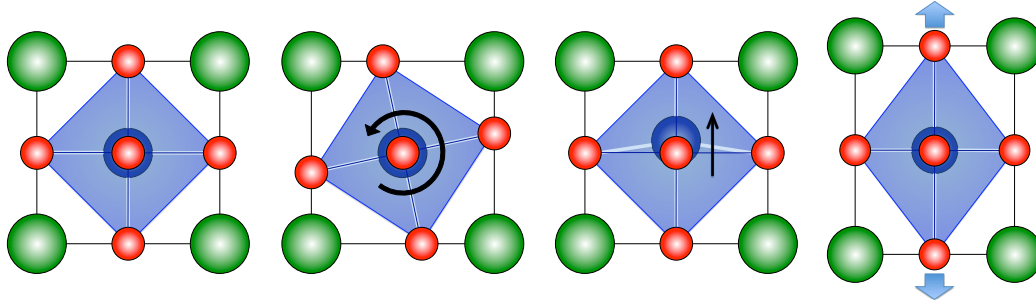


Figure 1.1: A schematic of the perovskite unit cell projected on to (100) and some example structural distortions. From left to right the illustrations represent the ideal cubic perovskite structure, an antiferrodistortive octahedra rotation (only one cell is shown), a ferroelectric-type and finally a Jahn-Teller-type distortion. Red, green and blue circles represent oxygen, and A and B cations respectively. The light blue shape represents the oxygen octahedra cage.

than ideal and hence the tolerance factor is larger than 1, the B cations will prefer to move off-centre (see figure 1.1). This is the case when Ca is replaced by Ba to form  $\text{BaTiO}_3$ . These two distortions, octahedra rotations and B-site off-centring, play an important role in determining the physical properties of these perovskite derivatives. The octahedra rotations lead to a reduction in the B-O-B bond angle from  $180^\circ$  that can affect the magnetic and transport properties. For example the magnetic superexchange mechanisms in manganites is known to depend strongly on this bond angle (2; 3). B-site off-centring is the manifestation of the polar distortion in  $\text{BaTiO}_3$  and several other perovskites<sup>1</sup>. The off-centring induces a dipole which aligns between unit cells producing a spontaneous macroscopic polarisation. Ferroelectrics will be discussed in further detail in the next section. It should be noted that the tolerance factor should be used for only semi-quantitative estimates of perovskite structures since it is based on ionic radii and perovskites are known to have mixed covalent character as mentioned above.

A third common structural distortion in perovskites, called a Jahn-Teller dis-

<sup>1</sup>In fact the term ferroelectricity was first used after the discovery of the effect in  $\text{BaTiO}_3$  (4).

## 1. INTRODUCTION

---

tortion, appears not because of size mismatch but instead due to an orbital degeneracy. In perovskites the octahedral crystal field and  $pd$  hybridisation splits the five  $3d$  B cation states into two; a doubly degenerate  $e_g$  and a triply degenerate  $t_{2g}$ . The two  $e_g$  states whose charge density point along directions towards the O anions lie in a higher energy than the three  $t_{2g}$ . In several  $3d$  systems an orbital degeneracy exists, for example in  $\text{LaMnO}_3$  with electronic configuration  $t_{2g}^3 e_g^1$  where the  $e_g$  electron can occupy any linear combination of the two orbitals ( $x^2 - y^2$  and  $3z^2 - r^2$ ). The Jahn-Teller theorem allows this degeneracy to be lifted by a symmetry reduction. Certain structural distortions to the octahedral cage can lift this degeneracy and lower the energy of the system. These distortions are called Jahn-teller distortions and usually lead to tetragonal or orthorhombic symmetry (see figure 1.1). Jahn-Teller effects play a role in, for example, electron-phonon coupling and orbital ordering in manganites.

### 1.1.2 Ferroelectrics

We now take a slightly closer look at ferroelectric perovskites since it provides an opportunity to introduce the concept of polarisation, which will be important for discussions of the  $\text{LaAlO}_3$ - $\text{SrTiO}_3$  interface which forms the core of this thesis. Additionally they deserve attention because ferroelectrics have been highly exploited in technology over the past few decades. For example they have been utilised in capacitors, sensors, actuators, thermistors and optoelectronics devices and more recently non-volatile memories. Further developments over the past several years are opening up novel device opportunities for ferroelectrics in the future, such as the discovery of giant-tunnelling electroresistance in ultra-thin films for non-destructive, higher density and faster operation ferroelectric memories (5; 6; 7; 8).

A ferroelectric material is an insulator with two or more local ground states of differing non-zero polarisation that can be switched upon application of an external electric field. The term ferroelectric was first applied to the perovskite  $\text{BaTiO}_3$

in 1945 (4), however the first discovery of a material showing polarisation reversal with an external electric field was the Rochelle salt in 1920 (9; 10; 11). These discoveries were a consequence of prior work on classes of materials known as pyroelectrics and piezoelectrics, which display coupling of polarisation with temperature and stress respectively. In fact all ferroelectrics are both pyroelectric and piezoelectric, and all pyroelectrics are piezoelectric (but the converse statements are not true). 21 out of the possible 32 crystallographic point groups have no inversion centre (non-centrosymmetric), of which 20 can exhibit piezoelectricity. Pyroelectrics and ferroelectrics constitute 10 out of these 20 point groups which have a unique polar axis, allowing for a spontaneous polarisation parallel to this axis <sup>1</sup>.

Within the ferroelectric phase, the free energy landscape contains at least two local minima, corresponding to two different orientations of the polarisation vector,  $\mathbf{P}$ . A small electric field may not switch the polarisation from one state to the other, due to the presence of a barrier between the two minima. This energy barrier, and the presence of domains (small volumes of material having uniform polarisation) produces the well known hysteresis curve of polarisation as a function of applied electric field in bulk ferroelectric materials (see figure 1.2). Measurements of polarisation usually involve sandwiching the material between capacitor plates. One method involves applying electric fields across the sample to switch the ferroelectric, where the polarisation is related to the integrated current flowing through the circuit. Note that access to the bulk contribution of the polarisation of each state separately is not possible, only the difference in polarisation between the two states. Chapter 2 expands on this discussion.

A ferroelectric usually only displays switchable polarisation states below a certain temperature,  $T_0$ , above which it is paraelectric. In some cases this phase

---

<sup>1</sup>Even centrosymmetric classes can formally have a non-zero polarisation (see chapter 3). This polarisation is not switchable and hence these materials are not ferroelectric. However the term ‘polar’ in the context of this thesis is used to describe any material with a non-zero polarisation, in relation to the study of polar surfaces (12).

## 1. INTRODUCTION

---

transition temperature, or Curie temperature, is predicted to be higher than the melting point of the material, or lower than absolute zero. In the latter case the material is called an incipient ferroelectric or quantum paraelectric, as in the case of  $\text{SrTiO}_3$ . The ferroelectric-paraelectric phase transition can be classed into two types; order-disorder and displacive. Within both classes, the ferroelectric phase is described by the presence of dipoles within each unit cell which all align between unit cells to form a macroscopic polarisation. Ferroelectricity is therefore a collective phenomena. For perovskites the dipole within each unit cell usually originates from the A or B cation off-centring (see figure 1.2). The origin of this off-centring can be described approximately using the above discussion of the Goldschmidt tolerance factor, or more rigourously within electronic structure theory, see below. The order-disorder and displacive transitions differ in the description of the paraelectric phase. Within the order-disorder picture, the paraelectric phase consists of randomly ordered dipoles (such as in  $\text{BaTiO}_3$ , see e.g. ref. (13)), whereas for the displacive transition the paraelectric phase consists of no-dipoles - the B cation returns to the centre of the unit cell. Several structural phase transitions within the ferroelectric phase can also appear below the Curie temperature, such as in  $\text{BaTiO}_3$ . With decreasing temperature the system changes from tetragonal to orthorhombic and finally to rhombohedral symmetry due to a rotation of the polarisation axis from  $[001]$  to  $[011]$  and finally  $[111]$  direction below 183K.

A major breakthrough in understanding the microscopic origin of ferroelectricity in perovskites came through electronic structure calculations using density functional theory (DFT). A brief introduction to DFT is presented in chapter 2. In the early 1990's Cohen (14) performed DFT calculations on  $\text{BaTiO}_3$  and  $\text{PbTiO}_3$ , reproducing the experimental off-centred ferroelectric phase. A large hybridisation between the nominally empty Ti  $3d$  and O  $2p$  was observed. It was proposed that if the energy gain through the formation of these new covalent bonds with B-cation off-centring is larger than the energy cost associated to

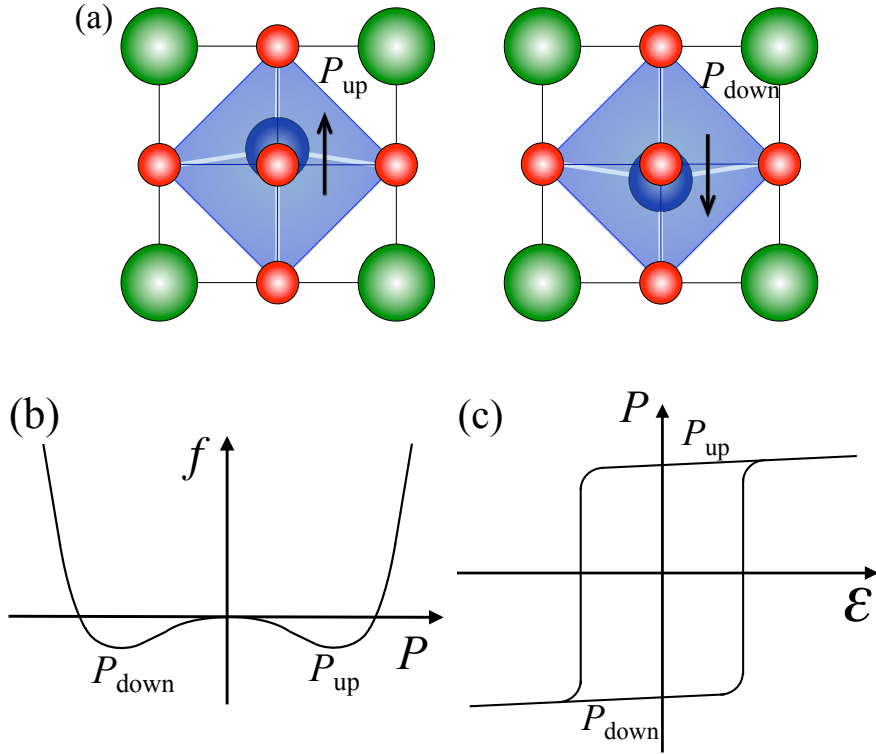


Figure 1.2: (a) Schematic of the off-centring for up and down ferroelectric polarisation states. (b) The typical double well shape of the free energy as a function of polarisation. (c) The hysteretic behaviour of the polarisation with applied electric field,  $\mathcal{E}$ .

short-range ionic Coulombic forces, the system would spontaneously polarise. The  $dp$  hybridisation is intimately linked with the anomalously large Born effective charges,  $Z^*$ , in ferroelectrics. The Born effective charge is dynamical, and should be distinguished from static charges which are usually based on partitioning the full electron density into contributions from different ions. Instead  $Z^*$  relates the change in polarisation upon displacement of an atomic sub-lattice.  $Z^*$  is large in ferroelectrics due to the charge transfers associated with bond formation upon B cation displacements.

Macroscopically, ferroelectric phase transitions can be described phenomenologically within thermodynamic theory. This is the Landau-Ginzburg-Devonshire

## 1. INTRODUCTION

---

(LGD) theory (15; 16). In a simplified form (1D treatment of 3D system with no anisotropy) in the absence of strain and an external electric field, the free energy of a ferroelectric can be expressed as a function of polarisation,  $P$ , and temperature,  $T$ ,

$$f(T, P) = a_1 P^2 + a_{11} P^4 + a_{111} P^6, \quad (1.2)$$

where the coefficients are temperature dependent. Perhaps the most important coefficient,  $a_1$ , takes the form,  $a_1 = \alpha(T - T_0)$ , where  $\alpha$  is a positive constant and  $T_0$  is the phase transition temperature. Additionally the coefficient,  $a_{11}$ , determines the type of transition; first or second order. For a second order transition,  $a_{11}$  is positive. When  $T > T_0$ ,  $a_1$  is positive, and the free energy is a single well with minimum at  $P = 0$ , and the material therefore in the paraelectric state. If instead  $T < T_0$ , the free energy is a double well (see figure 1.2) with minimum at  $P = \pm P_S$ , where  $P_S = \sqrt{-a_1/(2a_{11})}$  is the spontaneous polarisation of the material in the ferroelectric phase. The polarisation evolves gradually with temperature until reaching zero at the transition temperature, hence the transition is second order. For a first order transition,  $a_{11}$  is negative, and the free energy can have three local minima within a certain temperature range. Across the transition the global minimum switches from a location at  $P_S$  to zero, producing a discontinuous change in the polarisation, and hence the transition is first order. BaTiO<sub>3</sub> goes through several first order phase transitions.

In connection with the next section, we briefly highlight one of the many ways that an interface can dramatically affect a ferroelectric system. Take the simplest example of an interface with vacuum, i.e. a surface, of a ferroelectric material. A polarisation in the ferroelectric produces a net surface charge density,  $\sigma = \mathbf{P} \cdot \hat{\mathbf{n}}$ . In other words the surface charge density equals the magnitude of the polarisation normal to the surface. For a free standing film, open circuit boundary conditions can be assumed, i.e. the electric field in vacuum is zero. In the absence of any external charges, it can be easily shown using Gauss's law that a constant electric field within the film appears, with magnitude  $\sigma/\epsilon_0$ , pointing in opposite

direction to the polarisation (where  $\epsilon_0$  is the permittivity of free space). The energy associated with this internal electric field (called the depolarising field) is positive and large, adding to the quadratic term of the LGD free energy. The free energy becomes a single well for practically all accessible temperatures, rendering the material in the paraelectric phase. In reality the surface may have access to some form of screening charge which is able to reduce the net surface charge of the material and lower the depolarising field (chapter 8 considers a surface redox process forming charged defects). Alternatively the depolarising field can also be reduced by forming a periodic arrangement of  $180^\circ$  domains, if the domain wall energy cost is less than the ferroelectric well depth.

### 1.1.3 Interfaces

A heterostructure, is a layered system consisting of two or more different materials, and the boundary between layers is called the interface. Interfaces are key in many scientific areas and technological applications. For example semiconductor devices such as solar cells, lasers and transistors all rely on interface physics. This thesis considers two types of interface, both of two-dimensional form; surfaces (between an oxide and air or vacuum), and epitaxial interfaces (between two oxides). An epitaxial interface implies some degree of crystallographic matching between the atomic structure of the substrate and the film. The film and substrate need not be of the same crystal class for this to occur. The crystallographic registry between substrate and film of differing compositions is called heteroepitaxy.

Current techniques for epitaxial growth offer the possibility for control at an atomic level. Before film growth, the quality and termination of the underlying crystalline substrate surface is considered. Within the semiconductor industry, chemical etching processes to produce smooth, defect free surfaces are well known. The equivalent processes for oxides are still in their infancy, but some recipes for the most common oxide substrate,  $\text{SrTiO}_3$ , are reported (17; 18). It should be

## 1. INTRODUCTION

---

noted that in reality almost all substrate surfaces are vicinal containing atomic-scale steps, usually due to a small miscut angle from the ideal surface plane (see for example ref. (19) for more details). Once the substrate surface has been controlled, growth of the film proceeds with a choice of various deposition methods. The most common method used to grow the oxides presented in this thesis is pulsed laser deposition (PLD), followed by molecular beam epitaxy (MBE). In PLD a high-power laser is used to ablate a solid target which deposits on a heated substrate. Several growth parameters such as temperature, laser fluence and oxygen partial pressure are key to producing layer-by-layer stoichiometric oxide films. A comprehensive review of PLD can be found in ref. (20). Using reflection high-energy electron diffraction (RHEED) the growth of these oxide heterostructures can be monitored and controlled with layer-by-layer precision.

In the early stages of heteroepitaxial growth, or in low lattice mismatch systems, coherent epitaxy can occur whereby identical copying of the atomic registry between surface and film produces pseudomorphic growth. The bi-axial lattice mismatch strain induced by the substrate into the film is defined as,  $(a_{\text{sub}} - a_{\text{film}})/a_{\text{film}}$ , where  $a_{\text{film}}$  and  $a_{\text{sub}}$  denote the lattice parameter of the film and substrate respectively (for simplicity we assume cubic bulk structure for both film and substrate). A positive strain represents tension, and negative strain compression. A third strain normal to the interface is also induced due to the Poisson effect. In later stages of growth, or in highly mismatched systems, periodic dislocations (called misfit dislocations) are introduced at the interface to reduce the lattice mismatch strain. At this point the system is called semi-coherent. There usually exists a critical film thickness at which the transition between coherent and semi-coherent growth occurs. All the systems studied in this thesis are within the coherent regime since the films are ultrathin (several nm or less thick).

The effect of bi-axial mismatch strain in ultrathin films can sometimes be a dominating effect in determining their properties. The strain changes the distance between atoms and the orbital overlap, therefore affecting both lattice and

electronic degrees of freedom. The field of strain engineering in complex oxides is becoming popular, the idea being that careful selection of the substrate lattice parameter can tune the properties of the film to those desired. One striking example includes the prediction (21), and experimental confirmation (22), that  $\text{EuTiO}_3$ , in bulk form paraelectric and antiferromagnetic, can become simultaneously both ferromagnetic and ferroelectric under epitaxial strain (albeit the experiments used tensile strain, whereas the theory studied compressive). There are many other examples of strain engineering in complex oxide thin films, some of which are described in refs. (23; 24; 25).

Apart from strain there are many other effects by which interfaces can induce alterations to the charge, spin, orbital and lattice degrees of freedom. These include, charge transfer, symmetry breaking, frustration and electrostatic coupling. A description of each is beyond the scope of this chapter, but for a recent review, see ref. (26). We concentrate on electrostatic coupling below.

Electrostatic coupling becomes important when a material has a non-zero polarisation component normal to the interface (or surface). The electrostatic stability of crystalline surfaces is central to many of the concepts presented in this thesis, and has been the subject of confusion and debate since it was first formally discussed by Tasker in 1979 (12). In this section we only introduce some of the topics, leaving a more detailed treatment for chapters 2 and 3.

Tasker considered the surfaces of ionic crystals, whereby the surface is created by stacking bulk unit cells without allowing for any further ionic or electronic relaxation (see figure 1.3). This has been called the bulk frozen surface (27). The semi-infinite system is modelled by a set of point charges taking the formal valence of each ion. Tasker proposed that a surface is classified as polar if the bulk unit cell contains a finite dipole moment. The polarisation, and hence surface net charge ( $\mathbf{P} \cdot \hat{\mathbf{n}}$ ), within the textbook Clausius-Mossotti picture (see chapter 2), is equal to the dipole moment per unit volume of these formal point charges. A non-zero surface net charge density is energetically unstable since a plane of

## 1. INTRODUCTION

---

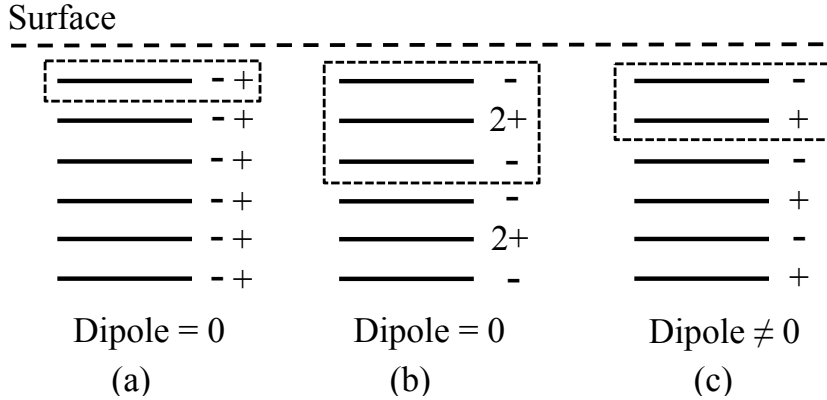


Figure 1.3: Tasker's ionic surface classification. (a) Type 1 with zero planar charges due to equal anions and cations on each plane. (b) Type 2 has charged planes but zero net dipole moment perpendicular to the surface. (c) Type 3 has both charged planes and a net dipole moment perpendicular to the surface. (Figure adapted from ref. (12)).

charge separating two semi-infinite systems produces a divergent electrostatic energy. This has been termed the 'polar catastrophe'. Therefore polar surfaces are predicted to not exist in nature, but require some form of charge screening.

Recently the use of the ideal formal charges, was replaced by a more realistic charge distribution in crystals taking in to account covalency (27). The classification of polar surfaces was instead based on the use of dipole-free unit cells. Once a dipole free unit cell is constructed, the existence of remaining charge left over in the surface unit cell defines a polar surface.

There are several apparent problems with both approaches described above (12; 27). The most important is that no connection to the modern theory of polarisation is made in either of these cases (see chapter 2). The charge density alone is not enough to define the polarisation, but also the phase of the wavefunctions is required. This inaccuracy led to the false concept of 'weak polarity' at the  $\text{SrTiO}_3$  (001) surface (27). It is only very recently that the modern theory of polarisation has been formally applied to the concept of polar surfaces (and in-

## 1.1 Oxides, interfaces and polarity

---

terfaces) (28; 29). It turns out that, by chance, Tasker's picture of formal charges is sufficient to define the polarisation for all materials that are characterised by a centre of symmetry. For materials lacking this symmetry, a non-trivial electronic component to the polarisation must be added. This component is related to the anomalous Born effective charge in ferroelectrics. If the bulk polarisation is non-zero, the surface is polar.

The interface theorem (30), can be used to classify a polar interface. If the difference in the component of the bulk polarisations normal to the interface from material A to material B is non-zero, the interface is polar. It is equivalent of adding the surface charge contributions from both materials either side of the interface. It should be noted that, of course, in reality no system is semi-infinite. In the case of thin films, both an interface with the substrate and a surface exists, usually with equal and opposite interface charge densities. Under open circuit boundary conditions and for finite sized films, the electrostatic energy no longer diverges. This is because the two interfaces are coupled, essentially creating a dipole across the film, and zero field elsewhere.

A polar surface or interface can neutralise the excess net charge density via several types of mechanisms. Extrinsic mechanisms (requiring an external reservoir/sink) include adsorption of foreign species and changes in the interface stoichiometry. Intrinsic mechanisms include electronic reconstruction and dielectric screening. For example the nominally polar Ge-GaAs (001) interface is thought to undergo an atomic reconstruction producing a non-stoichiometric interface (31). More recently there has been evidence suggesting that ferroelectric surfaces are affected by adsorption and desorption processes during polarisation reversal (32; 33; 34). One of the most popular examples of recent times is the interface metallicity in the  $\text{LaAlO}_3\text{-SrTiO}_3$  (001) system (35). It is thought that the interface two-dimensional electron gas appears due to the fact that the interface is polar (36), but the precise origin (intrinsic vs. extrinsic), and even the role of polarity is still debated. The next section summarises the key experimental

## 1. INTRODUCTION

---

and theoretical studies of the  $\text{LaAlO}_3\text{-SrTiO}_3$  system.

### 1.2 The $\text{LaAlO}_3/\text{SrTiO}_3$ interface

At room temperature  $\text{SrTiO}_3$  (STO) is a perovskite in the ideal undistorted cubic structure, with a lattice parameter of  $3.905 \text{ \AA}$  (37) and  $\text{LaAlO}_3$  (LAO) is a distorted rhombohedral perovskite with small rotations of the  $\text{AlO}_6$  octahedra. LAO can be considered as pseudocubic with a lattice constant of  $3.791 \text{ \AA}$  (38). Both are band insulators with band gaps of  $3.2 \text{ eV}$  (39; 40; 41) and  $5.6 \text{ eV}$  (42) respectively. The combination of a relatively small lattice mismatch between LAO and STO (3%) and similar thermal expansion coefficients (43; 44) suggests the potential for coherent epitaxial growth between the two.

The discovery that the LAO-STO interface is metallic in 2004 (35), was therefore a surprising result. Since the original finding, the LAO-STO interface has become a whole field of research in itself with a worldwide effort into understanding and utilising the interface's metallicity. Ohtomo and Hwang's seminal paper (35) has received over 700 citations to date. Since it is a fairly new topic, the field has developed considerably since the first discovery. The next several sections attempt to provide a brief overview of the most significant developments. We first provide a summary of experimental and theoretical results on a selection of important topics (interface transport and role of oxygen,  $\text{LaAlO}_3$  thickness dependence, field effects and electronic properties) and at the end discuss possible mechanisms to explain the results. Comprehensive reviews and shorter surveys can be found in refs. (45; 46; 47; 48; 49; 50; 51).

#### 1.2.1 Interface transport and the polar catastrophe

In Ohtomo and Hwang's seminal paper (35), LAO films were grown using pulsed laser deposition (PLD) on STO (001) substrates. Two different (001) STO terminations were used as a precursor to LAO growth;  $\text{TiO}_2$  and  $\text{SrO}$ . This

## 1.2 The $\text{LaAlO}_3/\text{SrTiO}_3$ interface

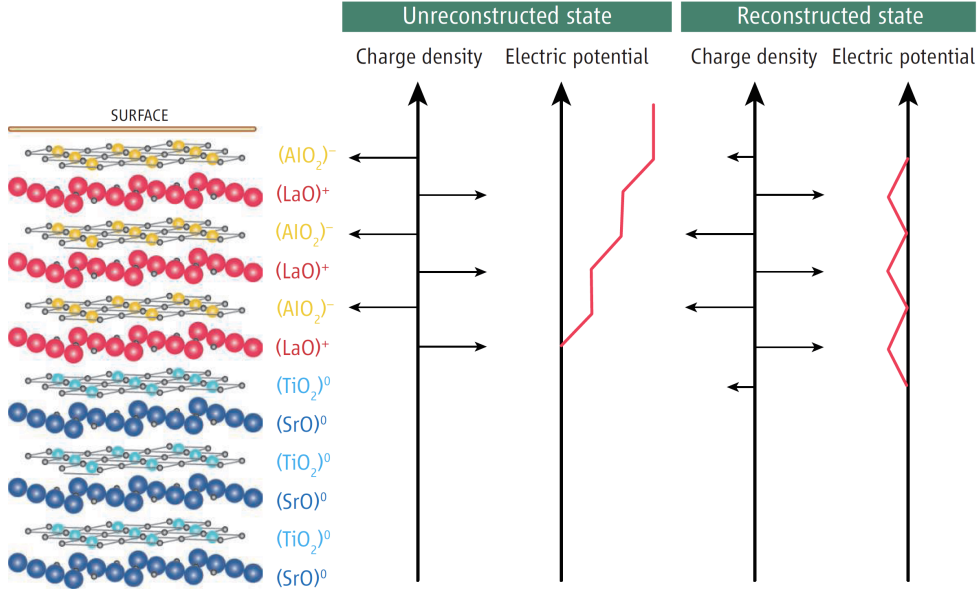


Figure 1.4: (Left): The (001) LAO-STO system, showing the planar formal charge density. (Middle): The resulting electric potential which diverges with thickness. (Right): If 0.5 electrons per two dimensional unit cell are removed from the LAO surface and placed at the interface, the resulting potential no longer diverges. (Figure adapted from reference (45)).

formed two different interfaces;  $\text{TiO}_2\text{-LaO}$  and  $\text{SrO-AlO}_2$  which we call  $n$  and  $p$  type interfaces (for reasons that will become clear below). See figure 1.4 for a schematic of the  $n$ -type interface. Hall transport measurements showed that whilst the  $p$ -type LAO-STO interface showed insulating behaviour, the  $n$ -type interface is conducting with a high electron mobility ( $10^4 \text{ cm}^2 \text{ V}^{-1}\text{s}^{-1}$  at low temperatures). This remarkable result shows how a change of a single atomic layer at an interface can dramatically alter the electronic properties of the system. Using atomic resolution electron energy loss spectroscopy (EELS) Nakagawa and Hwang (36) inferred soon afterwards the presence of approximately 0.3 oxygen vacancies per two dimensional unit cell at the  $p$  type interface and 0.7 electrons per two dimensional unit cell at the  $n$  type interface.

In order to rationalise their results, Nakagawa and Hwang (36) presented an

## 1. INTRODUCTION

---

argument called the polar catastrophe, which is illustrated in figure 1.4. Starting from the frozen bulk interface, the formal charges on each atomic (001) plane parallel to the interface are 0 and  $\pm 1$  electrons per two dimensional unit cell in STO ( $\text{SrO}^0$  and  $\text{TiO}_2^0$ ) and LAO ( $\text{LaO}^+$  and  $\text{AlO}_2^-$ ) respectively. One can solve the electric potential of this charge distribution using Gauss's law, given an electrical boundary condition. It is simple to show that under open circuit boundary conditions (i.e. the electric field is zero in the thick STO substrate and vacuum) the electric potential diverges with LAO thickness, since a constant non-zero electric field appears within LAO. One way to prevent this energetically unstable 'polar catastrophe' is by adding 0.5 holes (or 0.25 oxygen vacancies) per two-dimensional unit cell at the  $p$ -type interface and 0.5 electrons per two-dimensional unit cell at the  $n$ -type interface. The measured deviation from these numbers was argued to arise to reduce the interface band offset (see ref. (36) for more details). The polar catastrophe mechanism became a popular explanation for the origin of conductivity in LAO-STO. Many experimental studies that came after were inspired by attempting to prove or disprove the mechanism, and so we will refer back to it frequently. After these first two studies (35; 36) most experimental investigations concentrated on the metallic  $n$  type interface.

### 1.2.2 The role of oxygen partial pressure

Very early on the effect of growth conditions, in particular the oxygen partial pressure,  $p_{\text{O}_2}$  and oxygen annealing process, were known to alter the transport properties at the interface. Even in Ohtomo and Hwang's original paper, these parameters were tested and were seen to affect the Hall mobility, sheet resistance and carrier density of the  $n$ -type interface. This stimulated several further attempts to understand the effect of  $p_{\text{O}_2}$  and oxygen annealing processes on the  $n$ -type interface (52; 53; 54; 55; 56). For a summary of results see Table 1 of ref. (50). Whilst a scatter of values is found for the Hall mobility and sheet resistance, there seems to be a general agreement between studies that for samples

grown at high  $p_{\text{O}_2}$  (approximately  $10^{-4}$  mbar), the sheet carrier density is between  $10^{13}$ - $10^{14}$   $\text{cm}^{-2}$ . This is approximately 0.02-0.2 electrons per two dimensional interface unit cell, three orders of magnitude less than the density found at low  $p_{\text{O}_2}$  (approximately  $10^{-6}$  mbar), and over an order of magnitude less than that expected from the polar catastrophe (36). We highlight ref. (56) as an important study that helped to understand these results. Basletic *et al.* (56) discovered using a conductive tip atomic force microscope in cross-section that the spatial extent of the interface carriers changed from hundreds of micrometres into STO to within a few nanometres at the interface upon a high  $p_{\text{O}_2}$  anneal (see below for more on spatial extent of carriers). It suggests two types of carriers, one extending deep into the STO substrate and the other forming a two-dimensional electron gas (2DEG) at the interface. It was argued that at low  $p_{\text{O}_2}$  and without annealing, oxygen vacancies, a common defect in oxides, are formed during the growth process in STO. Each oxygen vacancy acts as an  $n$ -type donor, giving up two electrons available for conduction. This meant that in order to study the possibly intrinsic carriers that locate within nanometres of the interface, a well controlled growth process is needed to prevent the formation of STO oxygen vacancies. A recipe for such a growth procedure is given in ref. (57) and a review including substrate treatment can be found in ref. (47). The literature that is discussed in the remaining sections utilises this growth process, unless explicitly mentioned otherwise.

### 1.2.3 $\text{LaAlO}_3$ thickness dependence

A significant development was made when it was discovered that the conductivity at the  $n$  type interface only occurs for LAO films greater than 3 unit cells thick (58). Not only can the insulating-metallic transition at this critical thickness be used in field effect devices (see next section), but it would provide important clues as to the origin of the conductivity. The insulating-metallic critical thickness has since been reproduced among several groups using pulsed laser

## 1. INTRODUCTION

---

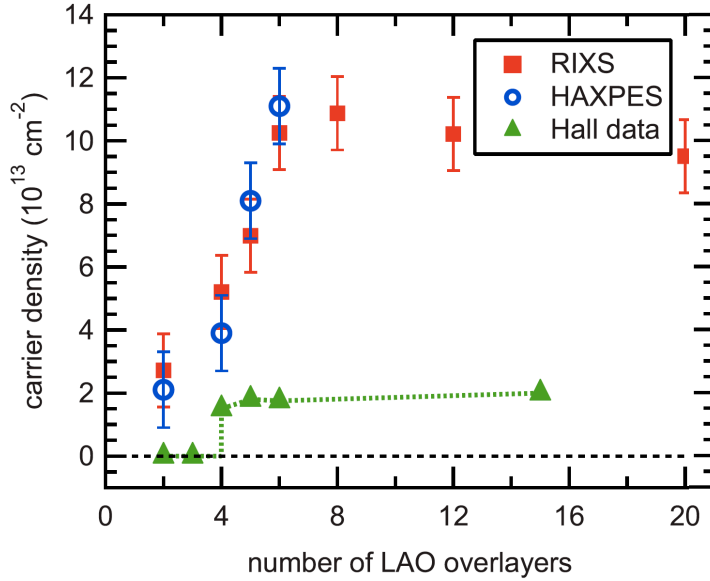


Figure 1.5: Comparison of the interface electron density measured via Hall transport (58), hard x-ray photoelectron spectroscopy (HAXPES) (59) and resonant inelastic x-ray scattering (RIXS) (60). (Figure adapted from reference (60)).

deposition techniques, and interestingly also molecular beam epitaxy (61), hinting towards a general mechanism not specific to the growth technique (once STO oxygen vacancies are removed). The sheet carrier density is below detectable levels for LAO films less than 4 unit cells thick, and increases in a step-like jump to a value between  $1 \times 10^{13}$  -  $3 \times 10^{13}$   $\text{cm}^{-2}$  (approximately 0.02-0.05 electrons per two dimensional interface unit cell - an order of magnitude less than that expected from the polar catastrophe (36)) with no further noticeable change at larger thicknesses (see figure 1.5). The effect of thickness on the sheet carrier density has been found to be quite different when a further STO capping layer is deposited on the LAO film. A small but finite density is found for LAO films as thin as one unit cell, and increases gradually to a value of approximately 0.2 electrons per two-dimensional unit cell at about 6 LAO unit cells (62). The non-existence of a critical thickness in this experiment may simply be due to the lower  $p_{\text{O}_2}$  ( $10^{-5}$  mbar) and lack of annealing. However more recent experiments and calculations

## 1.2 The $\text{LaAlO}_3/\text{SrTiO}_3$ interface

---

have suggested that the STO capping layer is responsible for this difference (63). For the moment we will concentrate on the bare uncapped LAO-STO system.

Spectroscopy measurements (photoemission and x-ray scattering) have also been utilised to determine the interface conduction band density (59; 60; 64) as a function of LAO thickness. Note here that it is the STO conduction band (Ti  $3d$ ) density being determined, which may or may not be mobile, unlike the carrier density as measured in transport. In all cases a larger sheet density than that seen in transport experiments was observed and even at an LAO thickness of 1 or 2 unit cells (59; 60; 64). The sheet density is seen to increase with LAO thickness to a value of approximately 0.2 electrons per two dimensional interface unit cell at 6-8 unit cells (59; 60), after which the density seems to remain constant (60) (see figure 1.5). There are several interesting points to note here. Firstly it is apparent that not all the Ti  $3d$  states contribute to transport, indicating two types of carriers: mobile and trapped. Indeed further spectroscopic evidence found in insulating systems in-gap Ti  $3d$  like states, but in conducting interfaces additional Ti  $3d$  states at the Fermi level (65). Secondly, whilst the density measured by spectroscopy is closer to that expected from the polar catastrophe than the density measured by transport, there are still more than half the electrons unaccounted for. It is interesting to note the increase in density with thickness up to 6-8 unit cells at which point the density remains independent of thickness (or possibly slowly decreases). This transition at 6-8 unit cells is close to the critical thickness for strain relaxation due to epitaxial mismatch (66) at which point misfit dislocations appear at the interface. Whilst an effect of dislocations on electron transport by scattering has been found (67), it is unknown what influence they could have on the character of the interface electron states in connection with spectroscopy.

The structural properties of LAO-STO have also been experimentally examined as a function of LAO thickness. Here we highlight two studies, which as we will discuss further below, support the concept of the importance of polarity

## 1. INTRODUCTION

---

in LAO-STO. An off-centring of the cation positions with respect to the ideal perovskite LAO structure, similar to the off-centring described above in ferroelectrics, was inferred from surface x-ray diffraction measurements (68). The magnitude of this off-centring was seen to reduce with increasing LAO thickness. In a second study, x-ray diffraction was used to determine the LAO out-of-plane lattice parameter,  $c$ , as a function of LAO thickness (69). They find that  $c$  starts at a larger value than that expected from elastic arguments alone, and reduces with increasing LAO thickness until at 6 unit cells when it reaches the elastic limit. Since off-centring is known to affect the lattice parameter, both studies are likely connected and in agreement. In fact both are signatures of an internal electric field within thin LAO films, consistent with that expected from the polar catastrophe (36).

Some aspects of the transport, spectroscopic and structural experimental investigations have been qualitatively reproduced (or predicted) with density functional theory (DFT) calculations (see chapter 2). An insulating to conducting transition with LAO thickness in the  $n$ -type interface has been found within DFT calculations, after the experimental observation. The first several studies calculating this critical thickness can be found in refs. (70; 71; 72; 73). A range of critical thicknesses have been reported; anywhere between 4-6 unit cells. The variation was later discussed as due to a dependence of the critical thickness on the STO band gap, which DFT underestimates to various degrees depending on the exchange correlation functional, and also the LAO dielectric constant, which is sensitive to strain (50). Additionally the LAO off-centring experimentally observed (68) as discussed above, had been previously predicted by DFT calculations (71; 73). The DFT calculations made significant developments towards understanding the mechanism of conductivity, in pristine (defect free) LAO-STO systems for which the calculations were performed on. They showed the existence of an electric field within LAO, in agreement with the polar catastrophe. At the critical thickness the potential drop across the film reaches the band gap of STO,

and electrons are transferred from the LAO surface to the STO interface. A computed layer-by-layer density of states which graphically captures this process can be found in ref. (72). The quantitative agreement (or disagreement) of this mechanism with experiment will be explored further below.

### 1.2.4 Field effects

Another significant discovery was that a gate voltage across the LAO-STO system can drive the interface reversibly between insulating and metallic regimes (58) when a LAO thickness of just below the critical is used. The findings were not only important for helping to understand the origin of the metallicity, but also presented a novel design for potential device applications within oxide electronics.

The field effect was later reproduced in ref. (70) (with a corresponding news article (74)) this time using a biased atomic force microscopy (AFM) tip to reversibly write and erase nanoscale conducting regions, with potential applications for high-density information storage devices. In both ref. (58) and (70) a LAO thickness of exactly 3 unit cells was required for the switching process, in connection with the critical thickness (58). In the latter, it was proposed that oxygen vacancies at the surface of LAO (not in STO as previously discussed) could be playing a role (70). Within this study a DFT calculation showed that the formation of an oxygen vacancy at the LAO surface, could alter the system from insulating to metallic, if the system was originally in the insulating state. In connection, evidence came later suggesting charge writing at the LAO surface was behind the AFM conductivity switching experiments (75), and that the process was dependent on the existence of water in the surface environment (76).

The field effect was additionally found to be able to switch the insulating state into a superconducting state (77) at low temperatures. These correlation effects and other interface electronic properties will be briefly summarised in the next section.

## 1. INTRODUCTION

---

### 1.2.5 Electronic properties

In this section, the properties (for example spatial extent, orbital character, correlation effects) of the conducting electron gas are presented. Since this thesis has been more concerned with the origin of the conducting region, rather than its properties, this section will only provide a brief summary of results. However some of the electronic properties can provide clues of its origin, and so we concentrate on these cases.

One of the first questions posed after Ohtomo and Hwang's initial transport measurements (35), was to what spatial extent are the electron carriers confined in STO? As mentioned already above, the growth conditions were found to dramatically influence the answer to this question. In samples grown at low  $p_{O_2}$  and without annealing, the carriers were found to extend deep into STO producing a 3D metallic region (54; 56; 78). Cross-section conductive tip atomic force microscopy measurements revealed that the spatial extent of the interface carriers changed from hundreds of micrometres into STO to within a few nanometres at the interface upon a high  $p_{O_2}$  anneal (56). It was suggested that two types of interface carriers exist, one extending deep into the STO substrate due to oxygen vacancies in STO, and the other forming a two-dimensional electron gas (2DEG) possibly intrinsic to the interface. This quasi-2D nature of the electron carriers under appropriate growth conditions has since been reproduced by several groups. For example hard x-ray photoelectron spectroscopy studies found the thickness of the carriers to be less than 4nm (59). Another cross-section conductive tip atomic force microscopy study measured the thickness to be less than 10 nm (79). Using atomic layer doping and transport measurements another study inferred the majority of the electron gas to lie within just 1 unit cell from the interface (80). Finally infrared ellipsometry found an asymmetric concentration profile, with a rapid initial decay from the interface over the first 2 nm and a pronounced tail that extends to about 11 nm (81). An effort also came from the DFT community to understand the spatial extent of the carriers. Early calculations also found the

electrons to be confined close to the interface (approximately 1 nm) (82; 83; 84). Later calculations using larger simulation sizes to include more STO units, found that whilst the majority of carriers lie within a nm of the interface, some extend further out with a slowly decaying density (85; 86; 87) in agreement with the infrared ellipsometry measurements (81). This suggests that electron carriers occupy at least two different bands, and connects with the next topic, the orbital character of the electron gas.

The first study to investigate the orbital character of the electronic carriers used atomic resolution electron energy loss spectroscopy (EELS), inferring the existence of  $\text{Ti}^{3+}$  states (36) localised near the interface. In bulk STO, Ti nominally has a charge state of  $\text{Ti}^{4+}$  with the unoccupied conduction band edge being of Ti  $3d$  character. Hence the existence of  $\text{Ti}^{3+}$  at the interface, indicates the likelihood of an electronic reconstruction filling the Ti  $3d$  band. This has since been reproduced with additional EELS measurements, however deviations in the interface Ti valence were found to be not as pronounced as the initial experiments (88). Further investigations using x-ray absorption spectroscopy revealed that the usual degeneracy of the Ti  $3d t_{2g}$  orbital is lost at the LAO-STO interface, with the  $3d_{xy}$  state being occupied first (89). More complex behaviour has been suggested by various experiments, such as suspected polaronic behaviour (81), and the interface electrons occupying at least two different states with localised and delocalised character (65; 90; 91). DFT calculations are a natural theoretical tool for understanding the electronic ground state behaviour of the interface. Many DFT investigations of the  $n$ -type LAO-STO interface have found occupied Ti  $3d$  states at the interface, and the first few can be found in refs. (71; 82; 92; 93). The splitting of the Ti  $3d t_{2g}$  orbital degeneracy has also been observed, with the  $3d_{xy}$  state being occupied first (82; 94), in agreement with x-ray absorption spectroscopy (89). With increasing carrier density the  $3d_{xz}$  and  $3d_{yz}$  states also become occupied. Ref. (94) showed that the lowest  $d_{xy}$  band is localised in the out-of-plane direction having a strongly 2D character, whilst the  $d_{xz}$  and  $d_{yz}$  states

## 1. INTRODUCTION

---

extend further into STO with a more 3D character. It was suggested that the 2D  $d_{xy}$  bands are subject to Anderson localisation, and hence their contribution to transport measurements may be strongly suppressed (94) providing a possible explanation for the lower electron density measured in transport (58) compared with spectroscopy (59; 60; 64) and that expected from the polar catastrophe (36).

We end this section with a brief mention of correlation effects, which whilst an extremely popular area receiving much attention, is beyond the scope of this thesis. Experimental evidence of magnetic properties of the 2DEG (95) by magnetoresistance measurements appeared approximately one year after the first prediction with DFT calculations (82). Further DFT calculations explored the effect of localisation and  $\text{TiO}_6$  octahedra tilting on the ground state magnetic ordering (96; 97). In addition, superconductivity has been observed (98), which has since been controlled with a field effect (77). Coexisting (99; 100), or phase separated (101), ferromagnetic and superconducting LAO-STO has recently been discovered. These fields are new and growing areas with still many open questions and opportunities (see refs. (47; 50) for further discussions).

### 1.2.6 Possible origins

In a recent short review article (51) a summary of the potential origins to the 2DEG was given. A table was presented which listed several important experimental observations with a potential mechanism explaining its origin (oxygen vacancies, interdiffusion, or electronic reconstruction due to the polar catastrophe). Every experimental observation listed was said to be explained via electronic reconstruction due to the polar catastrophe, whereas the other mechanisms (oxygen vacancies and interdiffusion) could not. The authors therefore ascribed the experimental phenomena in LAO-STO purely to the polar catastrophe, essentially suggesting a closed case. We will now explore the potential mechanisms, in relation to the experimental and theoretical studies that are reviewed above, to show that whilst the polar catastrophe agrees with several of the observed phenomena,

it does not naturally explain them all.

So far we have briefly mentioned three mechanisms that have been proposed as the origin to the LAO-STO 2DEG; the polar catastrophe, the formation of  $n$ -type oxygen vacancies in STO, and the formation of oxygen vacancies at the LAO surface. A fourth mechanism that has been proposed is cation interdiffusion (also called intermixing) (102; 103; 104; 105; 106). Such intermixing has been measured on a range of LAO-STO samples using various experimental techniques. The common argument is that when La and Sr interdiffuse between the two materials, the  $\text{La}^{3+}$  replacing  $\text{Sr}^{2+}$  acts as an  $n$ -type donor in STO creating the metallic behaviour. However within this local intermixing picture, the  $\text{Sr}^{2+}$  replaces the  $\text{La}^{3+}$  at the other side, acting as a  $p$ -type donor. Hence the electrons of the donors will annihilate with the holes of the acceptors, leaving the system insulating. Local intermixing is not expected to dope the interface, and nor is it expected to provide the charge necessary to prevent the polar catastrophe as shown in chapter 3.

Out of the other three proposed mechanisms (the polar catastrophe, the formation of  $n$ -type oxygen vacancies in STO, and the formation of oxygen vacancies at the LAO surface), the formation of  $n$ -type oxygen vacancies in STO is also not expected to provide the charge necessary to prevent the polar catastrophe. It is also difficult to explain, i) the observation of a LAO critical thickness for metallicity, and, ii) the SrO- $\text{AlO}_2$  insulating interface, in terms of oxygen vacancies within STO. The cross-section conductive tip atomic force microscopy measurements before and after a high  $p_{\text{O}_2}$  anneal (56) is strong evidence suggesting that two types of interface carriers exist, one extended deep into the STO substrate due to oxygen vacancies in STO, and the other forming a two-dimensional electron gas (2DEG) of different origin. However the recent findings that growth under even higher  $p_{\text{O}_2}$  ( $5 \times 10^{-2}$  mbar) can form insulating interfaces at all LAO thicknesses (107) raises doubts as to the role of O vacancies. These experiments deserve future attention and require attempts from other groups to reproduce

## 1. INTRODUCTION

---

their high  $p_{\text{O}_2}$  insulating samples, possibly using different deposition techniques.

Let us now consider the evidence for and against the polar catastrophe. We start with a reminder of the concept presented in ref. (36). Taking the frozen bulk LAO-STO interface, the formal charge density of each AO and  $\text{BO}_2$  (001) plane parallel to the interface are 0 and  $\pm 1$  electrons per two dimensional unit cell in STO and LAO respectively. Solving for the electric potential of the charge density distribution using Gauss's law, it is simple to show that under the boundary conditions of a zero electric field in the thick STO substrate, the electric potential diverges with LAO thickness. Ref. (36) argues that precisely 0.5 electrons per two dimensional unit cell at the  $n$ -type interface would prevent this potential divergence<sup>1</sup>. These arguments would also extend to any II-IV/III-III perovskite interface. Hence the fact that the interfaces between STO and  $\text{LaTiO}_3$  (108),  $\text{LaGaO}_3$  (109), and  $\text{LaVO}_3$  (110) are also metallic, is therefore quite strong evidence towards the polar catastrophe.

The polar catastrophe can also help explain the LAO critical thickness for metallicity, at least qualitatively. For ultrathin and pristine LAO films, the system can remain insulating and sustain an electric field. This has been seen in DFT calculations (70; 71; 72; 73), and can be described by a simple model that includes the band gaps and alignment of LAO-STO and the dielectric screening of LAO (see chapter 4 for an example model for LAO-STO superlattices). Solving for Gauss's law for the  $n$ -type interface as before, one can calculate the macroscopic electric field within LAO, including its dielectric response (see for example ref. (50) for details). Since both materials are insulators, the electric field remains, until at a critical thickness, the potential drop across the film reaches the band gap (in this case STO's band gap since it is the smaller and we assume no valence band offset). At this point electrons are transferred from the valence

---

<sup>1</sup>Note that these numbers are based on formal ionic charge values, and it is well known that perovskites have substantial covalent character. One might therefore expect the electron density to be scaled down accordingly. This however would be wrong. See chapter 3 for a discussion.

band maximum at the surface (of O  $2p$  character) to the conduction band minimum at the interface (of Ti  $3d$  character). Several points between this model and experimental findings agree and several disagree. Firstly the existence of an electric field in LAO has been inferred through structural (68; 69), and tunnelling measurements (111), however it was not seen in x-ray photoemission spectroscopy measurements (61). Whilst Ti  $3d$  states have been measured at the interface, no hole states have been seen at the surface except with a STO capping layer (63) although this could be due to the immobile nature of these states (85). Additionally if one calculates the critical thickness within the model, using the experimental band gaps, and the (strain and electric field dependent) LAO dielectric constant, it equals 6 unit cells (50), not 4 from transport experiments (58) or as thin as 1 or 2 unit cells from spectroscopy (59; 60; 64).

Therefore it seems that whilst there are several pieces of experimental evidence supporting the polar catastrophe, there are also a few discrepancies, and the picture is not as clear as it is made out to be in ref. (51). A final possibility, which has yet to be explored fully, is interface doping through the formation of surface oxygen vacancies (70). In chapter 7 we model the energetics of this processes, show that several experimental results incompatible with the polar catastrophe find natural explanations and hence propose it as an alternative origin to the 2DEG.

## 1.3 Aims and Objectives

The principal aim of this thesis is to further the understanding of interfaces between polar materials and related screening effects through analytical modelling and first principles calculations. The interface between  $\text{LaAlO}_3$  and  $\text{SrTiO}_3$  provides an excellent system to do this since it shows novel behaviour requiring new scientific understanding, and due to its high popularity providing opportunities for discussions and collaboration with experimental groups. The initial moti-

## 1. INTRODUCTION

---

vation for this thesis was to provide helpful guidelines, using basic theoretical principles, towards understanding the origin of the two-dimensional electron gas (2DEG) at the  $\text{LaAlO}_3\text{-SrTiO}_3$  interface. Through studying the pristine system (chapters 3 and 4) and realising the importance of electrostatics and polarity in these materials, we were led to ask several related questions: (i) can the polarisation of LAO be utilised further to create new electronic properties? (chapter 5), (ii) since interfaces between centrosymmetric materials can be charged, are there other symmetries in different materials which also allow polar surfaces? (chapter 6), iii) are defects instead likely to play a role in the origin of the 2DEG? (chapter 7), and (iv) can these polarity arguments and screening models also apply to the prototypical polar materials - ferroelectrics? (chapter 8).

The specific objectives of the research presented in this thesis were:

1. **To understand the net charge at insulating interfaces, particularly the interface between  $\text{LaAlO}_3$  and  $\text{SrTiO}_3$ .**

Within Tasker's classification of polar surfaces (12) and the polar catastrophe mechanism for the LAO-STO interface (36), formal ionic charges are used to model the charge density at the interface. However perovskites and many other materials have a sizeable degree of covalency, and so it has been suggested that factors accounting for related charge density effects should be included (see them reviewed in ref. (27)). Chapter 3 attempts to consider these approaches for addressing the issue of the net charge at polar interfaces within the framework of the modern theory of polarisation (see chapter 2), and applies it the LAO-STO interface.

2. **To apply the net charge considerations to pristine  $\text{LaAlO}_3\text{-SrTiO}_3$  superlattices.**

If the net charge of the frozen bulk system is known and found to be non-zero, the system is susceptible to charge screening instabilities. As a first step, we aim in chapter 4 to understand these screening processes in pristine

(defect free) LAO-STO superlattices, by comparing an electrostatics analysis (using the frozen bulk net charge from objective 1) with first principles calculations.

- 3. To determine whether the effect of steps at the  $\text{LaAlO}_3\text{-SrTiO}_3$  interface influence the electronic properties.**

Chapter 5 aims to understand the effect on the interface net charge and related screening effects by small alterations to the pristine interface seen in essentially all grown samples - steps. Steps of one unit cell height in LAO-STO samples are known and have been characterised (47; 112; 113).

- 4. To understand whether the net charge arguments apply generally in systems with different symmetry.**

Objectives 1, 2 and 3 have concentrated on the LAO-STO system which is made up of two centrosymmetric materials. Chapter 6 aims to understand whether the net charge arguments are more general, by considering a completely different system with a new symmetry (three-fold rotational) - two-dimensional honeycomb compounds.

- 5. To model the effect and stability of surface defects in polar thin films.**

The origin of the 2DEG at the LAO-STO interface is still debated. Whilst the polar catastrophe is currently the most popular mechanism, several experimental observations have raised doubts. Chapter 7 considers a different mechanism, which is also stabilised through the internal electric field, but where the carriers appear through the creation of surface redox defects, such as oxygen vacancies. Chapter 8 considers a similar mechanism as a potential route to thin film ferroelectric stability.

## 1. INTRODUCTION

---

# Chapter 2

## Theoretical Methods

### Chapter Summary

The primary theoretical technique employed in this thesis is density functional theory (DFT). The goal of this chapter is to present the basic theory, with some of the key approximations, underlying the calculation of the ground state of a crystalline system. The methods which are summarised are implemented in the SIESTA code (114; 115), and have been used in the current work. It is beyond the scope of this chapter to provide a detailed review of DFT, which can be found for example in ref. (116).

The second half of this chapter summarises the formal concept of polarisation and its calculation from the electronic structure. The history of the problem is briefly reviewed beginning with the problems of the Clausius-Mossotti model, the difficulties of quantum-mechanical electrons with spread charge densities and the resolution of polarisation as an adiabatic flow of current with the Berry phase and Wannier function formalisms.

### 2.1 Density functional theory

#### 2.1.1 The Kohn-Sham Formalism

The many-body problem of interacting electrons and nuclei in the solid state is formidable and requires various approximations to make it computationally tractable. The first approximation, due to Born and Oppenheimer (117), enables the electronic and nuclear degrees of freedom of a system to be separated due to the relatively small mass of the electrons, allowing solution of the *time – independent* Schrödinger wave equation. The electrons therefore move in the electrostatic field of the nuclei but the calculation is still nontrivial in a real system with many atoms due to the large number of degrees of freedom. In 1964 Hohenberg and Kohn (118) formulated density functional theory (DFT) which reduced the degrees of freedom by introducing the *electron density* rather than the many-body wavefunction as the basic state variable. In this theory the energy of the system,  $E[n(\mathbf{r})]$ , is expressed as a unique functional of this electron density,  $n(\mathbf{r})$ , according to

$$E[n(\mathbf{r})] = \int V_{\text{ext}}(\mathbf{r})n(\mathbf{r})d^3\mathbf{r} + F[n(\mathbf{r})] \quad (2.1)$$

where  $V_{\text{ext}}(\mathbf{r})$  is an external electrostatic potential (due to the nuclei) and  $F[n(\mathbf{r})]$  is a unique functional of the electron density. Moreover the charge density that minimises  $E[n(\mathbf{r})]$  must be the *exact* ground-state density of the system, and the value of the energy functional for that density corresponds to the *exact* ground state energy. Since the form of  $F[n(\mathbf{r})]$  is unknown Kohn and Sham (119) subsequently approximated it as follows

$$F[n(\mathbf{r})] = T_0[n(\mathbf{r})] + E_{\text{H}}[n(\mathbf{r})] + E_{\text{xc}}[n(\mathbf{r})] \quad (2.2)$$

where  $T_0[n(\mathbf{r})]$  is the kinetic energy of a system of non-interacting particles with density  $n(\mathbf{r})$ ,  $E_{\text{H}}[n(\mathbf{r})]$  is the Hartree energy due to the Coulombic repulsion of electrons and  $E_{\text{xc}}[n(\mathbf{r})]$  is the exchange-correlation energy. The exchange-correlation term should not only include exchange and correlation energies but

## 2.1 Density functional theory

---

also the difference between  $T_0[n(\mathbf{r})]$  and the true kinetic energy of the interacting system, however its exact form is unknown. In addition Kohn and Sham expressed the electron density as a sum over  $N$  *single particle* wavefunctions,  $\psi_i(\mathbf{r})$ , given by

$$n(\mathbf{r}) = \sum_{i=1}^N |\psi_i(\mathbf{r})|^2 \quad (2.3)$$

Each of the terms in equation 2.2 are represented by

$$T_0[n(\mathbf{r})] = - \sum_{i=1}^N \frac{\hbar^2}{2m} \int \psi_i^*(\mathbf{r}) \nabla^2 \psi_i(\mathbf{r}) d^3\mathbf{r} \quad (2.4)$$

$$E_H[n(\mathbf{r})] = \frac{e^2}{2} \int \frac{n(\mathbf{r})n(\mathbf{r}')}{|\mathbf{r} - \mathbf{r}'|} d^3\mathbf{r}d^3\mathbf{r}' \quad (2.5)$$

$$E_{xc}^{\text{LDA}}[n(\mathbf{r})] = \int \varepsilon_{xc}(\mathbf{r})n(\mathbf{r})d\mathbf{r} \quad (2.6)$$

Equation 2.6 is the *local density approximation* (LDA) to the exchange correlation-energy as defined in (119) where  $\varepsilon_{xc}(\mathbf{r})$  is the exchange-correlation energy of a homogeneous electron gas. In the *local spin density approximation* (LSDA) the role of spin is described by explicitly considering the density of up and down spins. In the *generalised gradient approximation* (GGA) the exchange-correlation energy of a system at a given point depends not only on the electron density at that point but also the gradient of the electron density there,  $|\nabla n(\mathbf{r})|$  (120; 121):

$$E_{xc}^{\text{GGA}}[n(\mathbf{r})] = \int f[n(\mathbf{r}), |\nabla n(\mathbf{r})|]d^3\mathbf{r} \quad (2.7)$$

GGA takes better account of inhomogeneities in the electron density than LDA.

The Kohn-Sham wave equation, obtained from a variational minimisation of equation 2.1 subject to the constraint of particle number conservation, is expressed as,

$$\left[ -\frac{\hbar^2}{2m} \nabla^2 + V_{\text{eff}}(\mathbf{r}) \right] \psi_i(\mathbf{r}) = \varepsilon_i \psi_i(\mathbf{r}) \quad (2.8)$$

where  $\varepsilon_i$  are the single particle eigenvalues, and  $V_{\text{eff}}(\mathbf{r}) = V_H(\mathbf{r}) + V_{\text{ext}}(\mathbf{r}) + V_{xc}$ , where  $V_{\text{ext}}(\mathbf{r})$  is the external potential due to the nuclei and

$$V_H = \frac{\delta E_H}{\delta n(\mathbf{r})} \quad (2.9)$$

## 2. THEORETICAL METHODS

---

$$V_{xc} = \frac{\delta E_{xc}}{\delta n(\mathbf{r})} \quad (2.10)$$

are the Hartree and exchange correlation potentials respectively. The result of the Kohn-Sham approach is to transform the problem of  $N$  interacting electrons to solving  $N$  independent Schrödinger equations for non-interacting electrons moving in an effective potential (the sum of the Hartree, external and exchange correlation potentials). Equation 2.8 is the Kohn-Sham equation which is a non-linear differential equation and must be solved *self-consistently* from an initial trial electron density until the effective potential and the resulting charge density are consistent. This self-consistency loop is illustrated in ref (122). In practice each iteration of this self-consistency loop within the SIESTA method involves solving a slightly adapted secular equation of 2.8. Firstly the hamiltonian and overlap matrices are built (using a localised basis set, see below), and then the secular equation is solved either by direct diagonalisation or minimisation of an energy functional.

In the Kohn-Sham formalism, the electron density must be determined (using equation 2.3) in all space. In practice the problem is simplified in the SIESTA method by calculating the density on a real space grid (115), whose fineness is controlled by a maximum energy cut-off which can be compared to the kinetic energy cut-off in plane wave basis set methods. For integrals over the first Brillouin zone (required for example when calculating the energy, forces and the density of states) the problem is similarly simplified by replacing the integrals with a reciprocal space mesh of special points, implemented in the Monkhorst and Pack scheme (123).

The sum of  $\varepsilon_i$  is the total energy of the fictitious system of non-interacting particles. The total energy of the ‘real’ system is then the sum of  $\varepsilon_i$  plus double count correction terms. It should be noted that only the highest occupied eigenvalue has physical meaning (124). Similarly the Kohn-Sham single-particle wavefunctions  $\psi_i(\mathbf{r})$  only relate to the true many-body wavefunction through the same ground state electron density.

### 2.1.2 Basis set

Solving the Kohn-Sham equations requires a mathematical representation of the single particle wavefunction. There are several representations, or basis sets, to choose from (the most popular being plane waves). The SIESTA code (114; 115) uses the linear combination of atomic orbitals (LCAO) basis set,

$$\psi_i(\mathbf{r}) = \sum_{Ilmn} c_{iIlmn} \phi_{Ilmn}(\mathbf{r}) \quad (2.11)$$

where the electron wavefunction is represented as a sum over all atomic orbitals for all the atoms,  $\phi_{Ilmn}(\mathbf{r})$ , multiplied by a corresponding coefficient,  $c_{iIlmn}$ , for atom  $I$  with  $l$  and  $m$  the angular momentum quantum numbers and  $n$  is the radial orbital number. One of the advantages of the LCAO basis set is that they can be strictly confined, i.e. zero beyond a cut-off radius (SIESTA uses the scheme of Ref. (125) or Ref. (126)). This locality of the basis can allow for a linear scaling of computational time with system size, termed order- $N$ , instead of the order- $N^3$  scaling typically found in most codes. Within this cut-off radius, the atomic orbitals are products of a numerical radial function and a spherical harmonic. For atom  $I$  located at  $\mathbf{R}_I$ ,

$$\phi_{Ilmn}(\mathbf{r}) = \phi_{Il n}(|\mathbf{r}|_I) Y_{lm}(\hat{\mathbf{r}}_I) \quad (2.12)$$

where  $\mathbf{r}_I = \mathbf{r} - \mathbf{R}_I$ . Even if the shape of the atomic orbitals is known qualitatively, it is not trivial to find an analytical function that accurately represents them. One option is to use sets of decaying exponentials or Gaussians, however many functions per orbital are usually required. The SIESTA code abandons the analytical form and represents the basis functions numerically to save computational costs. Minimal basis sets (single- $\zeta$ ) with only one numerical radial function per angular momentum orbital have been found suitable for semi-quantitative simulations. For higher accuracy it is possible to introduce more numerical functions per orbital (multiple- $\zeta$ ) and polarisation orbitals which account for angular flexibility due to deformation induced by bond formation. In practice polarisation orbitals

## 2. THEORETICAL METHODS

---

are either generated for an angular momentum one higher than the highest occupied orbital, or by using an atomic orbital of lower angular momentum subject to a small electric field.

### 2.1.3 The pseudopotential approximation

A pseudopotential is an approximation to the true electrostatic electron-nucleus interaction. In the pseudopotential approximation the core electrons closest to the nucleus are grouped with the nucleus to create a rigid ion. The interaction between the remaining valence electrons and the rigid ion constitutes the pseudopotential. One advantage of replacing the electron-nucleus interaction with an effective electron-ion interaction is that it softens the strongly diverging Coulomb potential near the nucleus. Additionally it replaces the strongly oscillating valence wavefunction near the nucleus with a smoother, nodeless pseudowavefunction. Furthermore the use of pseudopotentials replaces the need to obtain the core states which are highly energetic and localised, and thus computationally expensive. Provided certain criteria are met then the pseudopotential is a good representation of the true all electron-nucleus interaction. For example the norm-conserving pseudopotentials used in this thesis, preserve the same energy levels for the valence wave-functions as in the all-electron case, the shape of the wave-function outside the core region, and the total charge in the core region.

A brief mention of some of the specific features of the pseudopotentials used here: i) The pseudo charge density is equal to the true density beyond a defined cut-off radii, ii) The pseudopotentials are norm conserving (127) (the norm of the pseudowavefunction is equal to that of the true wavefunction), iii) The pseudopotential is semi-local, which is composed of both angular momentum dependent (called non-local), and to reduce computational expense, angular momentum independent (local) parts, and iv) The pseudopotentials in some cases include core corrections (128), which attempts to treat the nonlinear exchange-correlation potential between core and valence charges.

### 2.1.4 Periodic solids

To practically describe a bulk crystalline system, which is periodic but infinite in size, it is necessary to reduce the problem to a finite system. The periodicity of the crystal implies that the effective potential in the non-interacting wave equation 2.8, has the same periodicity as the crystal itself, i.e.  $V_{\text{eff}}(\mathbf{r}) = V_{\text{eff}}(\mathbf{r} + \mathbf{a})$ , where  $\mathbf{a}$  is a Bravais lattice vector.

Bloch's theorem allows the electron wavefunction in the periodic potential to be written as a product of a plane wave envelope with a periodic function,  $u_{n\mathbf{k}}(\mathbf{r})$ ,

$$\psi_{n\mathbf{k}}(\mathbf{r}) = e^{i\mathbf{k}\cdot\mathbf{r}} u_{n\mathbf{k}}(\mathbf{r}) \quad (2.13)$$

where the periodic part of the Bloch function has the same periodicity as the crystal, i.e.  $u_{n\mathbf{k}}(\mathbf{r}) = u_{n\mathbf{k}}(\mathbf{r} + \mathbf{a})$ , characterised by  $\mathbf{k}$ , the reciprocal lattice vector spanning the Brillouin zone and  $n$ , the band index. The problem has been reduced from an infinite number of wavefunctions, to a finite number within the Brillouin zone.

Periodic boundary conditions has become a widely used technique, not only for purely infinite systems with three-dimensional periodicity, but additionally aperiodic systems with molecules, surfaces, interfaces and defects by adopting a supercell, in which the size of the cell is increased until the interaction between replicas becomes negligible.

### 2.1.5 Ionic forces and the Hellmann-Feynman theorem

In order to efficiently relax the atomic geometry the ionic forces are calculated. These forces consist of two terms: the classical Coulombic repulsion between the ions and the quantum mechanical contribution from the valence electrons. The first term may be calculated using standard Ewald summation techniques, which comprises of decomposing the electrostatics in to short and long range and solving each in real and reciprocal space respectively to optimise convergence. The second contribution,  $\mathbf{f}_I$ , may be expressed in terms of the electronic wavefunctions as

## 2. THEORETICAL METHODS

---

follows

$$\mathbf{f}_I = -\frac{dE}{d\mathbf{R}_I} = -\frac{\partial E}{\partial \mathbf{R}_I} - \sum_i \frac{\partial E}{\partial \psi_i} \frac{d\psi_i}{d\mathbf{R}_I} - \sum_i \frac{\partial E}{\partial \psi_i^*} \frac{d\psi_i^*}{d\mathbf{R}_I} \quad (2.14)$$

where  $E$  is the Kohn-Sham electronic energy and  $\mathbf{R}_I$  is the position of ion  $I$ . The Hellmann-Feynman theorem (129; 130) states that, provided the electronic system is at its ground state, the last two terms in the above equation sum to zero and therefore the forces on the ions due to the electrons is given by just the partial derivative of the electronic energy with respect to the ionic positions. A correction to the Hellmann-Feynman theorem is required when using an atomic orbital basis set. This is the Pulay correction and is required due to the dependence of the basis functions on the ionic positions (131). Once the total ionic force is obtained the ionic positions can be relaxed using an iterative line minimisation technique such as *steepest descents* or, in a faster modified form, *conjugate gradients* (122).

## 2.2 Theory of polarisation

Electric polarisation is an essential concept for the description of a dielectric. It also plays a key role in ferroelectricity, pyroelectricity and piezoelectricity. The traditional simplified textbook definition is the dipole moment per unit volume. However we will see that this definition causes problems for bulk materials. Despite polarisation being such a fundamental property, the resolution only came fairly recently in the early 1990's. In this section we present the background to the problem of defining polarisation using the charge density or idealised polarisable units as in the Clausius-Mossotti model, and the solution of turning to the Berry phase or Wannier centres within the modern theory of polarisation.

### 2.2.1 Problem with Clausius-Mossotti

The standard picture of polarisation within matter is the Clausius-Mossotti model where it is assumed the material can be split into identifiable polarisable units and the resulting polarisation is simply the dipole moment of these

point-like charges per unit volume. However this picture is neither realistic, nor accurate. For example, in ferroelectric oxides, the bonding is known to have a degree of covalent character (132), moving the valence electrons away from the atom centres, rendering a point charge model over-simplified and unrealistic.

However the problem is more general. Even if the full electron density of a periodic crystal is known, the polarisation as traditionally expressed is ill-defined,

$$\mathbf{P} = \frac{e}{\Omega} \left[ \sum_I Z_I \mathbf{R}_I - \int_{\Omega} \mathbf{r} n(\mathbf{r}) d\mathbf{r} \right] \quad (2.15)$$

where  $\Omega$  is the volume of the unit cell,  $Z_I$  are the valence atomic numbers, and the summations and integrals are over the unit cell. This is simply the dipole moment of the point-like atomic charges plus the delocalised electrons per unit volume. The result depends on the position of the unit cell; arbitrarily shifting the cell alters the polarisation continuously. In a finite material equation 2.15 becomes well defined when integrating over the whole sample. However the summation then includes surface effects, which cannot be easily separated from the bulk. Equation 2.15 is not a helpful description of polarisation in a *bulk* material. It is clear that the knowledge of the periodic charge density alone is not enough to construct a meaningful definition of the bulk polarisation. This problem was first highlighted in 1974 (133).

### 2.2.2 Polarisation as an adiabatic flow of current

The first breakthrough in the theory came nearly 20 years later, and was based on the standard experimental setup for measuring polarisation. This is based on measuring derivatives of the polarisation, actually current, with an external process, such as an electric field, strain or temperature. Access to a particular state is not available, only the difference between an initial and final state. For example in a ferroelectric, the difference in polarisation upon polarisation reversal is measured. The spontaneous polarisation is defined as half the difference between the two states, due to prior knowledge of the symmetry equivalence of the two

## 2. THEORETICAL METHODS

---

states. Without this knowledge, the polarisation of each state cannot be individually attained, only the difference. The change in polarisation during an adiabatic evolution of an external parameter,  $\lambda$ , can be defined using the integrated current flowing through the material,

$$\Delta\mathbf{P} = \int_{\lambda_1}^{\lambda_2} \mathbf{j}(\lambda) d\lambda \quad (2.16)$$

where  $\mathbf{j}(\lambda)$  is the cell-averaged current density, which implicitly depends on the external parameter. In order to relate this to the ferroelectric spontaneous polarisation, we define  $\lambda$  as a parameter proportional to the atomic displacements such that for the centrosymmetric reference phase,  $\lambda = 0$ , and for the spontaneous ferroelectric state,  $\lambda = 1$ . The spontaneous polarisation is (134),

$$\Delta\mathbf{P} = \int_0^1 d\lambda \frac{d\mathbf{P}}{d\lambda} \quad (2.17)$$

where  $d\mathbf{P}/d\lambda$  is importantly a well-defined bulk property, see next section. Equation 2.17 defines the effective polarisation for a state by using a centrosymmetric phase as zero polarisation reference. This is distinct from the formal polarisation which is defined later. The initial and final states can be more general and refer to the system before/after the slow application of any perturbation.

Equation 2.16 does not refer to the charge density, but the current. Whilst the density relates to the square of the modulus of the wavefunction, the current relates to the phase. As shown in the next chapter, this equation is the basis behind the modern theory of polarisation.

### 2.2.3 Berry phase theory of polarisation

We now briefly outline the central ideas of the Berry-phase theory of polarisation, which are described in detail in Refs. (30; 135; 136). We begin with the Bloch electrons previously mentioned in section 2.1.4. One can rewrite the Schrödinger wave equation using the periodic part to the Bloch functions,  $u_{n\mathbf{k}}(\mathbf{r})$ ,

$$H(\mathbf{k})u_{n\mathbf{k}}(\mathbf{r}) = \varepsilon_{n\mathbf{k}}u_{n\mathbf{k}}(\mathbf{r}) \quad (2.18)$$

with the corresponding Hamiltonian now,

$$H(\mathbf{k}) = \frac{(\mathbf{p} + \hbar\mathbf{k})^2}{2m} + V_{\text{eff}}(\mathbf{r}) \quad (2.19)$$

for independent electrons (as in DFT, equation 2.8). The Bloch electrons are associated with a corresponding Berry-connection (137),

$$\mathbf{A}(\mathbf{k}) = i \sum_n \langle u_{n\mathbf{k}} | \frac{\partial u_{n\mathbf{k}}}{\partial \mathbf{k}} \rangle \quad (2.20)$$

and a Berry phase (137),

$$\gamma(C) = \oint_C \mathbf{A}(\mathbf{k}) d\mathbf{k} = i \oint_C \sum_n \langle u_{n\mathbf{k}} | \frac{\partial u_{n\mathbf{k}}}{\partial \mathbf{k}} \rangle d\mathbf{k} \quad (2.21)$$

over the closed path  $C$  in  $\mathbf{k}$ -space, where the total Berry connection and phase is simply the sum of the components for the individual occupied Bloch bands.

King-Smith and Vanderbilt showed that the electronic polarisation is related elegantly to the Berry phase of the occupied Bloch bands (135). The theorem uses the momentum matrix elements, instead of position, the periodicity of the Bloch bands, and adiabatic perturbation theory with  $\lambda$  to show  $d\mathbf{P}/d\lambda$  is well defined in infinite crystal systems, and

$$\mathbf{P}_{\text{el}}^\lambda = \frac{ie}{(2\pi)^3} \sum_n \int d\mathbf{k} \langle u_{n\mathbf{k}}^\lambda | \frac{\partial u_{n\mathbf{k}}^\lambda}{\partial \mathbf{k}} \rangle = \frac{e}{(2\pi)^3} \gamma \quad (2.22)$$

where the integral is performed over the Brillouin zone, and the summation over only the occupied bands, and the  $\lambda$ -dependence of the polarisation and the periodic part of the Bloch functions has been explicitly shown for clarity. The electronic polarisation is hence proportional to the Berry phase of the occupied Bloch states. This is the key result of the modern theory of polarisation.

The total polarisation is the sum of electronic and ionic components. Using equation 2.15 for the ionic component,

$$\mathbf{P}^\lambda = \frac{ie}{(2\pi)^3} \sum_n \int d\mathbf{k} \langle u_{n\mathbf{k}}^\lambda | \frac{\partial u_{n\mathbf{k}}^\lambda}{\partial \mathbf{k}} \rangle + \frac{e}{\Omega} \sum_I Z_I \mathbf{R}_I \quad (2.23)$$

## 2. THEORETICAL METHODS

---

which is defined as the formal polarisation, distinct from the effective polarisation of equation 2.17. The two values are equal if the polarisation of the reference centrosymmetric structure used to define the effective polarisation is zero. This is not always the case, as found in several of the materials discussed within this thesis (see chapter 3).

In practice, for numerical implementations such as those within DFT, the integral over the Brillouin zone is performed in a discrete  $\mathbf{k}$ -grid (135). It should be noted that the formulations presented here are only well-defined for insulators.

### 2.2.4 Mapping on to Wannier centres

Wannier functions,  $W_n(\mathbf{r} - \mathbf{a})$ , are localised functions characterised by the band index,  $n$ , and lattice vector,  $\mathbf{a}$ , typically used as an intuitive picture of bonding in materials (for simplicity we restrict this discussion to bands which are not entangled, i.e. bands that are separated from all others by finite gaps within the Brillouin zone). They are defined by a Fourier transform of the Bloch functions,

$$W_n^\lambda(\mathbf{r} - \mathbf{a}) = \frac{\Omega}{(2\pi)^3} \int d\mathbf{k} e^{i\mathbf{k}\cdot(\mathbf{r}-\mathbf{a})} u_{n\mathbf{k}}^\lambda(\mathbf{r}) \quad (2.24)$$

A popular choice is the maximally localised Wannier functions (138), defined by the set of Wanniers that minimises the quadratic spread of the functions. The Wannier centre at  $\mathbf{a} = 0$  is found by (139),

$$\langle \mathbf{r} \rangle_n^\lambda = \langle W_n^\lambda | \mathbf{r} | W_n^\lambda \rangle = \frac{i\Omega}{(2\pi)^3} \int d\mathbf{k} \langle u_{n\mathbf{k}}^\lambda | \frac{\partial u_{n\mathbf{k}}^\lambda}{\partial \mathbf{k}} \rangle \quad (2.25)$$

The relation with polarisation becomes clear when comparing this with equation 2.22. By inspection of equations 2.22 and 2.25 the electronic polarisation can be defined as the dipole moment per unit volume of the occupied Wannier centres (134; 135),

$$\mathbf{P}_{\text{el}}^\lambda = \frac{e}{\Omega} \sum \langle \mathbf{r} \rangle_n^\lambda \quad (2.26)$$

Hence the polarisation using the sum of Berry phases of the Bloch bands is equivalent to simply the location of the Wannier centres. The Wannier centres then

provide an intuitive picture of the polarisation in crystals. In fact the Clausius-Mossotti model is recovered - using Wannier centres is essentially the same as decomposing the crystal charge in to point charges. However it should be noted that the phase of the Bloch orbitals, not just the modulus, is essential in determining the Wannier centres.

### 2.2.5 Polarisation as a multivalued vector - the quantum

A further glance at equations 2.22 and 2.26 and we can see that the polarisation is a well-defined quantity modulo  $\frac{e}{\Omega}\mathbf{a}$ , with  $\mathbf{a}$  any lattice vector. This may seem surprising, however even the classical definition of the ionic polarisation (left hand side of equation 2.15) has the same uncertainty, due to the arbitrariness of the nuclear positions,  $\mathbf{R}_I$ , modulo a lattice vector  $\mathbf{a}$ .

Therefore it is helpful to think of the polarisation not as a single-valued quantity, but a multivalued vector quantity. In other words, the polarisation is a lattice of vectors in three-dimensions, distanced by translations of  $\frac{e}{\Omega}\mathbf{a}$ .

Chapter 3 continues the discussion of polarisation, concentrating on an example of a centrosymmetric crystal where the lattice of polarisation vectors is, perhaps surprisingly, not centred at zero. The issue of surface and interface charge is addressed in these materials.

## 2. THEORETICAL METHODS

---

# Chapter 3

## The net charge at interfaces between insulators

### Chapter Summary

Following from the theory of polarisation in chapter 2 the issue of the net charge at insulating interfaces is briefly reviewed with the aim of showing that such charges are unaffected by covalency and related charge density effects. For electrostatic analysis purposes, the net charge is defined by counting discrete electrons and core ion charges, and by the reference polarisation of the separate, unperturbed bulk materials. The arguments are illustrated for the insulating  $\text{LaAlO}_3\text{-SrTiO}_3$  interface, for which the net charge is exactly  $0.5e$  per interface formula unit, if the polarisation response in both materials is referred to zero. Further consequences are presented for chemical alterations at interfaces, in which internal and extrinsic processes are distinguished. The arguments are reviewed alongside the proposal of Stengel and Vanderbilt [Phys. Rev. B **80**, 241103 (2009)] of using formal polarisation values, based on the interface theorem of Vanderbilt and King-Smith [Phys. Rev. B **48**, 4442 (1993)].<sup>1</sup>

---

<sup>1</sup>The discussions presented in this chapter have been published in the article of Bristowe, Littlewood, and Artacho J. Phys.: Condens. Matter **23**, 081001 (2011) (28).

### 3. THE NET CHARGE AT INTERFACES BETWEEN INSULATORS

---

#### 3.1 Introduction

When Ohtomo and Hwang (35) discovered a two-dimensional electron gas at a pristine insulator-insulator interface, they rationalised their finding in terms of the electrostatics of formally charged ions. Namely,  $-2e$  for O,  $+4e$  for Ti,  $+2e$  for Sr, and  $+3e$  for Al and La, respectively, for the  $\text{LaAlO}_3/\text{SrTiO}_3$  (001) interface (LAO/STO). With such charges the alternating (001) SrO and  $\text{TiO}_2$  atomic layers of the perovskite structure of STO are neutral, while the LAO corresponding layers, LaO and  $\text{AlO}_2$ , are charged as  $+1e$  and  $-1e$  per formula unit, respectively. These net layer charges give rise to an imbalance at the interface giving a net charge of  $\pm 0.5e$  per interface formula unit (the sign depending on whether the interface is SrO/ $\text{AlO}_2$  or LaO/ $\text{TiO}_2$ ). This basic argument is at the heart of all the subsequent work in what has become a very hot topic (47; 48; 49; 50; 51).

It is well known, however, that formal charges represent quite an idealised picture of the electronic distribution in these far from ideally ionic insulators, in which covalency effects (notably in Al-O and Ti-O bonds) are not at all negligible. Indeed, many papers with quantitative modelling of the electrostatics allow for covalency effects, and thus a reduction of the interface effective charge.

#### 3.2 Basic argument

The intention of this note is to dispel covalency myths when dealing with the electrostatics of these systems (as reviewed in e.g. Ref. (27)): if the bulk polarisation of both materials is taken as zero, the effective charge of these pristine band-insulating interfaces is exactly as obtained from counting formal charges as done in the original paper (35), absolutely irrespective of ionicity or covalency considerations. It is exactly  $0.5e$  per formula unit for LAO/STO (in the absence of free carriers trapped at the interface, which will be assumed here unless explicitly stated).

The key to the argument is that what matters is charge counting, not the

## 3.2 Basic argument

---

shape of the charge density. This is not new, it has already been said for these systems (see Ref. (140), also implicit in Ref. (141)), but was already understood for polar/non-polar semiconductor interfaces (142) and formalised in Ref. (30). It is the old argument for understanding doping in semiconductors. Take phosphorous as a donor in bulk silicon. Its +5 core is surrounded by the same set of bonds that surrounded the Si +4 core it substitutes. These bonds can be described by electron pairs in localised Wannier functions (e.g. maximally localised Wannier functions (138)). These functions may be deformed as compared to what they would be in the pristine material, but the number of such functions remains, since they relate to the number of bands in the valence band. Take a large enough region around the dopant. The number of electrons in that region described by the full valence band is identical to the number in the same region without the dopant substitution. Since the core is +5 instead of +4, the net charge is precisely  $+1e$ . The fifth electron of P is then shallowly bound to that charge, in a hydrogenic Rydberg state below the conduction band, defined by the effective mass of the relevant conduction-band minimum, the dielectric constant of the material (which describes the deformation of the bonds around the dopant), and  $Z = +1$ .

In the LAO/STO system the interface is no longer a point defect and has a different material at each side. However, the valence bands of both LAO and STO give rise to four Wannier functions per O atom. This does not mean that they are on O in an ideal ionic form, in fact they are strongly deformed towards the Ti or Al nuclei, as polar covalent bonds. It is just a counting consideration, similar to that of there being two bonds per atom in a Si crystal. Counting core ionic charges and the valence electrons that way gives exactly the same charges as the formal charges used by Ohtomo and Hwang (35). As long as these Wannier functions localise over length scales smaller than the relevant system size (the LAO film thickness in the case at hand), using “polarisation-free” unit cells (27) allows to obtain the net interface charging of  $0.5e$  per formula unit.

### 3. THE NET CHARGE AT INTERFACES BETWEEN INSULATORS

---

#### 3.3 Formal discussion

The need to resort to such “polarisation-free cells”, however, reflects the fact that the definition of the net charge, albeit basic, is subtle. Let us review the argument more formally. In the “macroscopic” electrostatics we are interested in (length scales larger than atomic; extended to microscopics in Refs. (143; 144)) electric fields and charges relate through Gauss’s law,  $\nabla \cdot \mathbf{D} = \rho$ , i.e., the divergence of the electric displacement field equals the volume density of free charges (free meaning beyond the bound charges of the dielectric). The displacement combines the electric field  $\mathcal{E}$  and the material’s polarisation  $\mathbf{P}$  through  $\mathbf{D} = \epsilon_0 \mathcal{E} + \mathbf{P}$ , with  $\epsilon_0$  the dielectric permittivity of vacuum. For an interface, Gauss’s law becomes  $D_z^L - D_z^R = \sigma$ , where  $z$  is taken as the direction normal to the interface, L and R indicate the materials at either side of the interface (left and right), and  $\sigma$  stands for the area density of free charges associated to the interface. Thus,  $\epsilon_0(\mathcal{E}_z^L - \mathcal{E}_z^R) = \sigma - (P_z^L - P_z^R)$ , or  $\epsilon_0 \Delta \mathcal{E}_z = \sigma - \Delta P_z$ . In this work the charge per unit area of  $P$  and  $\sigma$  are expressed as electron charges per interface formula unit,  $e/\text{f.u.}$  The interface area associated to a STO perovskite f.u. is  $\sim 16 \text{ \AA}^2$ .

The subtlety in the problem arises from the polarisation definition, and, related, what is meant by “free charges”. Remember that we consider the interface with no free carriers, and thus no free charges in a strict sense. The net charge we are discussing plays the same role, however, given that it is not described by polarisation. It has been called compositional charge (145). The value of the polarisation in each material depends on the electric field acting in it. Such polarisation response to the electric field in the structure is not discussed in this chapter, it is explicitly considered in the electrostatic modelling of the interface system, either with an explicit  $P$  or by a dielectric constant (see Ref. (140) and chapter 4 for an example in this context). The key is the reference polarisation of the separated, unperturbed bulk materials (zero of polarisation), since a change in that reference changes  $\sigma$  by the same amount. There are two aspects to this.

(i) The usual experimental determinations of polarisation in a material give

### 3.3 Formal discussion

---

the change in polarisation between two states, but has no access to an absolute value for each state separately. Centrosymmetric materials (as LAO and STO) offer a natural definition of zero polarisation, thus allowing the definition of an *effective* polarisation, as the change in polarisation when the structure deviates from the centrosymmetric one (we follow the name convention of Ref. (141)). Switchable non-centrosymmetric solids (ferroelectrics) also have a natural zero of polarisation. Other non-centrosymmetric cases do not, and are discussed below.

(*ii*) The determination of polarisation from theory is not straightforward either. In a system of classical point charges, the polarisation of the bulk material can be obtained as the dipole moment of the unit cell divided by the unit-cell volume. This is ambiguous, however, since it depends on how the unit cell is defined. Take for instance a linear chain of equidistant, alternating  $+q$  and  $-q$  point charges (see figure 3.1). If you take the unit cell as having  $+q$  on the left and  $-q$  on the right, you get a different polarisation than if you choose it the other way around (actually, you get the same value with opposite sign). You can also choose your cell by taking  $+q$  in the centre, and one half of the  $-q$  charge at either end of the unit cell. This choice achieves zero polarisation by splitting the charge. If an interface is made to a similar chain of neutral particles (figure 3.1), the following descriptions are equivalent: (*i*)  $\Delta P = -q/2$  and net interface charge  $Q = 0$ ; (*ii*)  $\Delta P = +q/2$  and  $Q = -q$ ; or (*iii*)  $\Delta P = 0$  and  $Q = -q/2$ . In all cases, however, the change in electric field remains the same, since  $\epsilon_0 \Delta \mathcal{E} = Q - \Delta P = -q/2$ . It trivially maps to our three-dimensional system, the point being that different bulk polarisation reference definitions can be used, requiring a consistent redefinition of the interface charge. The original paper (35) and most that followed used the split-charge trick on the formal charges of the layers. Note an alternative technique to determine the ‘excess’ charge (146) which addresses the problem from a different angle based on chemical thermodynamics.

Quantum-mechanical electrons pose additional difficulties to the definition of the bulk polarisation of a solid (133), given their spread charge density: When

### 3. THE NET CHARGE AT INTERFACES BETWEEN INSULATORS

---

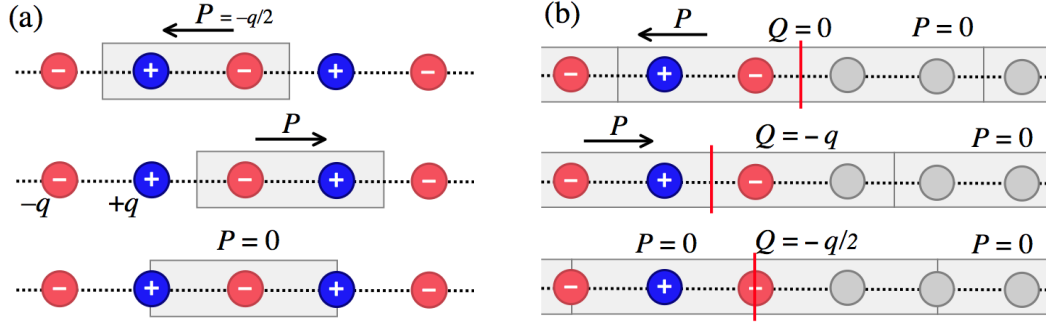


Figure 3.1: (a) Polarisation  $P$  values in a one-dimensional system of alternating  $\pm q$  charges. As dipole moment per unit length,  $P = q(a/2)/a = q/2 = P^0/2$ , where  $P^0$  is a quantum of polarisation (in the real system  $q = e$ ). (b) Interface charge  $Q$  for an interface of the previous chain with one of neutral charges. The different values of  $Q$  are associated to the definition of  $P$ .

displacing the unit cell, there is a continuous unphysical change of  $P$  if defined as above, instead of the jumps of quanta discussed above. For the point at hand, however, it is sufficient to know that towards calculating  $P$  the modern theory of polarisation (135; 136) allows to map the electronic wave functions in a material onto a classical system of point charges, using the centres of charge of the Wannier functions associated to the valence bands (138) (see chapter 2 for further details). Taking the ionic cores and the Wannier centres in a unit cell as point charges, the polarisation of any material can be defined as above, running onto the same arbitrariness. Equally, the inversion symmetry allows taking both bulk phases of LAO and STO with  $P = 0$  (taking the ‘effective’ polarisation - see section 3.4). The counting of charges (core charges and Wannier charges), gives the same  $0.5e/\text{f.u.}$  (for a figure illustrating it for the LAO/STO interface, see Figure 1 of Ref. (141)).

### 3.3.1 Symmetry considerations

The well defined polarisation reference for bulk centrosymmetric solids has been explicitly used above.<sup>1</sup> It is more general than it seems. The vast majority of symmetry breaking displacive instabilities in perovskites either remain centrosymmetric or become ferroelectric, both allowing for a good definition of a polarisation zero.

The situation is different for non-centrosymmetric non-switchable solids. In such a case, the definition of an effective polarisation taking as reference the one found in the unperturbed solid remains quite arbitrary. It actually changes with temperature (pyroelectricity). The zero temperature limit can then be used (as defined in (141)), but it still remains unsatisfactorily arbitrary. The key here is that for any interface involving such a solid, any unit cell definition giving zero polarisation would give an arbitrary fractional charge at the interface, apparently calling for ionicity/covalency considerations at the interface (142; 147). The muddled situation generated by the lack of symmetry in these materials clears below.

## 3.4 Formal versus effective polarisation

Stengel and Vanderbilt (141) propose a more elegant alternative view on this problem based on the so-called interface theorem (30). They start with the fact that the charge density entering Gauss’s law is that of free charges while “bound” charges are described by the polarisation term in the displacement field. The net compositional charge discussed here is neither. A more natural solution appears when considering the *formal* values of polarisation of both materials instead of their *effective* values (141). The former is as obtained by direct application of the modern theory of polarisation mentioned above (135) (e.g. considering the ionic cores and the centres of charge of Wannier functions as point charges (138)), which

---

<sup>1</sup>Note that, although we make the case for inversion, the only invariance needed here is that of any symmetry transforming  $z$  into  $-z$ . See Ref. (30) for a more general discussion.

### 3. THE NET CHARGE AT INTERFACES BETWEEN INSULATORS

---

offers a well defined zero reference. The difference between the two definitions gives precisely  $0.5e/f.u.$ : The formal  $P_z$  for STO is zero, while for LAO it is  $0.5e/f.u.$  (see Ref. (141)). With these values for the respective bulk polarisations, the ‘free’ charge at the interface is now zero (see first case in figure 3.1).

#### 3.4.1 Polarisation quanta and symmetry

It is interesting to see how these two polarisation values come about. In a system of discrete point charges, the polarisation is defined up to polarisation quanta: finite jumps of the polarisation when displacing the bulk unit cell along a crystallographic direction. A jump occurs when the edge of the unit cell reaches one of the point charges, which disappears there and reappears on the other side of the cell, and thus the dipole moment for the unit cell is changed by  $qa$ , the charge of the point-like particle that flipped, times the length of the cell in the direction of the flip. The polarisation changes by  $qa/\Omega$ , where  $\Omega$  is the unit cell volume, or  $q/S$ , with  $S$  the area of the unit cell normal to the flip direction. With  $e$  as the charge quantum, the quantum of polarisation in a given direction  $P^0$  is  $1e/S$ , and in our case  $P^0 = 1e/f.u.$

In these flips the system does not change at all, only our description of it. Such jumps in the value of  $P$  have thus no physical meaning. A meaningful polarisation value is thus modulo polarisation quanta. In other words, the whole set  $\{P+nP^0\}$  ( $n$  being any integer) corresponds to one only value. In our problem, only two  $P_z$  values are allowed if the material is centrosymmetric:  $P_z = 0$  or  $P_z = P^0/2$ , corresponding to the sets  $P_z = \{\dots - 2P^0, -P^0, 0, P^0, 2P^0, \dots\}$  (as for, e.g., STO) and  $P_z = \{\dots - 3P^0/2, -P^0/2, P^0/2, 3P^0/2, \dots\}$  (as for, e.g., LAO), respectively, since these are the only such sets that are invariant under change of sign. This is the key difference with our discussion in the previous section, in which the *effective* polarisation of any centrosymmetric system was defined to be always zero, instead of zero or  $P^0/2$ .

## 3.5 Further implications

### 3.5.1 Non-centrosymmetric non-ferroelectric materials

The proposal of using formal values of the polarisation is even more interesting if the materials are neither centrosymmetric nor ferroelectric, as is the case of III-V semiconductors as GaAs or GaN, as they interface with a non-polar one as Si (take (111) interfaces for diamond/sphalerite structures, (001) for wurtzite). The trick used in the previous section (take zero-polarisation materials at each side), is quite contrived since, for the polar material, one has to split a point charge into two arbitrary bits to be put at each side of the cell in order to get  $P = 0$ . It leaves some inconvenient non-zero value of net interface charge (one of the bits, actually equal to the formal value of the polarisation). The consideration (and calculation) of the formal polarisation as such, however, simplifies matters, implying zero compositional charge at the interface. This is concluded following the same procedure as before: *(i)* take the system as made of point charges associated to the ionic cores and the Wannier centres, *(ii)* define your unit cells such that all charges are accounted for at the interface (i.e. the unit cells coming from each material either side of the interface are periodic translations of each other - they do not overlap or leave space missing at the interface), *(iii)* consider the corresponding formal polarisation values arising from the choice of unit cell; and *(iv)* count the charge of the interface unit cell. The apparent “covalency” issue that appeared at the interface reduces to the formal value of the polarisation in the bulk materials. The bond covalency/ionicity factors introduced in the past (147) or other charge density, or charge-density “topology” considerations (see them reviewed in (27)) are not addressing the problem from the right angle.

### 3.5.2 Polarisation quanta and relative polarisation

Going back to centrosymmetric perovskites, consider now the interface between  $\text{KTaO}_3$  and  $\text{LaAlO}_3$  (KTO/LAO). The formal polarisation for both ma-

### 3. THE NET CHARGE AT INTERFACES BETWEEN INSULATORS

---

materials taken separately is  $P^0/2$ . Taking these values and assuming zero compositional charge would be wrong, however. This can be seen if computing the compositional charge as in section 3.3. In this case, while in LAO the  $\text{AlO}_2$  planes are have a  $-1$  charge, and the  $\text{LaO}$  planes are  $+1$ , in  $\text{KTaO}$  it is the other way around:  $\text{TaO}_2$  planes are  $+1$ , while  $\text{KO}$  planes are  $-1$ . The two possible interfaces would then be  $\text{TaO}_2/\text{LaO}$ , or  $\text{KO}/\text{AlO}_2$ , which gives net compositional charges of  $-e/\text{f.u.}$  and  $+e/\text{f.u.}$ , respectively, which coincide with  $\pm P^0$ . A quantum of polarisation can thus have physical meaning. It does when determining the relative polarisation of the two materials. One can define the formal polarisation of one material with an arbitrary number of added polarisation quanta, but the condition of zero compositional charge at the interface completely defines the polarisation of the material at the other side of the interface. In this case  $\sigma_{\text{comp}} = 0$  if taking  $P = P^0/2$  for one and  $P = -P^0/2$  for the other. See also chapter 6 for an example of relative polarisation in 2D hexagonal compounds.

#### 3.5.3 Interface effects

So far we have assumed perfect interfaces *and* thin two-dimensional charge distributions. In this section we briefly explore the effect of deviations from such assumptions in chemically altered interfaces.

##### 3.5.3.1 Internal rearrangements: intermixing

Both during and after sample growth there is the possibility of inter-diffusion of atoms across the interface. Such processes have attracted attention lately (36; 102; 103; 105) as one of the possible explanations for the origin of 2D conduction in  $\text{LAO}/\text{STO}$  interfaces. The argument used is simply that, since  $\text{La}$  is a known dopant (donor) in  $\text{STO}$ ,  $\text{La}$  cations diffusing from  $\text{LAO}$  into  $\text{STO}$  could dope the interface and thus make it conducting.

Let us consider here what to expect from ions exchanging across the interface. This discussion will focus on the effects of having a given inter-diffusion profile

### 3.5 Further implications

---

in a sample, rather than the energetics and kinetics that might originate it, since equilibrium is not expected to be reached in this aspect. We shall concentrate here on inter-diffusion situations starting from the pristine stoichiometric interface, and all the exchanges happening within a region around the interface whose width is smaller than other length scales in the problem. The effects on deviations from stoichiometry, and of diffusion processes from/to reservoirs extrinsic to the interface, are qualitatively different and will be treated briefly below.

Based on chemical (steric) arguments and on quite a wealth of accumulated knowledge on perovskites, the most likely inter-diffusion processes by far are swaps of like atoms, namely, B cations ( $\text{Al}^{3+}$  cations in LAO substituted by  $\text{Ti}^{4+}$ , or  $\text{Ti}^{4+}$  in STO substituted by  $\text{Al}^{3+}$ ) and A cations ( $\text{La}^{3+}$  to  $\text{Sr}^{2+}$  on one side,  $\text{Sr}^{2+}$  to  $\text{La}^{3+}$  on the other). The swap of  $\text{O}^{2-}$  anions across the interface is also likely, but of no consequence. Each cation substitution gives rise to a net bound charge plus a compensating carrier. For example  $\text{La}^{3+}$  replacing  $\text{Sr}^{2+}$  gives a  $+e$  centre with an associated electron, thus the donor mentioned above.

The first important point to make here is that such inter-diffusion *should not be expected to dope the interface*. Be it A or B cations swapping across the interface, there will be as many “wrong” cations on one side as on the other, and thus as many donors at one side as acceptors at the other. The electrons of the donors annihilate with the holes of acceptors, as long as both dopants are located in the proximity of the interface, the situation considered here.

The second important point to make here is that such inter-diffusion does affect the electrostatics, but only in the interface region, it does not affect the electric field emanating from it into the film. This is a direct consequence of Gauss’s law: the net flux of the electric displacement field across surfaces parallel to the interface equals the net charge contained in the region within them. In the absence of charges raining in from other regions, the net charge per unit area is unaltered, and hence so is the difference in outgoing electric fields at either side of the interface,  $\Delta\mathcal{E}_z$ . The fields at either side can change, for instance,

### 3. THE NET CHARGE AT INTERFACES BETWEEN INSULATORS

---

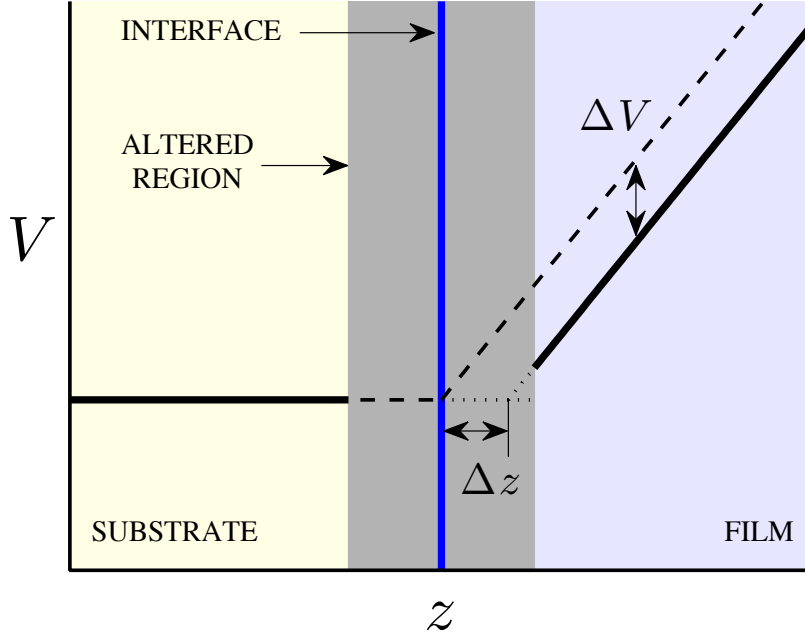


Figure 3.2: Electrostatics around an interface with  $\sigma_c$  the pristine interface net charge per unit area, around which there is a region with cation intermixing (dark grey band). Electrostatic potential energy  $V$  versus distance perpendicular to the interface  $z$ . The boundary condition is taken as constant potential on the side of the substrate. The slope of the outgoing potential to the right is  $\sigma_c/\epsilon$ , where  $\epsilon$  is the dielectric constant of the film (see chapter 4 for details of the dielectric response), regardless of the inter-diffusion, the latter producing a potential shift  $\Delta V$ , or apparent interface shift in position,  $\delta z$ .

by altering an interface dipole under fixed-bias boundary conditions. This is an indirect global effect, however, whereby a constant field is added to the whole system leaving  $\Delta\mathcal{E}_z$  invariant.

The main effect of cation inter-diffusion across the interface is illustrated in Figure 3.2: the electrostatic potential is shifted with respect to the one arising from a pristine interface. It is essentially the effect of the interface dipole generated by the swap of charges with its characteristic potential drop  $\Delta V$  (or raise). Alternatively, this effect can be interpreted as an effective shift of the interface

## 3.6 Final remarks and conclusions

---

position,  $\Delta z$  in the figure, i.e. a renormalisation of the film thickness.

The third point in this section is on the sign of such effect, depending on the two inter-diffusion cases, B or A cation exchanges. It is simple to show that the former, having Al and Ti ions exchanged, produces a drop of the electrostatic potential energy, or a right shift of the effective interface position, and would thus renormalise the film thickness to a smaller value. The latter produces the opposite. From a thermodynamic point of view, B cation inter-diffusion will be favoured by the electrostatics, whilst A cation inter-diffusion will tend to be suppressed.

### 3.5.3.2 Extrinsic processes: non-stoichiometry

The electrostatics are affected by extrinsic processes such as receiving free carriers, altering the stoichiometry at growth, or redox processes at the interface. They can also combine, like a remote redox process at the surface of a film that sends free carriers to a buried interface. An important redox process in these materials is the formation of O vacancies, whereby the pristine solid is reduced leaving two electron carriers. The vacancy becomes a centre with an effective  $Z = +2$  by the same arguments as in semiconductor doping (section 3.2): a double donor. In the bulk the two free electrons bind to the vacancy while in heterostructures they may find more stable residence elsewhere, in perfect analogy to what happens in semiconductor heterostructures. O vacancies on the surface of LAO may see their electrons transferred to the two-dimensional states at the buried STO/LAO interface (70; 148) (see chapter 7 for more details).

## 3.6 Final remarks and conclusions

As a final remark let us note that although the examples illustrating this discussion have been drawn from band insulators (doubly occupied Wannier functions), the arguments are more general and include Mott insulators, as long as

### 3. THE NET CHARGE AT INTERFACES BETWEEN INSULATORS

---

there is a well defined gap (think in terms of spin-polarised wave-functions and their corresponding, singly occupied Wannier functions). This is so for interfaces but also for point defects.

In conclusion we have reviewed the issue of the net charge at interfaces between insulators. In an attempt to dispel myths of such charges being affected by covalency and related charge density effects, we have presented a case for the counting of discrete electrons and core ion charges or equivalently the use of the formal polarisation value. The arguments are illustrated for the popular LAO/STO interface and additionally for non-centrosymmetric materials and for interfaces for which the charge mismatch is an integer number of polarisation quanta.

The remaining chapters in this thesis are divided in to two categories; chapters 4, 5 and 6 describe the resulting electrostatics and an electronic screening mechanism at pristine interfaces, whilst chapters 7 and 8 study an extrinsic screening mechanism and its energetics in ultra thin films.

# Chapter 4

## Oxide superlattices with alternating $n$ and $p$ interfaces

### Chapter Summary

In the last chapter the net charge at the LAO/STO interface was argued to be precisely  $\pm 0.5$  electrons per two-dimensional (2D) unit cell. This chapter considers the resulting electrostatic analysis of a superlattice system with alternating positively ( $n$ -type) and negatively ( $p$ -type) charged interfaces. A model of charged capacitor plates offers a simple paradigm to understand their dielectric properties and the insulator to metal transition (IMT) at interfaces with increasing layer thickness. The model is supported by first-principles results based on density-functional theory. The charge at insulating interfaces is argued and found to be as predicted from the formal ionic charges, not populations. Different relative layer thicknesses produce a spontaneous polarisation of the system, and allow manipulation of the interfacial electron gas. Large piezoresistance effects can be obtained from the sensitivity of the IMT to lateral strain. Carrier densities are found to be ideal for exciton condensation.<sup>1</sup>

---

<sup>1</sup>The results presented in this chapter have been published in the article of Bristowe, Artacho and Littlewood Phys. Rev. B **80**, 045425 (2009) (140).

## 4. OXIDE SUPERLATTICES WITH ALTERNATING $N$ AND $P$ INTERFACES

---

### 4.1 Introduction and methods

Recent technological advances have enabled the fabrication of high quality oxide multilayers, revealing a wealth of fascinating new physics. One striking example is the  $\text{LaAlO}_3/\text{SrTiO}_3$  system (LAO/STO). In 2004, Ohtomo and Hwang (35) discovered that the interface between these two perovskite band insulators can be conducting, depending on the termination of both materials. Many experimental and theoretical studies immediately followed (for a review see refs. (45; 46; 47; 48; 49; 50; 51)). Charge compensation at the interface of thick layers is required to avoid the so-called polar catastrophe. It arises from the diverging electrostatic potential caused by the net electric charge at these interfaces resulting from the fact that the (001) monolayers of STO are neutral while the ones of LAO are charged. The  $\text{TiO}_2$ -LaO interface (termed  $n$ ) needs 0.5 electrons per two-dimensional (2D) unit cell, and the SrO- $\text{AlO}_2$  interface ( $p$ ) 0.5 holes to avoid this polar catastrophe. Such numbers are based on formal ionic charges, i.e.,  $\text{Ti}^{+4}$ ,  $\text{Sr}^{+2}$ ,  $\text{La}^{+3}$ ,  $\text{Al}^{+3}$ , and  $\text{O}^{-2}$ , although it is well known that the charge distribution in these materials is far from being so ideally ionic. Formal charges are often downscaled by so-called covalency parameters that aim to describe more realistic charges (27).

These compensating electrons and holes are confined to the interface regions, but highly mobile in 2D, defining 2D electron and hole gases (72; 84). Huijben *et al.* (62) (see (85) for the theory) studied a system with one  $p$  and one  $n$  interface, finding 2D conduction beyond a critical interface separation of five unit cells. Characteristics like carrier mobility depend on the carrier density, which grows with separation beyond the critical value (94). Multilayers with both  $p$  and  $n$  interfaces with such a control of carrier density provide promising systems for obtaining the so-far elusive excitonic insulator (149), a new playground for Bose condensation effects. Recent experiments have demonstrated that oxygen vacancies can be controlled, while still allowing metallic conduction attributed to a 2D layer (56; 58).

This chapter focuses on LAO/STO superlattices with alternating  $p$  and  $n$  interfaces. We consider pristine systems, with no point defects (the effect of oxygen vacancies (82; 150) is discussed briefly at the end, and in more detail in chapter 7). Considering an equal thickness for both materials, an IMT is found by our calculations based on density-functional theory (DFT) for a thickness of just over eight unit cells. The electrostatic potential obtained in the calculations agrees remarkably well with a simple model of capacitor plates, giving an almost constant field of opposite sign in both materials, which does not change with increasing thickness until the potential drop coincides with the band gap. At that critical thickness electrons transfer from the  $p$  to the  $n$  interface, making them conducting, and pinning the potential drop.

The DFT calculations were done using the local density approximation (151) and the SIESTA method (114; 115). Norm-conserving pseudopotentials (127) were used, considering normal cores for O and Al, while semi-core electrons were included in the valence for La(5s5p), Sr(4s4p) and Ti(3s3p). Double- $\zeta$  polarised bases were used for valence electrons (152). Integrals in real space were performed on a mesh of 250 Ry cut-off (115), while Brillouin zone integrations were done on a  $k$ -mesh of 30 Å cut-off (as defined in ref. (153)). Four unit cells of STO in its ideal perovskite structure were layered on top of four of LAO, the 4/4 superlattice containing both TiO<sub>2</sub>-LaO and SrO-AlO<sub>2</sub> terminations. The lateral lattice parameter was set to the theoretical average for the two materials. The cell size was relaxed perpendicular to the interface ( $z$ ) along with the atomic positions until the forces were below 15 meV/Å. Samples for 8/8 and 12/12 unit cells were equally prepared. Other DFT studies (72; 73; 82; 84; 85; 92; 94; 150; 154; 155; 156), have focused on single interfaces of either kind, on arrays of repeated interfaces, or on alternating  $p$  and  $n$  interfaces. The latter (92; 150; 154) have considered four unit cells or less, too thin to observe the physics discussed here.

### 4.2 Results and discussion

The band structures of the three superlattices are presented in Figure 4.1. The band gap is indirect and reduces with interface separation, closing for the 12/12 system, with holes and electrons separated in reciprocal space. The behaviour in real space is shown in Figure 4.2 for the 12/12 case using the density of states projected onto each bilayer. The macroscopic average (143) of the electrostatic potential is plotted alongside.

The physics of the problem is apparent in this figure. The net electric charge of chemical origin at the interfaces establish electric fields among them, defining a zig-zag potential, which is closely followed by the band structure of both materials. The IMT occurs when the amplitude of the zig-zag is larger than the band gap (the valence band offsets are small in this scale, approximately 0.2 eV for the  $p$  and 0.0 eV for the  $n$  interfaces <sup>1</sup>). At this point holes appear confined in  $z$  around the  $\text{AlO}_2$  plane of the  $p$  interface, and around the  $\bar{M}$  point in the 2D Brillouin zone, while electrons are confined to the  $\text{TiO}_2$  plane at the  $n$  interface, and around  $\bar{\Gamma}$ . The 2D electron gas (2DEG) is dominated by a Ti  $3d$  character. It is nicely parabolic with an effective mass of  $0.4 m_e$ . The several parallel sub-bands at this interface correspond to excitations under the effective confining potential for electrons along  $z$  (figure 4.4a) <sup>2</sup>.

Quantitative predictions for the IMT are biased by the known band-gap problem of Kohn-Sham fermions (159). Constrained DFT calculations as used for charge-transfer systems (160) can be used for ours, but are beyond the scope of this work, its focus being the elucidation of the main mechanisms at play. In addition, it has been argued that, being  $\text{LaTiO}_3$  a system with highly correlated

---

<sup>1</sup>Offsets estimated from inspection of the layer by layer projected density of states. A more accurate determination, such as that presented in ref. (157), is not required here since the errors involved are too small to significantly effect the results

<sup>2</sup>Ref. (158) solves electron confinement in a V-shaped potential. The 2DEG states in this chapter are confined by different physics (4.4a) and for a different system.

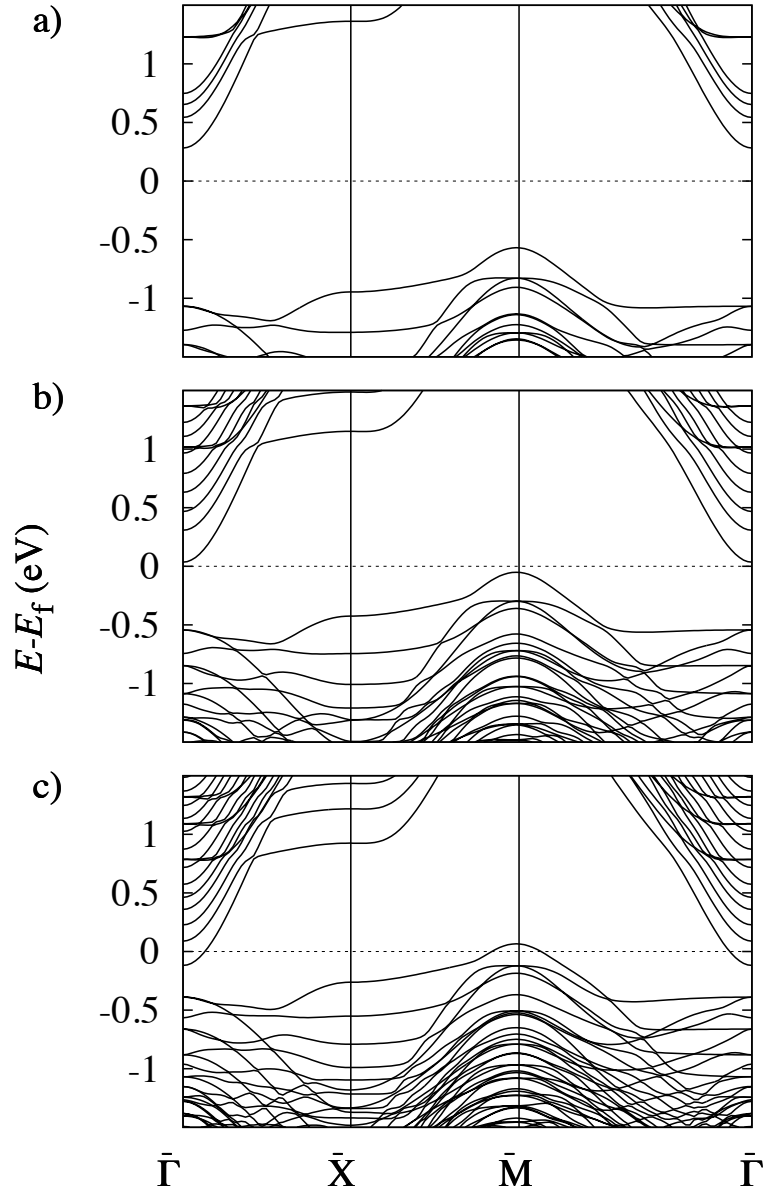


Figure 4.1: Band structures of three  $\text{LaAlO}_3/\text{SrTiO}_3$  superlattices with (a) 4/4, (b) 8/8, and (c) 12/12 unit-cell thicknesses.

#### 4. OXIDE SUPERLATTICES WITH ALTERNATING $N$ AND $P$ INTERFACES

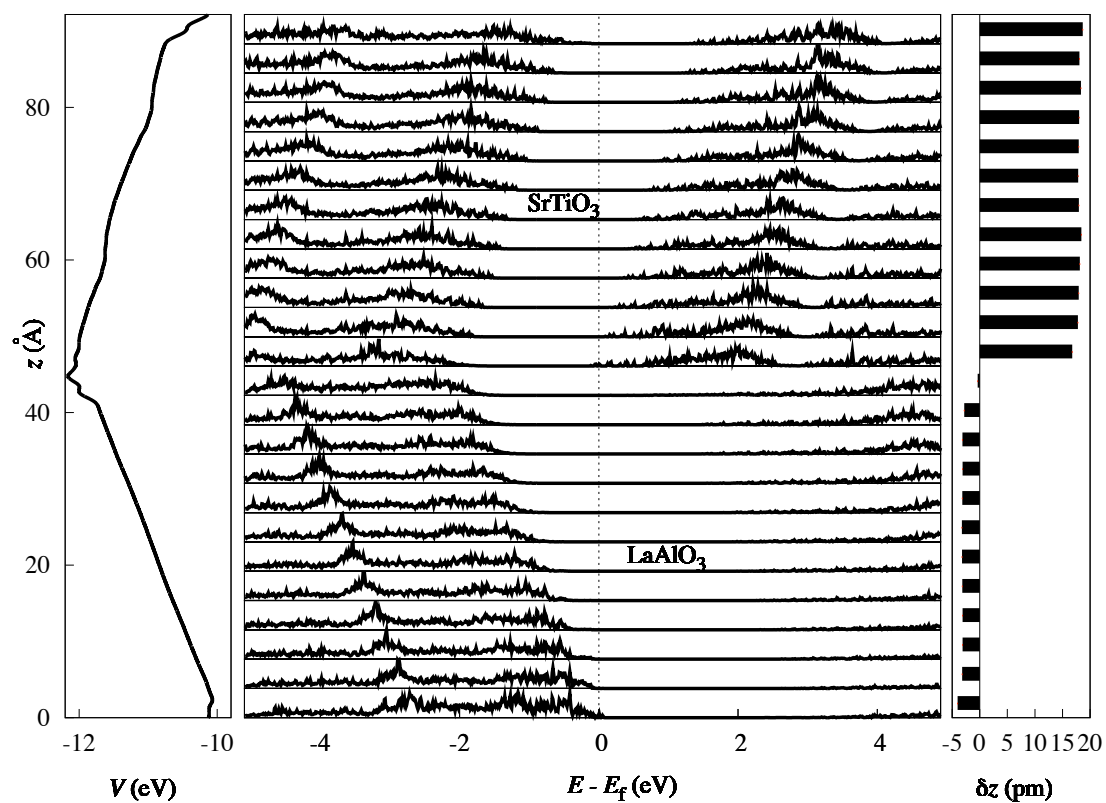


Figure 4.2: Centre: Density of states projected on unit-cell bilayers for the 12/12 superlattice. Left: Averaged (143) electrostatic potential energy for electrons as a function of  $z$ . Right: The anion-cation splitting of the  $\text{TiO}_2$  planes in  $\text{SrTiO}_3$  and  $\text{LaO}$  planes in  $\text{LaAlO}_3$  (larger splitting in each material), with  $\delta z = z_{\text{cation}} - z_{\text{anion}}$ .

electrons in the Ti  $3d$  band, methods addressing strong correlations are needed for our system. Note that this is not the case, however, since our IMT is in the limit of zero occupation of the  $3d$  band, hardly a correlated system, unlike  $\text{LaTiO}_3$ , which has one  $3d$  electron per Ti atom.

The deviations from the zig-zag behaviour of the potential are small in the scale of its amplitude, allowing the definition of a net electric field through each material. Its magnitude is nearly equal in both materials despite their different dielectric response. Such response is illustrated in figure 4.2 by the  $z$ -splitting of cations and anions at each layer, which is much larger for STO as expected. The fields obtained are  $57.3 \text{ mV}/\text{\AA}$  ( $5.73 \text{ MV}/\text{cm}$ ) and  $57.1 \text{ mV}/\text{\AA}$  ( $5.71 \text{ MV}/\text{cm}$ ) for the 4/4 and 8/8 superlattices, while the 12/12 sees it reduced to  $37.8 \text{ mV}/\text{\AA}$  ( $3.78 \text{ MV}/\text{cm}$ ) due to the partial charge back-transfer<sup>1</sup>. The field values correlate with the difference in sub-band separation seen in figure 4.1. An estimate of the 2DEG width  $w$  is obtained from  $w \sim E_{\text{ZPE}}/\mathcal{E}$ , i.e. the zero-point energy (ZPE) for the confining potential, over its slope, the electric field. Taking for 8/8,  $\mathcal{E} = 57 \text{ mV}/\text{\AA}$  and  $E_{\text{ZPE}} \sim 0.2 \text{ eV}$  (estimated from a Wentzel-Kramers-Brillouin solution to a triangular well) gives  $w \sim 4 \text{ \AA}$ .

### 4.2.1 Model of charged plates

The physics described can be further analysed with a simple model. The insulating system is modelled by a sequence of capacitor plates, one per interface, separated by dielectric material, as sketched in figure 4.3. Each plate has a planar charge density of chemical origin  $\sigma_c$  (the  $0.5e$  per interface unit cell described above and in chapter 3), positive at the  $n$  interface, negative for the  $p$ . Using Gauss's law, periodic boundary conditions (PBC), and equal thicknesses, there

---

<sup>1</sup> These fields are comparable with the dielectric breakdown of STO and LAO thin films, however progress in growth techniques has seen values reach in excess of  $6 \text{ MV}/\text{cm}$  (161; 162). In any case, here we are interested in pristine thin films. The effect of defects are discussed further in chapter 7.

#### 4. OXIDE SUPERLATTICES WITH ALTERNATING $N$ AND $P$ INTERFACES

---

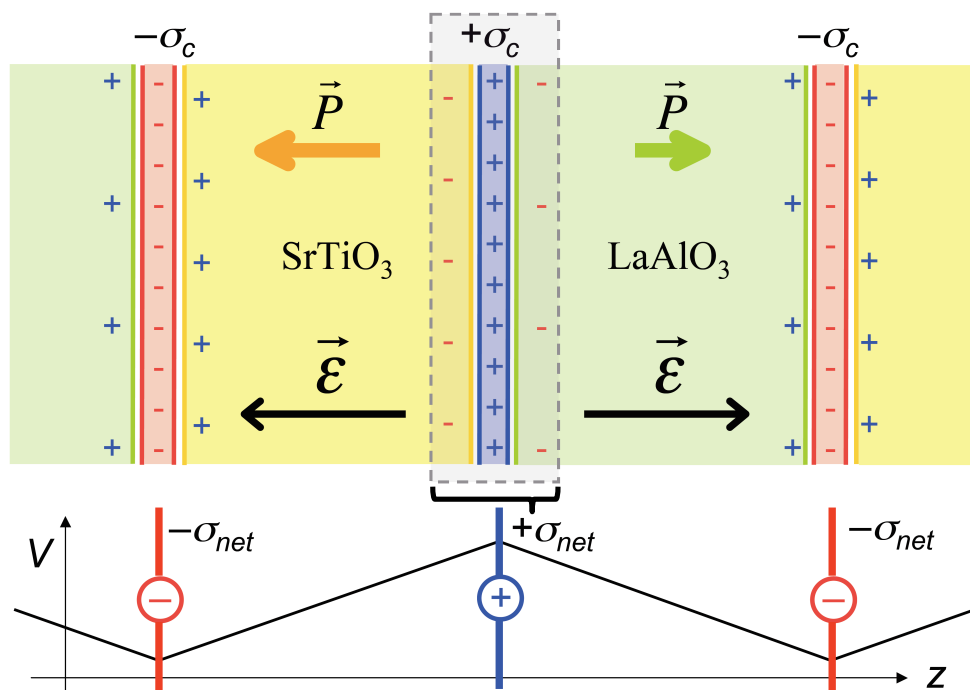


Figure 4.3: Capacitor-plates model of the LAO/STO superlattice. Above, the plates are indicated by the thinner bands, and  $\sigma_c$  indicates the charge of chemical origin attached to each, which is equal but of opposite sign for alternating interfaces. The box around the central plate indicates the surfaces for integration of Gauss's law. The lower panel shows the net electrostatic potential  $V$  for the system, which can be seen as arising from plates with  $\sigma_{net} = \sigma_c - P_{\text{LAO}} - P_{\text{STO}}$ , the latter  $P_{\text{LAO}}$  and  $P_{\text{STO}}$  referring to the magnitude of the respective polarisations (notice that  $V$  has opposite sign to what shown in the left panel of figure 4.2, which is  $qV$ ).

is a uniform electric field of magnitude  $\mathcal{E}^0$  pointing outwards from the  $n$  interface that satisfies

$$\sigma_c - P_{\text{LAO}} - P_{\text{STO}} = 2\epsilon_0\mathcal{E}^0, \quad (4.1)$$

with  $P_{\text{LAO}}$  and  $P_{\text{STO}}$  the magnitude of the respective polarisations of both materials under the field, and  $\epsilon_0$  the dielectric permittivity of vacuum. The left hand side is what is indicated by  $\sigma_{\text{net}}$  in figure 4.3. The behaviour at the  $p$  interface is exactly opposite, with the field now pointing towards the plate. The fields have equal magnitude in both materials even if both polarisations are different.

Finding  $\mathcal{E}^0$  requires knowing  $P(\mathcal{E})$  beyond linear response, at least for paraelectric STO. However under the strain conditions imposed by our geometry, the bulk of STO presents a spontaneous polarisation along  $z$  (163; 164). This allows for a simpler modelling than for unstrained paraelectric STO (since  $P(\mathcal{E})$  can now be approximated as linear with an offset), and offers an upper bound in the response, which corresponds to an upper bound to the critical thickness for the IMT. We take  $P_{\text{LAO}} = \epsilon_0\chi_{\text{LAO}}\mathcal{E}$  and  $P_{\text{STO}} = P_{\text{s(STO)}} + \epsilon_0\chi_{\text{STO}}\mathcal{E}$ , where  $P_{\text{s(STO)}}$  is the spontaneous polarisation of STO. Defining  $\kappa = 2 + \chi_{\text{STO}} + \chi_{\text{LAO}}$ , equation 4.1 becomes

$$\mathcal{E}^0 = (\sigma_c - P_{\text{s(STO)}})/\epsilon_0\kappa. \quad (4.2)$$

We obtain  $P_{\text{s(STO)}} = 0.309 \text{ C/m}^2$  using the Berry phase approach (135) for bulk STO with the same strain conditions as in the multilayer. The lattice contribution to both susceptibilities is computed as in Ref. (164) from the phonons and the Born effective charges, which are obtained by finite differences of the forces and the polarisation, respectively (165).

The computed susceptibilities are  $\chi_{33}^{\text{ph}}(\text{LAO}) = 12.2$  and  $\chi_{33}^{\text{ph}}(\text{STO}) = 24.7$ . To these we add the electronic contribution taking it from  $\epsilon^\infty(\text{STO}) = 5.18$  (166) and  $\epsilon^\infty(\text{LAO}) = 4.77$  (167). Using these bulk quantities and  $\sigma_c = 0.5e$  per interface unit cell, an electric field of  $57.4 \text{ mV/\AA}$  is obtained, in excellent agreement with the superlattice DFT results.

## 4. OXIDE SUPERLATTICES WITH ALTERNATING $N$ AND $P$ INTERFACES

---

### 4.2.2 Chemical charge at interfaces

This agreement indicates that the physically meaningful charge  $\sigma_c$  is the one predicted by formal ionic charges, rather than populations, as discussed in detail in chapter 3. The reason is the same as for dopants in semiconductors, where irrespective of the charge distribution around the dopant, the net charge is the result of counting core charges on one hand and electrons in the valence band on the other. Take the example of phosphorous as a donor in bulk silicon. Its +5 core is surrounded by the same set of bonds that surrounded the Si +4 core it substitutes. The electron-pair clouds of these bonds are deformed (polarised), of course, but the number of electrons remains. The net effect is that the P donor creates an attractive potential for electrons that corresponds to a charge of  $+e$ , not an effective charge of any kind, the deformation of the bonds around being described by the dielectric constant of bulk silicon.

These arguments were generalised to interfaces three decades ago (142). The valence-band electron counting was performed in terms of bands, but it can also be done using Lewis pairs or localised Wannier states. In LAO and STO the valence band corresponds to four Wannier states per oxygen, which gives exactly the same numbers as when using formal charges. The local charge neutrality picture (27) can then be used as the easiest way to see the interface charging, but using formal charges, not effective ones. Whether atoms are chemically more or less ionic depends on the shape and displacement of the Wanniers from the O atom towards the cations, but is irrelevant here. What is relevant is the number of electron pairs and the fact that they localise over lengths much smaller than the interface separation.

### 4.2.3 Insulator to metal transition

The IMT occurs at the critical thickness of  $d_c = \Delta/\mathcal{E}^0$ , where  $\Delta$  is the gap (STO's), including the ZPE for the confining potential at both interfaces (figure

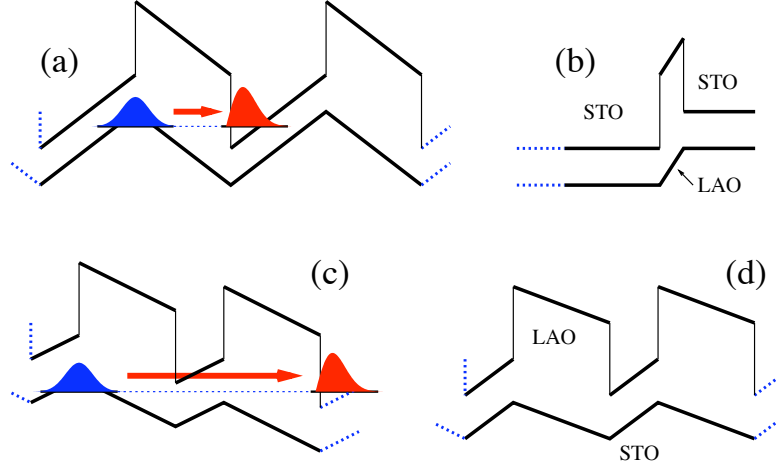


Figure 4.4: Model band gap versus  $z$  for a superlattice with equal thicknesses (a), the thin film sample of ref. (62) (b), and a superlattice with different thicknesses with open (c) and periodic (d) boundary conditions. In (a) and (c) the arrow indicates the charge transfer leading to electron (red) and hole (blue) 2D gases. In both cases the thicknesses depicted give the onset of the charge transfer, corresponding to the insulator to metal transition.

4.4a). Taking the calculated  $\mathcal{E}^0$ , our DFT gap for strained STO (1.78 eV), and both ZPEs as  $\sim 0.2$  eV, a  $d_c = 38 \text{ \AA}$  is obtained,  $\sim 10$  unit cells. This value is sensitive to lateral strain, since  $P(\mathcal{E})$  depends on strain (especially for STO, so close to a ferroelectric instability). Indeed, repeating the DFT calculation for 8/8 under the lateral lattice parameter of bulk STO gives conducting interfaces. This effect can be used to sense applied strain, or in reverse using strain to switch the 2DEG, on a sample tuned to be close to the IMT (a piezoresistance device). In fact since the publication of this chapter (140), exactly this effect was found experimentally (168).

Beyond the IMT, a constant density of states for holes and electrons is assumed, modelling 2D parabolic bands. Considering electron transfer from the  $p$

## 4. OXIDE SUPERLATTICES WITH ALTERNATING $N$ AND $P$ INTERFACES

---

to the  $n$  interface, equation 4.1 becomes

$$\sigma_c - P_{\text{LAO}} - P_{\text{STO}} - (\mathcal{E}d - \Delta)g = 2\epsilon_0\mathcal{E} \quad (4.3)$$

where  $d$  is the interface separation,  $\mathcal{E}$  the modified field, and  $g$  the density of states (taking equal effective masses for electrons and holes). Proceeding as for equation 4.2,

$$\mathcal{E} = (\sigma_c + g\Delta - P_{\text{s(STO)}})/(\epsilon_0\kappa + gd). \quad (4.4)$$

The electric field vanishes as  $1/d$  for large separations, the charge transferred tending to compensate the chemical charge. In our case,  $g\Delta \gg \sigma_c$ , and thus  $\mathcal{E}/\mathcal{E}^0 \sim d_c/d$ , i.e. the voltage drop is essentially pinned by the gap. Using the calculated  $d_c$ ,  $d_c/d_{12} \approx 2/3$ . The electric fields obtained from DFT for the 12/12 and 8/8 systems give a ratio of  $0.662 \approx 2/3$ .

### 4.2.4 Extending the model to other systems

Consider now the model for other systems. Take a superlattice with thicker layers for LAO than for STO (figure 4.4c). It is analogous to a frozen  $\langle 111 \rangle$  LO phonon in NaCl: the different separations of the charged planes gives a net electric field. PBC remove it as if putting the system between shorted metal plates (figure 4.4d). It is as a ferroelectric, except that switching the spontaneous polarisation demands changing the thicknesses. Note that with PBC and thinner STO,  $\mathcal{E}_{\text{STO}} > \mathcal{E}_{\text{LAO}}$ . Without shorted plates the system is unstable to the appearance of 2DEGs (figure 4.4c).

The  $d_c$  found experimentally on the non-repeated system of ref. (62) is much smaller than our superlattice result. They grew an LAO layer sandwiched between an STO substrate and an STO capping layer, such that the interface between LAO and the substrate is  $n$ -type, and the interface between LAO and the capping layer is  $p$ -type (figure 4.4b). The field is zero in the substrate and overlayer, the  $p$  and  $n$  interfaces defining a capacitor only screened by LAO. Thus,  $\mathcal{E} = \sigma_c/\epsilon_0(1 + \chi_{\text{LAO}})$ ,

more than twice as large as  $\mathcal{E}^0$  of equation 4.2<sup>1</sup>. The critical thickness also depends on the band gap, which is underestimated within DFT by less than factor of two ( $\Delta_{\text{DFT}} = 1.78$  eV and  $\Delta_{\text{exp}} = 3.2$  eV). The two effects reduce the ratio,  $d_c = \Delta/\mathcal{E}^0$ , and hence also the experimental critical thickness of ref. (62) compared with the DFT superlattice calculations here.

### 4.3 Final remarks and summary

The electron-hole interactions among 2D gases should establish bound states, i.e. excitons. Achievable exciton densities are favourable for exciton condensation, the optimal density being (149)  $n_{\text{opt}} = (\pi a_0^2)^{-1}$ , with  $a_0^2 \approx (a_B \epsilon / m_{\text{eff}})^2 + d^2$  (with  $a_B$  the Bohr radius,  $\epsilon$  the dielectric constant and  $m_{\text{eff}}$  the effective mass). For the superlattice system  $n_{\text{opt}} \approx 0.002e/\text{cell}$ , which is well within range ( $n_{12/12} = 0.073e/\text{cell}$ ).

The IMT is affected by the presence of O vacancies. Each donates two electrons to the  $n$  interface giving rise to a 2DEG. Their appearance and location depends on their stability and on kinetic effects like electromigration and sample-growth history. Chapter 7 considers the stability of the vacancies as an alternative mechanism to the IMT presented here.

In summary, the agreement between DFT and the model shows that it contains the relevant physics of these superlattices, pointing to new science and applications by changing relative thicknesses, substrates, and stress.

---

<sup>1</sup>A similar model has been recently described for one single  $n$  interface (86).

#### 4. OXIDE SUPERLATTICES WITH ALTERNATING $N$ AND $P$ INTERFACES

---

# Chapter 5

## Proposal of a one-dimensional electron gas in the steps at the LaAlO<sub>3</sub>-SrTiO<sub>3</sub> interface

### Chapter Summary

The previous chapter considered the origin of the two dimensional electron gas at pristine LAO/STO superlattices. Here we propose that a one-dimensional electron gas (1DEG) can be engineered at the step edges of vicinal LAO/STO interfaces. These predictions are supported by first principles calculations and electrostatic modelling which elucidate the origin of the 1DEG as an electronic reconstruction to compensate a net surface charge in the step edge. The results suggest a novel route to increasing the functional density in these electronic interfaces. <sup>1</sup>

---

<sup>1</sup>The results displayed in this chapter have been published in the article of Bristowe, Fix, Blamire, Littlewood and Artacho Phys. Rev. Lett. **108**, 166802 (2012) (169).

## 5. PROPOSAL OF A ONE-DIMENSIONAL ELECTRON GAS IN THE STEPS AT THE LAALO<sub>3</sub>-SRTIO<sub>3</sub> INTERFACE

---

### 5.1 Introduction

The two-dimensional electron gas (2DEG) at the interface between two band insulators, LaAlO<sub>3</sub> (LAO) and SrTiO<sub>3</sub> (STO), has become the prototypical system for the study of novel electronic phases at oxide interfaces. Since the original discovery (35) it has been shown that at low temperatures the 2DEG may become magnetic (95), superconducting (98), or both coexisting in one phase (99; 100). At room temperature the LAO-STO interface may find applications in field-effect devices (58; 70), sensors (170) or nano photo-detectors (171).

The origin of the 2DEG is still under debate, but one potential mechanism, called the “electronic reconstruction” (36), is currently the most popular (51). At the heart of this mechanism is the notion that LAO has a non-zero polarisation,  $P$  (28; 141), which for thin films, translates to having polar surfaces/interfaces along certain crystallographic directions (30), (including (001) - the most common growth direction in practice). Polar surfaces are electrostatically unstable but one possible route to charge compensate is via a transfer of electrons between the surface of the film and the interface. For a LAO film grown on a TiO<sub>2</sub> terminated STO (001) substrate, complete compensation would amount to precisely  $0.5 e/S$  (where  $S$  is the area of the (001) plane associated to one formula unit) transferring from the LAO surface to the interface, creating the 2DEG. Incomplete, or no compensation may occur for ultrathin LAO films, where the internal potential drop is lower than the relevant effective gap (in this case the band gap of STO). This is consistent with the observation of a critical LAO thickness,  $d_c$ , for 2DEG appearance (58). An alternative charge compensating mechanism is via surface oxygen vacancies (70) which is also consistent with the observed  $d_c$  (see Ref. (148) and chapter 7).

In this chapter we propose that steps at the interface, defects which are observed in practically all epitaxial films (due to a small miscut of the substrate by angle  $\theta$ ), can be utilised to produce one-dimensional electron gases (1DEG) residing at the step edge. We use a simple model to argue that a step of one unit

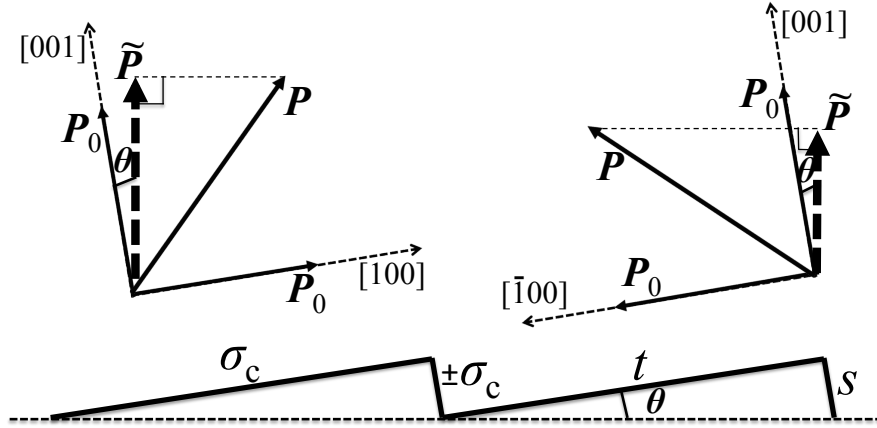


Figure 5.1: Schematic diagram illustrating the effect of steps on the net charge of the interface. Top: Polarisation argument considering LAO has a polarisation,  $P_0$  along the  $[100]$ ,  $[010]$  and  $[001]$  directions, with  $P$  the total, and  $\tilde{P}$  the net of the stepped interface. Bottom: an equivalent picture with charge densities  $\pm\sigma_c$  on the terrace and step edge, where  $s$  and  $t$  are the step and terrace distances respectively.

cell in height alters the polarity of the interface and surface of LAO, since the step edge itself has a net charge of  $e/2S$  (i.e. a charge line density of  $se/2S$ , with  $s$  the step height as in figure 5.1). An equivalent, and more rigorous, picture takes the component perpendicular to the stepped surface of the formal polarisation of LAO (figure 5.1), which is precisely (1,1,1)  $e/2S$  as shown later in this chapter. The electrostatics of the interface are studied with a simple capacitor plate model, supported with density functional theory (DFT) calculations, that shows an alteration of the interface carrier density with miscut angle. A 1DEG is predicted for small miscut angles when the LAO thickness is just below  $d_c(\theta = 0)$ , the critical thickness for metallicity in the zero miscut system.

## 5.2 Results and discussion

### 5.2.1 Polarisation model

We begin with a formal consideration of the polarity of stepped LAO surfaces. We define the miscut angle as  $\tan\theta = s/t$ , where  $s$  and  $t$  are the step and terrace distances respectively (see figure 5.1). The steps can be intentionally miscut along a certain direction (112; 113). We consider the [100] case here, but the arguments can be trivially applied to any miscut orientation. Atomic force microscopy (AFM) measurements of epitaxial LAO-STO suggest steps of 1 unit cell in height (112; 113). Neighbouring terraces of the surface are then of the same termination (BO<sub>2</sub> here), but the step edge may be terminated either AO or BO<sub>2</sub> (non-polar vicinal LAO surfaces have been considered in Ref. (29)). Perhaps the conceptually simplest picture is to take what has been called “chemical” (140) (or “compositional” (145)) charges,  $\sigma_c = 0.5e/S$ , along the terrace and step edges (figure 5.1 bottom). The total net charge of the surface,  $\tilde{\sigma}_c$ , is then  $\sigma_c(\cos\theta \pm \sin\theta)$ . The  $\pm$  depends on the step termination: addition if the step and terrace have the same terminations, and subtraction if they have opposite terminations. This result can be confirmed within the framework of the modern theory of polarisation (135). Taking the formal polarisation,  $P$ , defined by (136) the position of the ion cores and mapping the electronic wavefunction on to Wannier centres (138), one finds for cubic LAO  $P = \sqrt{3} e/2S$  along the [111] direction (29) modulo a quantum of polarisation. The component of this polarisation normal to the stepped surface (figure 5.1 top),  $\tilde{P}$ , is the net surface charge density and precisely the same as the above “chemical” charge. For tetragonal LAO (as in the case of epitaxial thin films), a trivial correction may be applied to the above through a redefinition of  $S$ .

### 5.2.2 DFT calculations

To support this picture, density functional theory (DFT) calculations were performed on two model LAO-STO systems <sup>1</sup>:  $n$ - $n$  superlattices, and  $n$ - $p$  films.  $n$  and  $p$  denote the termination of LAO terraces ( $n$  - LaO,  $p$  - AlO<sub>2</sub>). Note that in both cases, the steps are created by simply altering one of the supercell vectors - there is no change in stoichiometry through the introduction of steps. The DFT calculations were performed using the Wu-Cohen exchange correlation functional (172) as implemented in the SIESTA code (114; 115). Details of the pseudopotentials and atomic-orbitals basis are given in Ref. (140). Atomic forces were relaxed to less than 40 meV/Å. We begin with  $n$ - $n$  superlattices (figure 5.2).

Figure 5.2 shows the effect of steps on the electronic structure of the  $n$ - $n$  superlattice. The superlattice was constructed from 4.5 unit cells of LAO and 8.5 unit cells of STO stacked along the [001] direction. Steps were introduced by taking a supercell and altering the  $\mathbf{a}$  supercell vector to  $t\mathbf{a}+s\mathbf{c}$  (see figure 5.2 left). This produces  $n$ -type steps along one interface and  $p$ -type steps along the other while maintaining exactly the same stoichiometry ( $n$  and  $p$  here denote the step edge termination, in the same manner as above for the terrace). Figure 5.2 shows the case of  $t=3$  and  $s=1$ . In the system without steps (which we call the pristine system) the Ti 3d conduction electrons distribute evenly between the two  $n$ -type terraces -  $0.5 e/S$  at each interface with a decay through the STO slab (figure 5.2 centre), consistent with previous DFT calculations (84; 94). The inclusion of steps is found to transfer electrons from one interface to the other (figure 5.2 right), accumulating near the  $n$ -type steps, and depleting near the  $p$ -type steps, with respect to the pristine system. The total density of electrons transferred is approximately  $0.1e/S$  (20% of  $\sigma_c$ ). This is consistent with the number required to screen the bound charge density of each interface, including the step charges, as predicted by the model. This model system clearly shows a large effect of

---

<sup>1</sup>The effect of the DFT band gap error in LAO-STO is discussed extensively in the literature (see e.g. Ref. (148)) and is easily corrected for within the model (equation 5.1).

## 5. PROPOSAL OF A ONE-DIMENSIONAL ELECTRON GAS IN THE STEPS AT THE LAALO<sub>3</sub>-SRTIO<sub>3</sub> INTERFACE

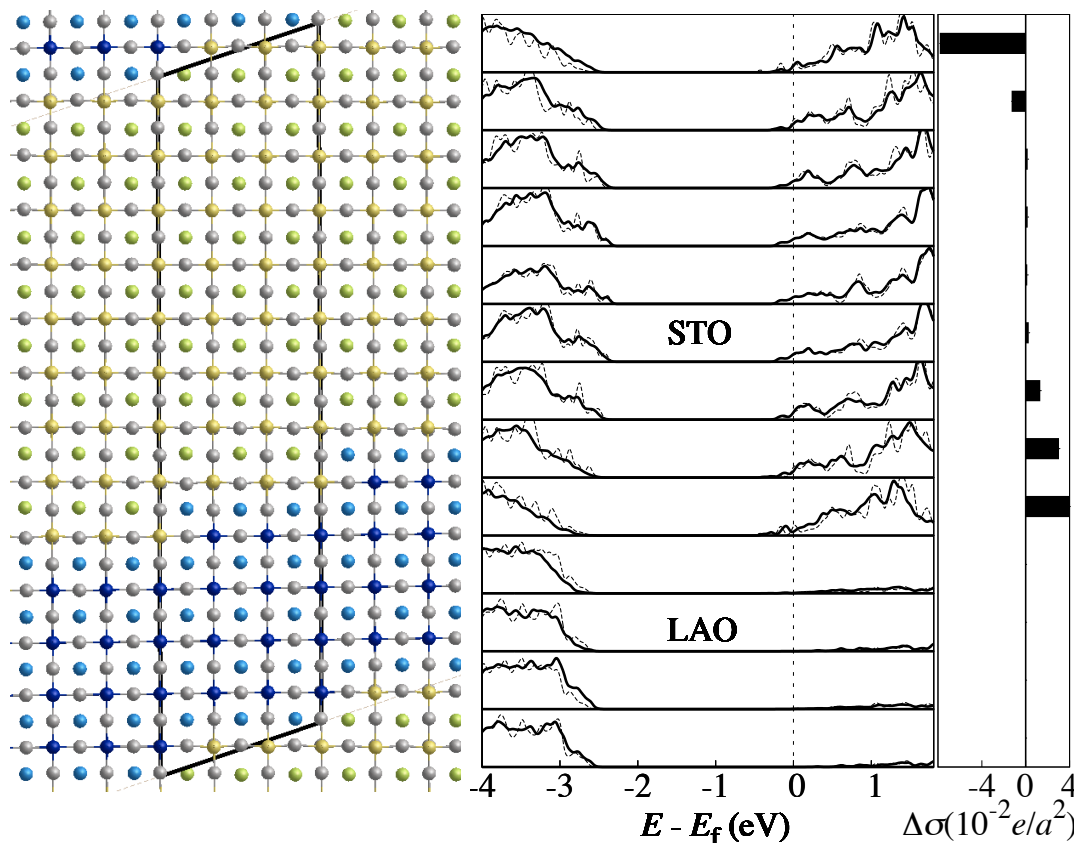


Figure 5.2: Left: The DFT simulation cell of the LAO/STO superlattice. The two interface terrace terminations are both  $\text{TiO}_2\text{-LaO}$  ( $n$ -type) whereas the interface step termination is  $n$ -type along the bottom interface and  $p$ -type ( $\text{SrO-AlO}_2$ ) along the top interface. (grey: oxygen, dark blue: Al, light blue: La, yellow: Ti, green: Sr) Centre: (001) Layered density of states near the Fermi level of the stepped superlattice (solid lines) and pristine superlattice (dashed line). Right: The change in the layer density of free electrons on introduction of steps in the superlattice.

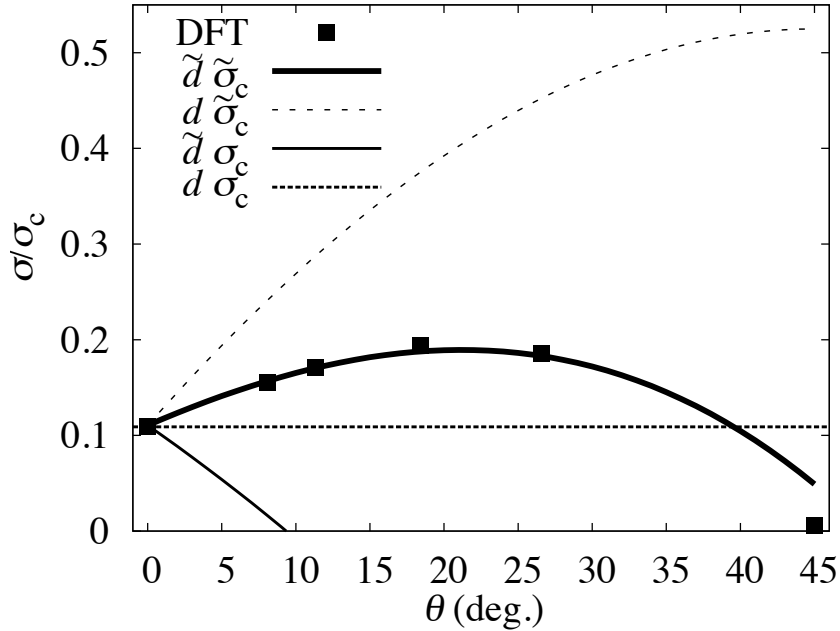


Figure 5.3: Interface free electron density,  $\sigma$ , as a function of the miscut angle,  $\theta$ , for a LAO(3 unit cells)/STO film geometry. Points represent densities calculated from DFT, and lines are electrostatic modelling under various assumptions (see text).

steps on the interface free electron density and distribution. Note that there has been no change in stoichiometry nor is there any other mechanism suggesting an additional charge transfer.

We now consider  $n$ - $p$  LAO films on STO substrates - the most commonly experimentally grown geometry. The system consists of a slab geometry of  $d$  LAO unit cells stacked on 5 unit cells of STO along the  $[001]$  direction including a 15 Å vacuum layer. A dipole correction was included in the vacuum layer to simulate open-circuit boundary conditions, preventing unphysical macroscopic electric fields due to the asymmetry of the slab and the periodic boundary conditions. The introduction of steps was the same as in the above superlattice case, and chosen such that  $n$ -type steps reside in the  $n$ -type terrace (at the interface), and  $p$ -type steps reside in the  $p$ -type terrace (at the surface). We begin with

## 5. PROPOSAL OF A ONE-DIMENSIONAL ELECTRON GAS IN THE STEPS AT THE LAALO<sub>3</sub>-SRTIO<sub>3</sub> INTERFACE

---

the case of  $d = 3$  unit cells, which we found to be beyond the pristine critical thickness within DFT for the onset of metallicity, and then alter the miscut angle,  $\theta$ , through varying  $t$  ( $s$  is again fixed at 1 unit cell to resemble that seen in experiments). The total interface free electron density,  $\sigma$ , is the STO occupied conduction band electron density calculated from the projected density of states. The results are depicted as points in figure 5.3, which shows a clear variation of free charge density with miscut angle, going through a maximum (nearly 200% of  $\sigma(\theta = 0)$ ) at intermediate angles. Three curves are compared in figure 5.3, each with various model approximations, which we discuss next.

### 5.2.3 Charge transfer model

To model  $\sigma$  as a function of  $\theta$  we use (i) Gauss' Law,  $\tilde{\sigma}_c - \sigma = \epsilon\mathcal{E}$ , where  $\epsilon$  is the LAO dielectric constant and  $\mathcal{E}$  the LAO internal electric field, and (ii) voltage drop pinning,  $\mathcal{E} = \Delta/\tilde{d}$  (140) ( $\Delta$  is the STO band gap), obtaining

$$\sigma = \tilde{\sigma}_c - \frac{\epsilon\Delta}{\tilde{d}} \quad (5.1)$$

with  $\tilde{\sigma}_c = \sigma_c(\cos\theta + \sin\theta)$  the net charge of the stepped interface as discussed earlier, and  $\tilde{d} = d(1 + C\tan\theta)/(1 + \tan\theta)$  (after some algebra), the average shortest distance between the stepped plates ( $C$  is a geometrical constant depending only on the ratio  $s/d$ ). Equation 5.1 produces the bold line curve in figure 5.3, which is in good agreement with the DFT calculations (the only parameters which are fitted are  $\epsilon$  and  $\Delta$  using the non-stepped DFT results i.e. the  $y$ -intercept of figure 5.3). Importantly, both the effect of the steps on the net polarisation,  $\tilde{\sigma}_c$ , and on the effective LAO thickness,  $\tilde{d}$ , is required to agree with the DFT calculations. Substituting simply the terrace net charge  $\sigma_c$  and/or the LAO thickness  $d$  results in disagreement with DFT (dotted and thin lines figure 5.3 respectively).

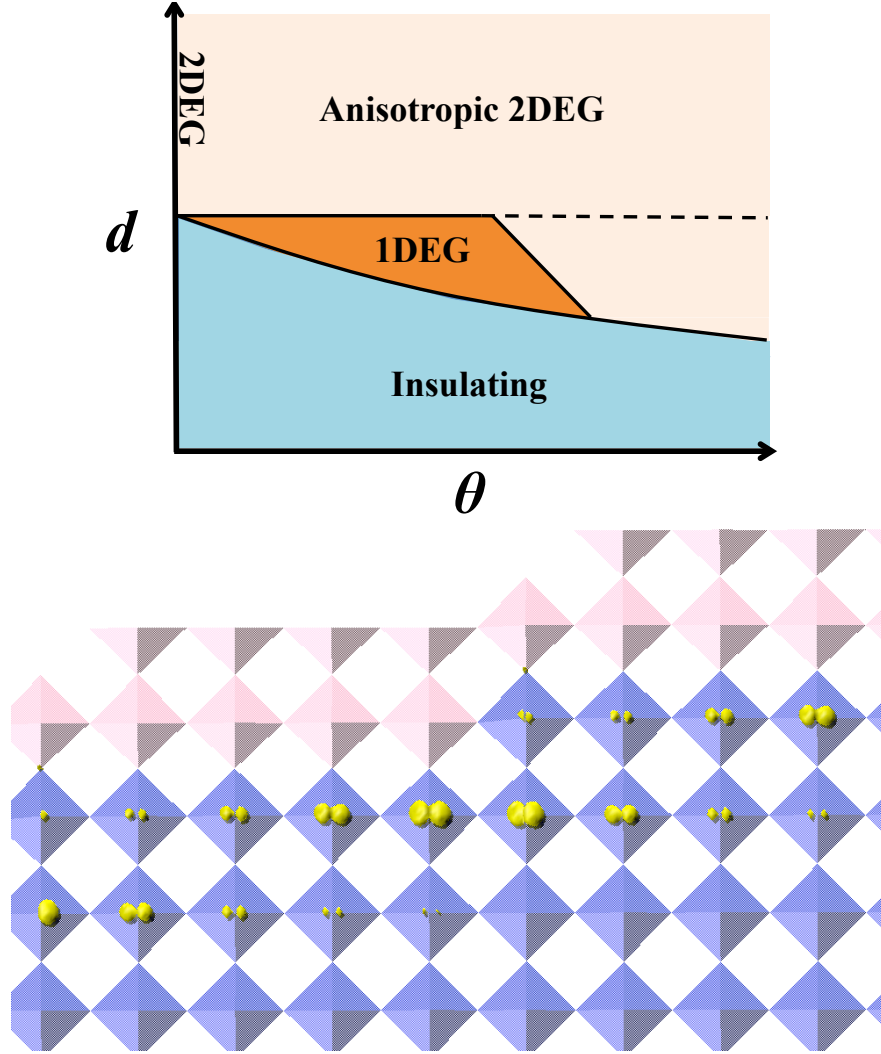


Figure 5.4: Top: Predicted schematic electronic phase diagram (see text) at the  $n$ -type (step and terrace) terminated LAO/STO interface as a function of the miscut angle,  $\theta$ , and the LAO thickness,  $d$ . Bottom: An isosurface of the Ti 3d electron density (yellow clouds) at an  $n$ -type stepped LAO/STO interface. Blue and pink cages represent oxygen octahedra around Ti and Al atoms respectively.

## 5. PROPOSAL OF A ONE-DIMENSIONAL ELECTRON GAS IN THE STEPS AT THE LAALO<sub>3</sub>-SRTIO<sub>3</sub> INTERFACE

---

### 5.2.4 Phases of the electron gas

With strong support from the DFT calculations, we explore the model further in figure 5.4 top. Firstly the critical thickness for metallicity as a function of miscut angle,  $d_c(\theta)$ . This is determined from equation 5.1 by setting  $\sigma$  to zero and rearranging for  $d$ . A schematic of this transition is shown in figure 5.4 top, for small  $\theta$ , as the curved line separating the insulating phase. The degree of curvature away from horizontal has been exaggerated for clarity. In fact, using the experimental values for  $\epsilon$  and  $\Delta$  and  $\sigma_c = 0.5e/S$ , it reaches a minimum of about 97% of  $d_c(\theta = 0)$  at  $\theta \approx 17^\circ$ . Interestingly, this minimum can be altered through epitaxial strain, since the step edge charge density relies on the out-of-plane lattice parameter, and miscut orientation. Figure 5.4 top shows three other phases above this transition curve - 2DEG, anisotropic 2DEG and 1DEG. Above the pristine critical thickness (horizontal line) an anisotropic 2DEG is predicted at any non-zero miscut angle. This is due to the non-isotropic net charge density of the interface (see later for support from DFT). Between the pristine critical thickness and  $d_c(\theta)$ , and for small  $\theta$ , a 1DEG phase is predicted, as follows. Introducing steps just below the pristine critical thickness produces carriers in the step edge, to screen the excess interface bound charge. In the limit of very small  $\theta$  these are effectively isolated steps. Considering one single step, the excess chemical charge is located around the step for the same reason that the chemical charge associated to the pristine LAO/STO (001) interface is located close to the interface. Since the free carrier charge being transferred is less than the excess chemical charge, the potential well generated by the latter confines the carriers within some width around the step in the direction normal to the step, thereby defining a 1DEG. A phase transition with increasing miscut angle occurs when the 1DEGs, with a finite width, begin to overlap with next neighbour steps. At this point, the 1DEGs are electronically indistinguishable from the anisotropic 2DEG.

In an attempt to observe the 1DEG, DFT calculations were performed on the

### 5.3 Final remarks and conclusions

---

same  $n - p$  film system (see above), now with  $d = 2$  unit cells, lower than the pristine critical thickness, and  $t=5$ ,  $s=1$ . Figure 5.4 bottom shows an isosurface of the Ti  $3d$  electron density. The electron density is clearly inhomogeneous, and accumulates near the step edge. The density decays from the step edge in to the terrace, but not to zero. The phase is the anisotropic 2DEG of figure 5.4 top, below the dotted line. By reducing the miscut angle in the simulation, it should be possible to find the 1DEG, however we are limited to not too small miscut angles due to system size. Methods including strong correlation effects, may further confine the electrons at the step.

### 5.3 Final remarks and conclusions

Experimental studies of LAO-STO investigating the effect of steps are few, but we highlight two here. Anisotropic electrical transport has been observed, but explained by anisotropic carrier mobility, not density (112). Interestingly, the strongest anisotropy was observed at lowest miscut angles, in disagreement with their step scattering model. Elsewhere, steps were found to affect the carrier mobility and density of the 2DEG (113). The carrier density was found to decrease with miscut angle, suggesting the possibility of  $p$ -type step formation.

We hope this work will stimulate the study of stepped surfaces and the search for 1DEGs. Likely candidate systems include; (i)  $n$ -type step and terrace terminations, (ii) a theoretical pristine critical thickness of only just beyond an integer number of LAO unit cells, (iii) a maximised curvature of  $d_c(\theta)$  and (iv) a small miscut angle to disconnect the 1DEGs from successive steps, but not too small since the effect of the step polarisation is then minimised. In practice this may mean; (i) surface chemical treatment to alter the step edge termination, (ii) engineering the pristine critical thickness (through for example strain (140; 168), electric field (58; 70), material (109) or atmospheric environment if the electronic reconstruction instead occurs via surface chemical redox reactions (70; 148)), and

## 5. PROPOSAL OF A ONE-DIMENSIONAL ELECTRON GAS IN THE STEPS AT THE LAALO<sub>3</sub>-SRTIO<sub>3</sub> INTERFACE

---

(*iii*) increasing the step bound charge through epitaxial strain, and miscut orientation.

In conclusion we have studied the effects of steps at the LAO-STO interface on the electronic structure. A simple model of polarisation and electrostatics is in good agreement with DFT calculations. The model predicts the existence of a 1DEG in the step edge at the interface.

# Chapter 6

## Polarisation classes of two-dimensional honeycomb compounds

### Chapter Summary

So far we have discussed the polarisation in centrosymmetric perovskite oxides in chapters 3, 4 and 5. This chapter extends these arguments to a completely different type of material with a new (three-fold rotational) symmetry, namely II-VI, III-V and IV-IV two-dimensional honeycomb structures. The formal in-plane polarisation of these materials is found to be exactly as what one would obtain if using the ideal formal charges, irrespective of covalency. This places these materials in to distinct classes of polarisation, in a similar fashion as for III-III, II-IV and I-V perovskites discussed previously. Interfaces between these classes are necessarily polar, and first principles calculations elucidate an electronic screening mechanism not dissimilar to oxide interfaces (chapter 4). The resultant interface one-dimensional (1D) electron and hole gases are in some cases half-metallic.<sup>1</sup>

---

<sup>1</sup>This chapter has been performed in collaboration with M Stengel who aided with discussions and M Pruneda who additionally generated the pseudopotentials and basis sets.

## 6. POLARISATION CLASSES OF TWO-DIMENSIONAL HONEYCOMB COMPOUNDS

---

### 6.1 Introduction

Carbon honeycomb structures have dominated nanoscience in recent years in various dimensional forms from fullerenes to nanoribbons and graphene to nanotubes. These nano-materials are expected to have significant impact in a variety of applications such as sensors, electronics, catalysis and gas storage.

Since the first real two-dimensional material (graphene) was successfully synthesised by mechanical exfoliation (173; 174), a growing number of studies have been devoted to other planar systems, which include BN monolayers (175), layered transition metal oxides (176), dichalcogenides (177; 178), or topological insulators such as  $\text{Bi}_2\text{Te}_3$  or  $\text{Bi}_2\text{Se}_3$  (179). Furthermore, improvements in growth techniques are showing signs of allowing combinations of these nanomaterials to be joined together forming heterostructures. One of the most widely studied such hybrid system is formed by the combination of graphene and BN, either as domain segregated nanosheets (180) or as stacking of layers (181), but there are many other possible geometries (e.g. Refs. (182; 183; 184)).

Another planar system includes ultrathin films of many II-VI, III-V and IV-IV compounds. Theoretical calculations predicted several years ago that the (out-of-plane) polarity of these ultrathin films could be compensated through a structural transformation to a non-polar graphitic phase with the honeycomb structure (185; 186). Several of these predicted films have since been grown in the lab (e.g. Ref. (187)). This shows that polarisation effects can be very important in these 2D systems. However, to our knowledge, in-plane polarisation and its relation to ionicity has not been formally addressed yet.

In this chapter, we explicitly address the in-plane polarisation in 2D honeycomb materials. We show, supported by first principles calculations, that (i) the role of ionicity/covalency does not affect the polarisation; (ii) the formal polarisation is found by a simple charge counting procedure (and confirmed with Berry phase and Wannier function calculations) to be equivalent to that of taking the formal ionic charges of each species, irrespective of covalency; (iii) the result is

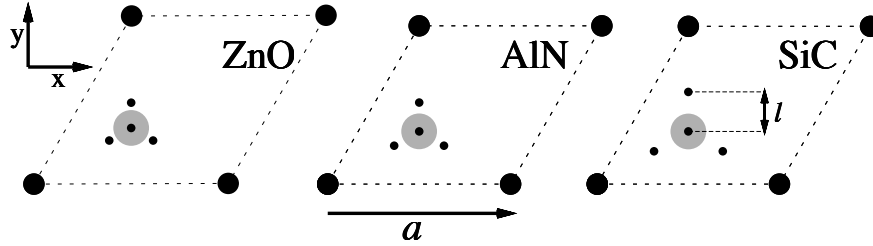


Figure 6.1: The position of the Wannier centres (small circles) in the unit cell of ZnO, AlN and SiC (to scale). The ‘cation’ (Zn, Al, Si) is represented by the large black circles, and the ‘anion’ (O, N, C) by the grey circles.  $l$  is the distance of the  $sp^2$  Wannier centres from the anion ( $l=0.431, 0.491, 0.677$  Å for ZnO, AlN and SiC respectively), and  $a$  is the cell parameter (3.316, 3.121, 3.110 Å respectively).

three distinct sets of allowed polarisation lattices, for the II-VI, III-V and IV-IV compounds; (iv) at interfaces between these classes first principles calculations elucidate an electronic screening mechanism not dissimilar to oxide interfaces, and (v) the resultant interface 1D electron and hole gasses are in some cases half-metallic.

## 6.2 Results and discussion

### 6.2.1 Polarisation classes

We begin with a discussion of 2D honeycomb materials in bulk form. The honeycomb structure can be seen as a triangular lattice with a basis of two atoms, A and B. In graphene, A and B sites are both occupied by a carbon atom, but for general graphenic structures they can be different A and B ions. Figure 6.1 shows the unit cell (to scale) of ZnO, AlN and SiC: II-VI, III-V and IV-IV compounds respectively. These three were selected from each group due to their respectively low lattice mismatch (188; 189), and the recent prediction of their stability in the 2D honeycomb structure (186), however the following considerations are general

## 6. POLARISATION CLASSES OF TWO-DIMENSIONAL HONEYCOMB COMPOUNDS

---

to any 2D insulating honeycomb compound. Figure 6.1 also displays the position of the four Wannier centres (138) of the valence per unit cell, consisting of three  $sp^2$  directional orbitals centred along bonds and one  $p_z$  orbital centred on the more electronegative of the two species (which we call the anion, and the other species with no  $p_z$  Wannier the cation)<sup>1</sup>. The distance of the  $sp^2$  Wannier centre to the anion,  $l$ , increases from the II-VI to the III-V to the IV-IV compounds, as one might expect due to the increasing covalent nature of the species. Due to the three-fold symmetry of these structures, the *effective* polarisation is zero irrespective of ionicity-covalency, as traditionally defined. However the *formal* polarisation is not necessarily zero, as has been discussed in the topical context of oxides and  $\text{LaAlO}_3$  (28; 29; 141) (see chapter 3). Taking the formal polarisation,  $P$ , as defined within the modern theory of polarisation (135) by the position of the Wannier and core centres (136), we calculate  $P = 4/3, 6/3$ , and  $8/3$  ( $e/a$ ) modulo a quantum of polarisation ( $2/\sqrt{3} e/a$ ) for the II-VI, III-V and IV-IV compounds respectively (defined as the dipole moment per unit area in 2D). These values were also confirmed with Berry phase calculations (135) within the SIESTA code (114; 115). These values are equivalent to taking point charges of the formal charge of each species. In other words, the degree of ionicity-covalency does not affect the polarisation.

The lattice of allowed polarisation vectors,  $\mathbf{P}$ , is displayed in figure 6.2. Each class of material (II-VI, III-V or IV-IV) has a triangular lattice of polarisation vectors as expected from the threefold rotational symmetry, with each set displaced by  $2/3$  ( $e/a$ ) from the others. The three sets of polarisation values here bear connection within the topical field of polarity in oxide heterostructures and the 2DEG at the interface between  $\text{LaAlO}_3$  and  $\text{SrTiO}_3$  (35).  $\text{LaAlO}_3$ ,  $\text{SrTiO}_3$  (and for example  $\text{KNbO}_3$ ), so-called III-III II-IV (and I-V) perovskites, have different sets of allowed polarisation values defining different classes of material by

---

<sup>1</sup>The Wannier calculation was performed with the Wannier90 (190) code and the density functional theory (DFT) code SIESTA (114; 115).

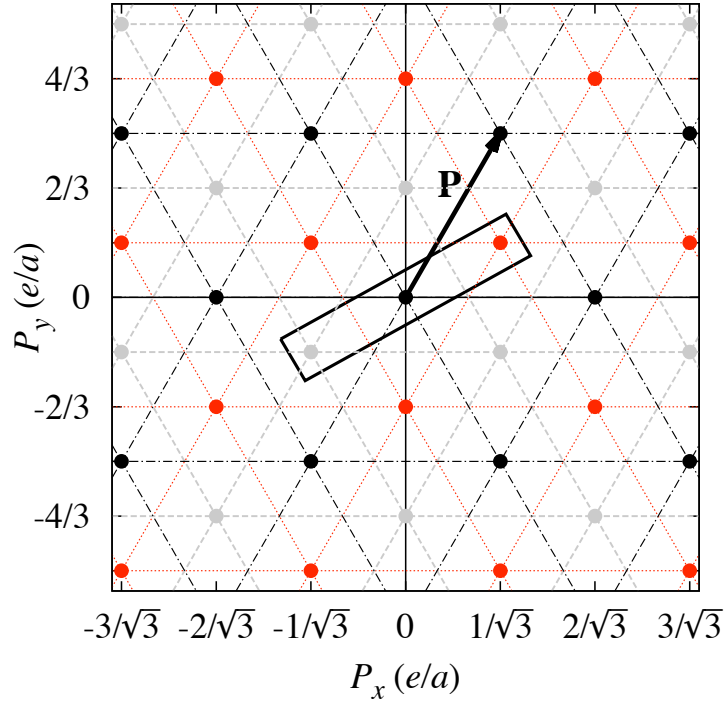


Figure 6.2: The triangular lattice of allowed polarisation values for the II-VI (red), III-V (black) and IV-IV (grey) 2D honeycomb compounds. The dots represent polarisation vectors, indicated by  $\mathbf{P}$ . The box highlights an example of a compatible set of values (see text).

polarisation (see chapter 3), in relation to the 2D honeycomb materials here. The different symmetry (three-fold in the honeycomb structure versus inversion in the oxide perovskites) give rise to a new set of formal values. One might expect that interfaces between two 2D honeycomb materials from different polarisation classes might also show unusual electronic behaviour.

### 6.2.2 Superlattices

To test this prediction, first principles calculations were performed of interfaces between the II-VI, III-V and IV-IV compounds. The interface direction was chosen to be along  $x$  (defining the zig-zag edge). Stoichiometric zig-zag nanorib-

## 6. POLARISATION CLASSES OF TWO-DIMENSIONAL HONEYCOMB COMPOUNDS

---

bons (ZNRs) of each material were joined to maintain the  $A_aB_aA_bB_b$  stacking sequence ( $A_a$ : cation of material  $a$ ,  $B_b$ : anion of material  $b$  etc.), since the ABBA sequence was found to be metallic for all thicknesses without a band gap, likely due to the incompatibility of the  $sp^2$  bonding between the A-A and B-B interface species. The resultant superlattice contains two different interfaces ( $A_aB_aA_bB_b$ , and  $A_bB_bA_aB_a$ ). The ZNRs were made of various thicknesses,  $n$ , being the number of AB bi-layers. The first principles calculations were performed using the spin-polarised Perdew-Burke-Ernzerhof (PBE) exchange correlation functional (191) as implemented in the SIESTA code (114; 115). Norm conserving pseudopotentials (127) and double- $\zeta$  polarised bases were used for the valence electrons (152). Atomic forces were relaxed to less than 20 meV/Å. A 20 Å vacuum layer between the 2D sheets was included, which was found to be a sufficient separation (tests of up to a 200 Å vacuum layer did not affect results significantly).

At this point we note a side issue related to polarisation in the superlattice systems. Mismatch strain, albeit small for the materials chosen, may introduce a non-trivial electronic component to the polarisation on top of the polarisation discussed in section 6.2.1. This arises due to the loss of the threefold symmetry axis with axial strain. The systems are then likely to be piezoelectric. These effects are beyond the current study, but would be an interesting line of research for future work. We believe the effects to be small compared with the large lattice polarisation discussed above, especially for the 0.3% mismatched SiC-AlN system.

Figure 6.3 shows the line density of a one-dimensional electron (hole) gas (1DEG) appearing at the interface between AlN-SiC (III-V - IV-IV) and ZnO-SiC (II-VI - IV-IV) as a function of layer thickness,  $n$ . The 1DEGs appear to screen the net charge at the interface (see discussions below and figures 6.4 and 6.5 for details of this electronic screening). With increasing layer thickness, the 1DEG density tends to this net charge which equals, from the interface theorem (30), the difference in the component of the bulk polarisation perpendicular to the

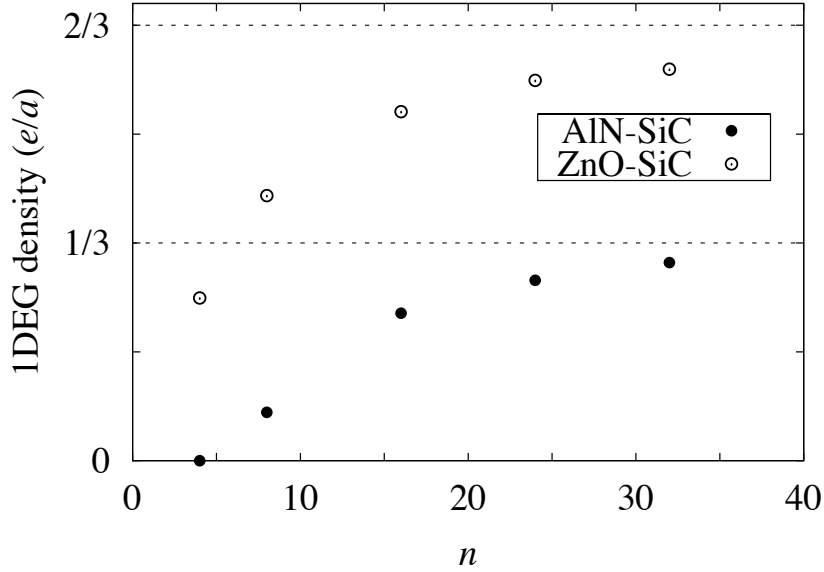


Figure 6.3: The density of free electrons (or holes) calculated as a function of slab width ( $n$ ) for the two superlattice systems.

interface from material  $a$  to material  $b$ . This is in agreement with what is found in the full first principles calculations (compare figure 6.3 dotted lines, with figure 6.2). It is interesting to note that the pair of polarisation values from both sets does matter (similar to the arguments presented for oxides, see chapter 3). Figure 6.2 highlights a compatible group of polarisation values in the rectangular box region. This group is compatible since the respective choice in unit cell of each material includes all charge within the interfacial unit cell as polarisation (bound charge). Varying the choice of unit cell from material  $a$  to material  $b$  (i.e. the polarisation value) amounts to leaving free charge at the interface unaccounted for by the polarisation. The result is equivalent, only our description of the charge changes (bound versus free charge, see chapter 3). See Ref. (141) and references within for more details.

We now explore the details of the electronic screening in the superlattices. Figures 6.4 and 6.5 show the electronic structure in real and reciprocal space respectively. Figure 6.4 is the spin-resolved layer-by-layer density of states (DOS)

## 6. POLARISATION CLASSES OF TWO-DIMENSIONAL HONEYCOMB COMPOUNDS

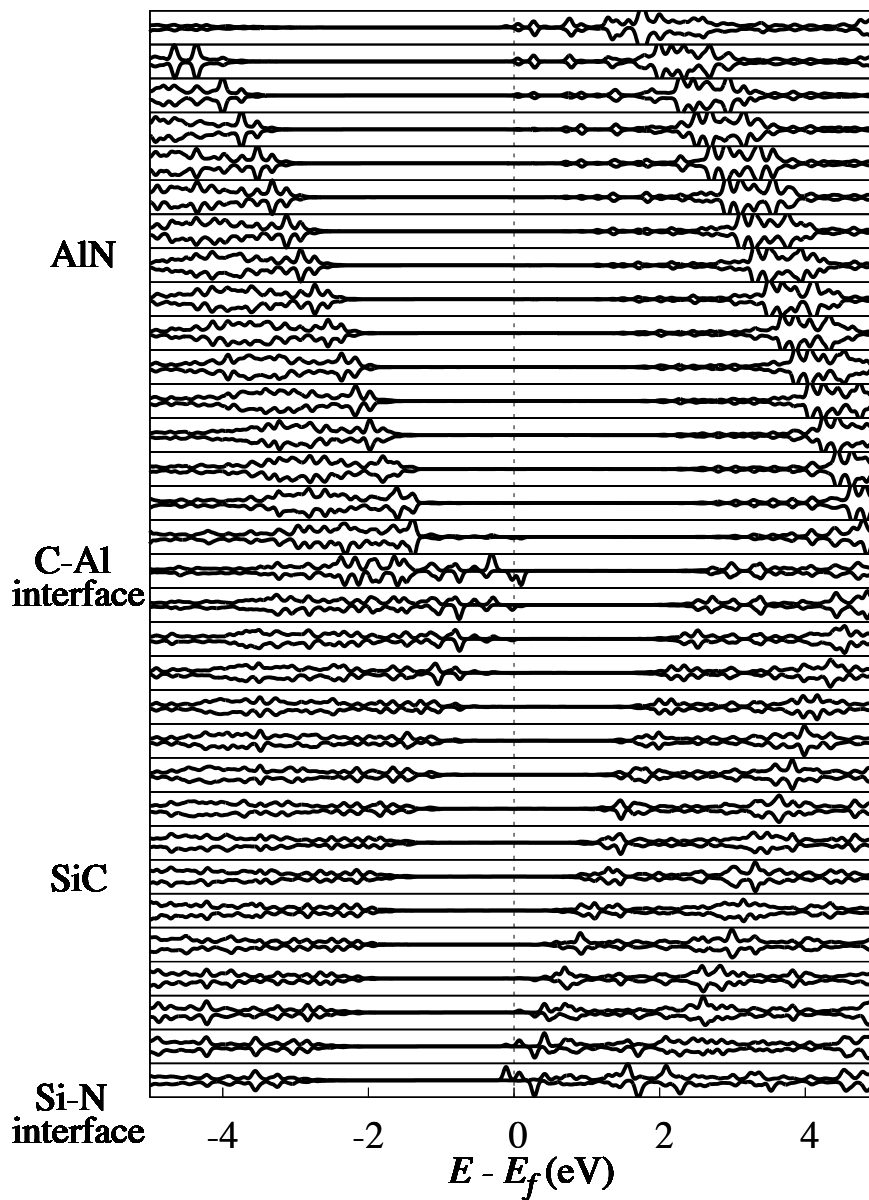


Figure 6.4: The layer-by-layer density of states (DOS) of the AlN-SiC ( $n=16$ ) superlattice. Top panels are the DOS of spin up electrons, and bottom panels are the DOS of spin down electrons. The top half is the AlN slab, and the bottom half the SiC slab and the interface terminations are indicated.

of the AlN-SiC ( $n=16$ ) superlattice. The bands are seen to shift in energy within each layer in a zig-zag fashion, with the potential drop pinned to the effective band gap (in this case the band gap of SiC), once the layers are thick enough (for  $n=4$ , not shown, the drop is smaller than the gap and the system is insulating). These shifts are due to an electric field arising from the net interfacial charge. Notice that the electronic screening mechanism resembles that seen in oxide superlattices (140) (see chapter 4), although the electrostatics of this system is different, with nonuniform fields in the sheet's plane and stray fields in the vacuum space. The pinning of the drop occurs because of an electronic transfer from the top of the valence band at the negatively charged interface ( $p$ -type) to the bottom of the conduction band at the positively charged interface ( $n$ -type), creating the 1D electron and hole gasses. As the layer thickness increases the internal electric field reduces (since the drop is pinned), and the 1DEG density tends to the interface bound charge in agreement with figure 6.3.

Figure 6.5 displays the spin-resolved band structure near  $E_f$  for the same superlattice. Two bands are seen to cross  $E_f$ , and correspond to two localised states at the Si-N and Al-C interfaces that can be coupled ferromagnetically (FM) or antiferromagnetically (AF) (192). For sufficiently wide SiC and AlN stripes, both states are decoupled and the AF and FM solutions are degenerate in energy. In the AF (FM) configuration, electrons are transferred from the Al-C  $\pi$  bonding state to the Si-N  $\pi^*$  antibonding state giving rise to half-metallic 1D electron and hole gases of the same (opposite) spin at each interface. In this case the amount of charge transferred can be obtained from the k-point where the bands cross  $E_f$ : for large  $n$  they should cross at the k-point  $2/3$  from  $\Gamma$  to X corresponding to a charge of  $1/3$ , if  $n$  is small, the bands cross closer to X or simply do not cross. Bands corresponding to the opposite spin for the Al-C (Si-N) interfacial states are slightly below (above) these. The set of unoccupied parabolic bands at  $\Gamma$  seen in Fig.3 are also localised at the Si-N edge, and their range of localisation decreases with increasing energy (although not shown, there are also similar occupied bands

## 6. POLARISATION CLASSES OF TWO-DIMENSIONAL HONEYCOMB COMPOUNDS

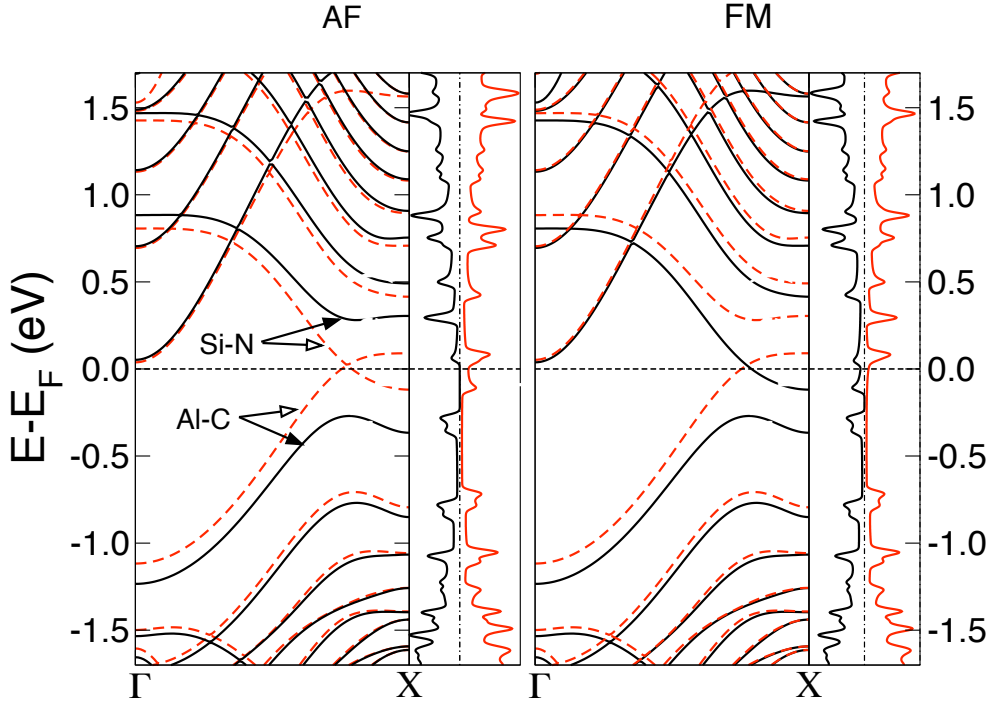


Figure 6.5: The band structure and total DOS of the AlN-SiC ( $n=16$ ) superlattice in AF and FM spin configurations. Black lines are spin up bands, and red dashed lines spin down bands.

at lower energies localised at the Al-C interface). These bands are partially occupied for ZnO-SiC superlattices giving the extra charge-transfer contribution needed. Since these bands are spin degenerate, the ZnO-SiC system is not half-metallic with a reduced spin polarisation. Otherwise the band structure for ZnO-SiC is similar. The origin of the magnetism in systems of charge injection in to different bulk, nanoribboned and heterostructured honeycomb structures have been discussed elsewhere (192; 193; 194; 195; 196; 197; 198).

### 6.3 Final remarks and conclusions

We briefly mention some final remarks. The polar structures studied here may, in certain growth conditions, find more energetically favourable screening

### 6.3 Final remarks and conclusions

---

mechanisms as an alternative to electronic screening. As an example an anionic vacancy can donate electrons to the  $n$ -type interface, or combinations of anionic vacancies and cationic vacancies at each interface can provide the necessary charge screening without free electrons. Similar mechanisms have been proposed at the  $\text{LaAlO}_3$ - $\text{SrTiO}_3$  interface, and its energetics discussed (148) (see next chapter, 7). If the growth conditions can be controlled such that these point defects are minimised it may be possible to utilise the systems here for various applications such as spintronics, sensors and electronics. It would also be interesting to study the excitonic properties of the electron-hole gases, and in addition the possible piezoelectric and piezoresistance effects.

In conclusion we have introduced classes of 2D honeycomb materials in terms of polarisation. Interfaces between these classes can exhibit interesting properties such as half-metallic 1DEGs. The physics describing these superlattices is not dissimilar to oxide systems (see chapters 3, 4 and 5).

## 6. POLARISATION CLASSES OF TWO-DIMENSIONAL HONEYCOMB COMPOUNDS

---

# Chapter 7

## Surface defects and conduction in polar oxide heterostructures

### Chapter Summary

The past few chapters (chapters 4, 5 and 6) have considered the physics of pristine interfaces between polar materials, and the pure electronic screening that results. In this chapter we present an alternative origin to the 2DEG at the LAO-STO interface as surface redox reactions, in particular surface O vacancies, using a model supported by first principles calculations that describes the redox formation. In agreement with recent spectroscopic and transport measurements, we predict a stabilisation of such redox processes (and hence Ti *3d* occupation) with film thickness beyond a critical value, which can be smaller than the critical thickness for 2D electronic conduction, since the surface defects generate trapping potentials that will affect the interface electron mobility. Several other recent experimental results, such as lack of core level broadening and shifts, find natural explanation. Pristine systems will likely require changed growth conditions or modified materials with a higher vacancy free energy. <sup>1</sup>

---

<sup>1</sup>The results presented in this chapter have been published in the article of Bristowe, Littlewood and Artacho Phys. Rev. B **83**, 205405 (2011) (148).

## 7. SURFACE DEFECTS AND CONDUCTION IN POLAR OXIDE HETEROSTRUCTURES

---

### 7.1 Introduction

Complex oxides offer the potential to replace conventional semiconductors in a range of devices due to reduced feature sizes and added functionality (see e.g. ref. (48; 199)). The polar interface between  $\text{LaAlO}_3$  (LAO) and  $\text{SrTiO}_3$  (STO) (35) has shown promise as a field effect transistor (58; 70). One problem hindering its development is the low mobility of the interface two-dimensional electron gas (2DEG). To progress, the origin of the 2DEG must be understood. Explanations proposed to date can be classed into three categories: (i) electron transfer countering the “polar catastrophe” (36), (ii) doping through O vacancies in the film (70; 200; 201; 202) or in the substrate (52; 53; 54), and (iii) cation intermixing at the interface (36; 102; 103; 105). Growth conditions have been shown to affect the observed behaviour, particularly  $\text{O}_2$  partial pressure and post-annealing treatments, affecting carrier density and confinement to the interface (as opposed to conduction through the STO substrate) (53; 58).

The polar catastrophe (36) arises from a polarisation discontinuity between the non-polar STO substrate and polar LAO film (141) as discussed in chapters 3, 4 and 5. In LAO films grown on  $\text{TiO}_2$  terminated STO substrates this polar discontinuity induces a divergence of the electric displacement field ( $\nabla \cdot \mathbf{D}$ ) in the pristine system equal to considering the effective polarisation response and net effective charges  $\sigma_c$  of precisely  $+e/2$  and  $-e/2$  per formula unit at the interface and surface, respectively (28; 140; 141). The electrostatic potential then builds up across the LAO film, accumulating electrostatic energy. To counter it a charge transfer between the interface and the surface is required. A mechanism intrinsic to the pristine system is given by the transfer of electrons from the surface to the interface. From band bending arguments, electrons are transferred from the O  $2p$  at the top of the valence band at the LAO surface, to the Ti  $3d$  conduction band at the interface, once the potential drop across the LAO layer reaches the effective band gap, which is calculated to happen for a LAO thickness of five unit cells (see ref. (50) and within). However the absence of a 2D hole gas

at the surface and the observation of populated Ti  $3d$  states for films as thin as one or two bilayers (59; 60; 64) raises doubts about this mechanism. Two important points should be kept in mind. Firstly, the samples are generally not kept or measured in vacuum. The surface can thus be covered by adsorbents like water, and it will likely be far from an ideal surface termination, possibly including chemical alterations such as the hydroxylation seen on many wet oxides. The second point is more central, however: whatever the chemistry, the relevant electrostatics across the film can only be affected by processes in which charge is altered at each side of the film, either by charge transport across it, or by charges arriving at either side from external reservoirs. If there are no such external sources and the chemical processes are confined to the surface, the remaining possibility is that of surface redox processes. They transform surface bound charge into free-carrier charge, the electrons or holes then being free to move to the buried interface. The clearest and quite relevant example is that of oxygen vacancy formation whereby surface  $O^{2-}$  anions transform into  $O_2$  molecules, releasing two electrons to the  $n$  interface, as illustrated in figure 7.1 (70; 200; 201; 202). Surface protonation (203; 204) is an analogous process in which the surface is also reduced by the oxidation of  $O^{2-}$  into  $O_2$ , although in this case the process depends on the presence of water,  $H_2O \rightarrow 1/2 O_2 + 2e^- + 2H^+$ , and both the energetics and kinetics will be different from the previous one (203). The protons attach to the surface O atoms, while the electrons are again free to go to the  $n$  interface (note that the non-redox hydroxylation,  $H_2O \rightarrow OH^- + H^+$ , does not affect the electrostatics across the film).

In section 7.2 we present a model for the formation of surface redox processes. We then apply the model to the LAO/STO system in section 7.3 using parameters obtained from first-principles calculations (see section 7.5). We show that, for such a surface redox process, (*i*) the process is favoured by film thickness through the effect of the electric field across the film; (*ii*) the growth of the density of the related surface defects with film thickness is predicted, showing a

## 7. SURFACE DEFECTS AND CONDUCTION IN POLAR OXIDE HETEROSTRUCTURES

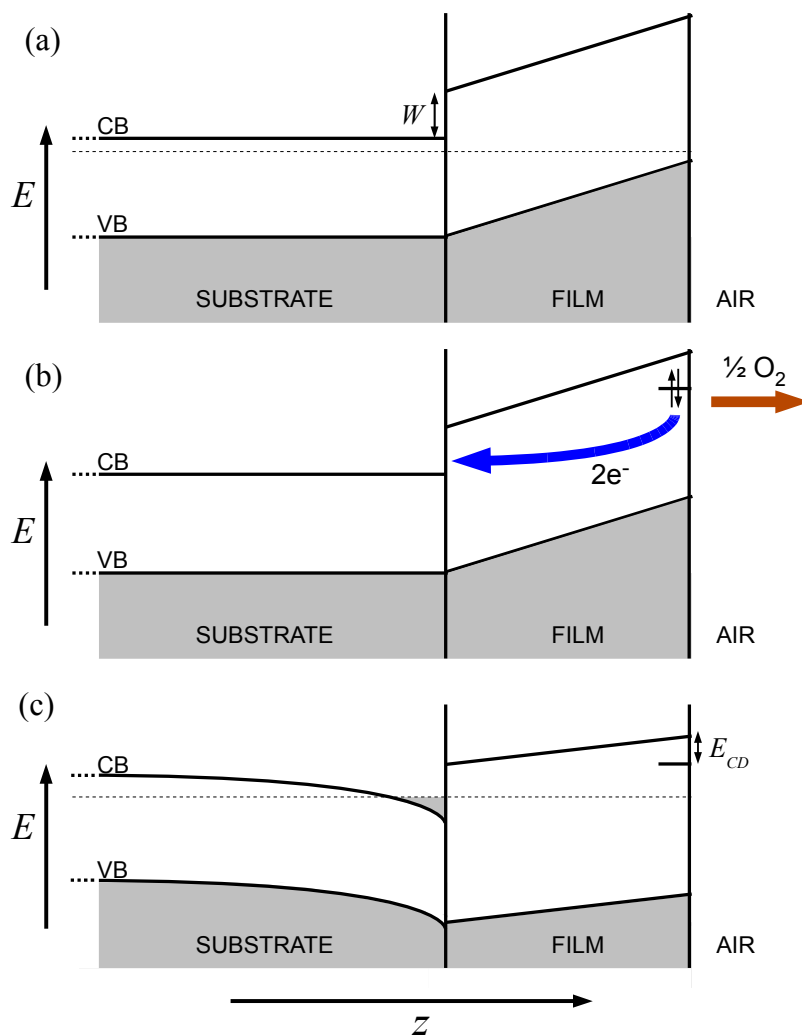


Figure 7.1: Schematic band diagram of an interface between a polar film and a non-polar substrate along the normal direction,  $z$ . (a) The pristine system under the critical film thickness. (b) The creation of a donor state at the surface via a redox reaction and subsequent electron transfer. (c) The process reduces the film's electric field.  $W$  is the conduction band offset and  $E_{CD}$  is the energy difference between the surface conduction band minimum and the donor state level.

minimum critical thickness; *(iii)* the model is in excellent agreement with first principles calculations and reasonable agreement with what is observed experimentally for Ti 3*d* occupation; *(iv)* the potential drop across the film does not change substantially with thickness once vacancies start to appear; *(v)* for thin films the carriers at the interface are still trapped by the electrostatic potential generated by the vacancies in deep double-donor states: a strongly disordered two-dimensional electron system; *(vi)* as thickness increases the levels become shallower and the number density increases, closing the gap to the conduction band; *(vii)* the conduction onset is therefore at a higher film thickness than the one for interfacial carrier population. Finally we note that the model can also be applied to *p*-type interfaces and ultra thin ferroelectric films, where alteration of the surface chemistry has also been proposed as a possible screening mechanism (see for example ref. (32) and chapter 8).

## 7.2 Model

We consider a pristine polar thin film on a non-polar substrate defining a *n*-type interface (see figure 7.1), and a surface reduction process (the model can be trivially extended to *p*-type interfaces and surface oxidising reactions, see below). The introduction of a surface defect via a redox reaction produces a donor level in the gap. The defect provides *Z* electrons (two for an O vacancy) that can transfer to the interface (see figure 7.1), thus contributing to the screening of the polarisation or compositional charge  $\sigma_c$  at either side of the polar film ( $\pm 0.5e/\text{f.u.}$  in LAO (28; 140; 141)).

Considering this electron migration, we can model the formation energy of one such surface defect,  $E_{\text{form}}$ , in the presence of an area density *n* of surface defects as

$$E_{\text{form}}(n) = C + E_{\mathcal{E}}(n) + \alpha n, \quad (7.1)$$

where we have separated an electrostatic term associated with the internal electric

## 7. SURFACE DEFECTS AND CONDUCTION IN POLAR OXIDE HETEROSTRUCTURES

---

field in the film,  $E_{\mathcal{E}}(n)$ , from a surface/interface chemistry term,  $C$ , and a term accounting for defect-defect interactions other than electrostatic in a mean-field sense. It can be seen as arising from

$$E_{\text{form}}(n) = E_{\text{form}}^0 - Z(W - E_{CD}) + E_{\mathcal{E}}(n) + \sum_i^{\text{others}} J_i r_i, \quad (7.2)$$

where  $E_{\text{form}}^0$  is the formation energy of an isolated surface defect in the absence of a field across the film,  $W$  and  $E_{CD}$  are defined in figure 7.1<sup>1</sup> and  $J_i$  and  $r_i$  are the defect-defect coupling interaction and separation respectively.  $E_{\text{form}}^0$  (and thus  $C$ ) depends on the particular surface chemical process, and the reference chemical potential for the relevant redox counterpart species in the environment, e.g.  $\mu_{\text{O}_2}(p, T)$ , which depends on experimental conditions (partial pressure,  $p$ , and temperature,  $T$ ).

Taking equation 7.1, the surface excess energy for a given area density of surface defects is then

$$\Omega(n) = \int_0^n E_{\text{form}}(n') dn' = Cn + \Omega_{\mathcal{E}}(n) + \frac{1}{2}\alpha n^2. \quad (7.3)$$

The key of the proposed energy decomposition is that the  $\Omega_{\mathcal{E}}$  term is simply the energy gain per unit area of partly discharging a capacitor, which is

$$\Omega_{\mathcal{E}}(n) = \frac{d}{2\epsilon} [(\sigma_c - \sigma_v)^2 - \sigma_c^2], \quad (7.4)$$

where  $d$  is the film thickness,  $\epsilon$  is the LAO dielectric constant,  $\sigma_c$  is the compositional charge, and  $\sigma_v = n(Ze)$  is the charge density of the carriers confined to the interface (note that these electrons may not all be mobile, as discussed below). Equation 7.4 assumes no screening by electronic reconstruction, which is right if the onset for defect stabilisation happens earlier than the one for electronic reconstruction (and the surface defect mutual repulsion is weak), both of which we believe to be true for the case of LAO-STO (see next section). We limit ourselves to the regime given by equation 7.4 since a wider discussion of the model is

---

<sup>1</sup>A valence band offset has been omitted for clarity since it is known to be small, but can also be included alongside the conduction band offset without affecting the model

irrelevant here. A complete description of all possible regimes will be presented elsewhere (205).

The equilibrium defect density is determined by finding the value that minimises  $\Omega$ . Taking equations 7.3 and 7.4,

$$n = \frac{dZe\sigma_c - C\epsilon}{(Ze)^2d + \alpha\epsilon}. \quad (7.5)$$

A critical thickness arises for defect stabilisation,

$$d_c = C\epsilon/(Ze\sigma_c), \quad (7.6)$$

$n$  tending to  $\sigma_c/Ze$  for large  $d$ , which is the value required to completely screen the film's intrinsic polarisation.

## 7.3 Discussion

### 7.3.1 Interface carrier density

We now consider the specific case of O vacancy formation at the surface as the most prominent candidate redox process (70; 200; 202). Figure 7.2a) shows quantitative agreement between the model's  $\bar{E}_{\text{form}} = \frac{1}{n}\Omega(n) = \frac{1}{n}\int_0^n E_{\text{form}}dn'$  and first principles calculations of the surface vacancy formation energies in ref. (200) on the full LAO/STO structure.  $\bar{E}_{\text{form}}$  is the right magnitude to compare to first-principles results since it accounts for the energy difference between the system with a given concentration of surface defects ( $n$ ) and the pristine system ( $n = 0$ ), per surface defect, thus  $\Omega(n)/n$ . The physical constants used in the model were determined independently by separate DFT calculations (see section 7.5) and then compared to DFT results for films of varying thickness (figure 7.2a)). The predicted behaviour of  $n$  (and  $\sigma_v$ ) in LAO/STO is shown in figure 7.2b), where it is compared with Ti  $3d$  occupation (both trapped and mobile) as measured with HAXPES (59). Two bands are plotted, the coloured one uses a range in  $C$ , the striped one a range in  $\alpha$  and  $\epsilon$  (see section 7.5). The bulk dielectric constant of

## 7. SURFACE DEFECTS AND CONDUCTION IN POLAR OXIDE HETEROSTRUCTURES

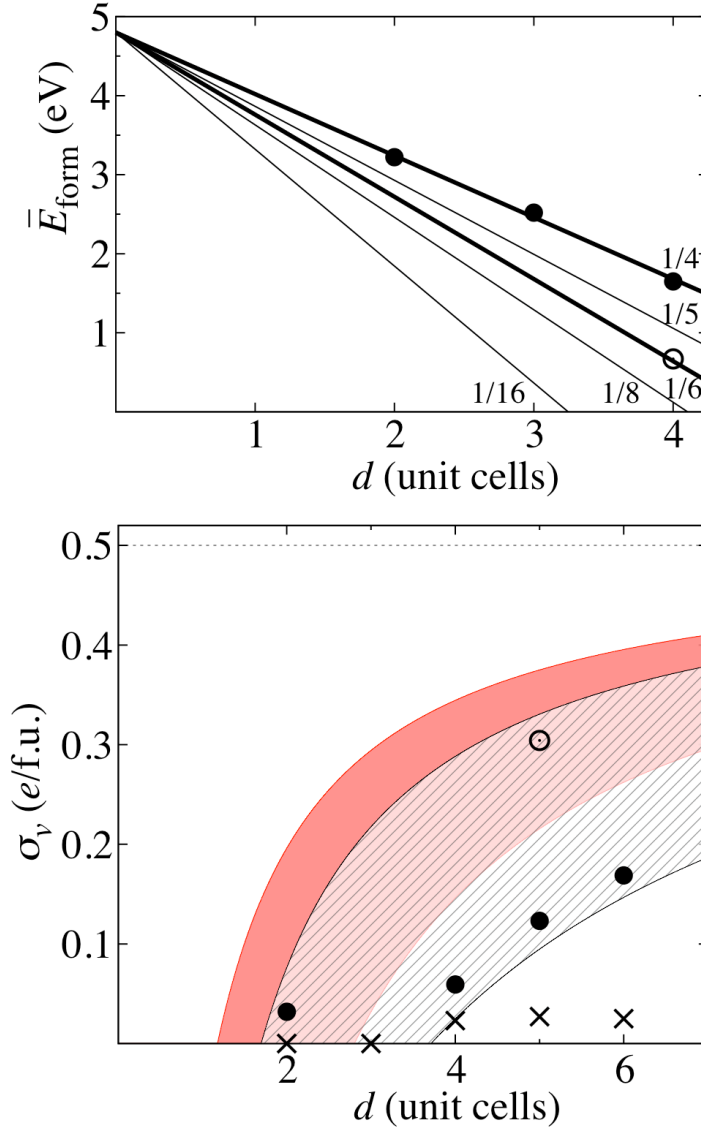


Figure 7.2: a) Defect formation energy,  $\bar{E}_{\text{form}}$  (see definition in text) versus LAO film thickness  $d$  for various vacancy densities  $n$ . The model (lines) is compared with the DFT calculations (circles) of ref. (200) of the surface vacancy formation energy on the full LAO/STO structure (see section 7.5 for the determination of the model parameters). b) Equilibrium area density of interface carriers  $\sigma_v$  versus  $d$ . The red (grey) band is the model prediction for  $2.1 \text{ eV} < C < 5.0 \text{ eV}$ ,  $\epsilon = 25$  and  $\alpha = 0.8 \text{ eV}/(\text{vac}/\text{f.u.})^2$ . The striped band is for  $C = 3.6 \text{ eV}$ ,  $21 < \epsilon < 46$  and  $0 < \alpha < 8 \text{ eV}/(\text{vac}/\text{f.u.})^2$ . The circles indicate the Ti  $3d$  occupation as measured with HAXPES in ref. (59). Open circle indicates the sample was not annealed. The crosses indicate the carrier density from Hall measurements in ref. (58).

LAO is about 24 (206). It may be substantially different for a strained ultra-thin film (see ref. (50) and within) and so the range  $21 < \epsilon < 46$  has been considered.

The agreement in figure 7.2b) between model and experiment is only qualitative given the ambiguities in some of the magnitudes of key parameters defining the problem, most notably the chemical potential of O<sub>2</sub> in experimental conditions. Despite this, the model predicts a critical thickness for the appearance of carriers at the interface for a LAO film thickness below the five unit cells predicted by the purely electronic mechanism. Other qualitative features observed but not understood in this system also find a natural explanation (below).

### 7.3.2 Electric field in LAO: pinning of potential drop

The electrostatic potential drop across the LAO film is

$$V = (\sigma_c - \sigma_v)d/\epsilon. \quad (7.7)$$

Substituting  $\sigma_v$ , the drop is essentially independent of thickness,  $V \approx C/(Ze)$ , when the vacancy-vacancy interaction is small,  $\alpha \ll (Ze)^2d/\epsilon$ . Using the parameters for LAO/STO the difference in potential drop per LAO layer added is between 0.0 and 0.2 eV/f.u., much smaller than the predicted thickness dependence for the electronic screening model, and consistent with recent XPS measurements, which show no core level broadening with film thickness (61). The pinning of  $V$  is also consistent with reduced cation-anion relative displacement with increasing LAO thickness as measured by SXRD (68).

### 7.3.3 Onset of conduction: electron trapping

The redox processes proposed above explain the absence of hole-mediated transport at the surface, while electrons allow 2D conduction at the interface. An important observation that remains unexplained, however, is the fact that the onset of interfacial Ti 3*d* occupation, as measured with HAXPES (59; 60; 64), happens at lower film thickness than the onset for interfacial 2D conduction (58).

## 7. SURFACE DEFECTS AND CONDUCTION IN POLAR OXIDE HETEROSTRUCTURES

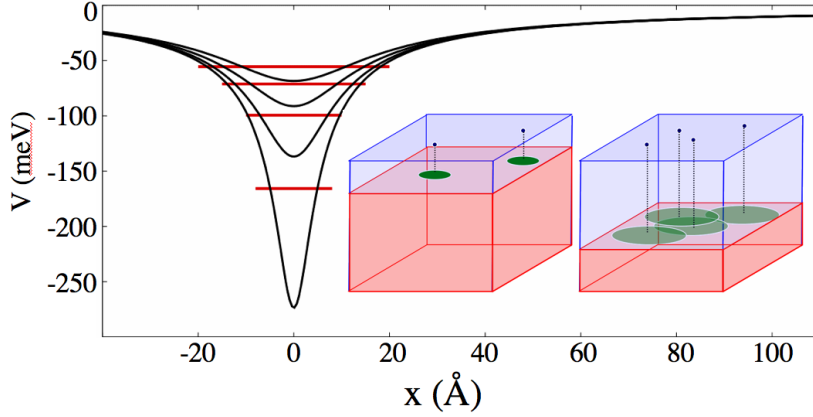


Figure 7.3: Trapping potential  $V$  created by a surface O vacancy as seen by interface electrons versus distance within the interface plane  $x$  ( $x=0$  is directly below the vacancy) for film thickness  $d = a$  (deepest),  $2a$ ,  $3a$ ,  $4a$  (shallowest), with harmonic estimates of corresponding donor ground states (taking  $m_{\text{eff}} = 3m_e$  (81)). Inset: Sketch of range and density of trapped states.

It has been suggested that the 2DEG lies in several Ti  $3d$  sub-bands, some of which are not mobile due to Anderson localisation (94). Whether Anderson localisation occurs on an energy scale as high as room temperature depends on the energy scale of the disorder distribution. The surface defects associated to the redox processes represent point sources of effective charge, very much as a dopant in a semiconductor (28), e.g.  $+2e$  for an O vacancy. They then generate trapping potentials for the carriers at the interface plane of the form  $V_{\text{trap}} = Ze^2/\epsilon\sqrt{r^2 + d^2}$ , in atomic units, where  $d$  is the film thickness and  $r^2 = x^2 + y^2$  corresponds to the radial variable in the plane. This potential is sketched in figure 7.3 for several  $d$  values. Its depth decays with thickness as  $1/d$ . Figure 7.3 shows estimates of the ground state electron level associated to the double donor state arising at the interface due to an O vacancy at the surface. These trapped interface levels may be the ‘in-gap states’ seen in a recent spectroscopic study (65). For a thin film the traps are deep and few, but as it grows thicker, the donor states become shallower *and* the area density of traps grows, as illustrated in the inset of figure 7.3. A

## 7.4 Final remarks and conclusions

---

transition from insulating to conducting behaviour is thus expected at a larger film thickness than the critical thickness for surface defect stabilisation. With growing thickness, not only dopant levels tend to overlap as in a degenerate semiconductor, but the doping-level band is pushed towards the conduction band. For  $Z = 2$ , as for O vacancies, the physics of this transition is that of band overlap and disorder, since all dopant states are doubly occupied. If the mechanism involves  $Z = 1$  defects, as in the hydroxylation case, the transition will be rather Mott-Anderson, as each dopant state is singly occupied. The different phenomenologies could be used to ascertain on the mechanism. The surface potential distribution from charged defects is consistent with a recent Kelvin probe force microscopy study (207).

## 7.4 Final remarks and conclusions

A recent AFM study of LAO/STO has proposed the mechanism for conductivity switching (58; 70) as the writing of surface charge (75). Applying a biased tip to the surface alters the field across the LAO film which either increases or decreases the stability of vacancies (and hence  $\sigma_v$ ) depending on the sign of the bias. An implication of this observation is that the kinetics for these redox processes is accessible at room temperature as used in these experiments, not only the much higher temperature used for growth.

The model proposed can also be used for  $p$  interfaces, holes, acceptor levels and surface oxidation processes. This would be the case for LAO grown on SrO terminated STO. It is less symmetric than it seems, however, since, in addition to different energetics and chemical potentials, the large conduction band offset at the interface ( $W$  in figure 7.1) favours the situation for electrons towards  $n$  interfaces much more than the much smaller valence band offset for holes and  $p$ -interfaces. For thin film ferroelectrics with outwards (inwards) polarisation on metallic substrates, the important alignment becomes the acceptor (donor) level

## 7. SURFACE DEFECTS AND CONDUCTION IN POLAR OXIDE HETEROSTRUCTURES

---

with the metal fermi level. This could be behind the stability of switchable ultra thin ferroelectric films under open circuit conditions (see e.g. ref. (5; 32)). See chapter 8 for further discussion.

In conclusion, surface redox processes by have been shown to be promoted by the the internal electric field in polar thin films. A simple model has been used to predict the film-thickness dependence of the equilibrium density of surface defect levels, and corresponding interface carrier density. The model is applied quantitatively to the formation of O vacancies at the surface of a LAO film on STO. The estimated carrier density and potential drop as a function of LAO thickness is compared with recent HAXPES and XPS core level measurements respectively. Carrier trapping for thin films is discussed, with different physics predicted for single and double donor defects as would arise from vacancy formation or hydroxylation.

### 7.5 Model parameters

Here we describe the determination of the parameters,  $\alpha$ ,  $\epsilon$  and  $C$  used in the model in figure 7.2 of section 7.3. The parameters used in the model were independently determined from first principles in appropriate LAO-based systems (see below), and then the model was checked against DFT calculations of vacancy formation energies in the full LAO/STO system as a function of thickness (figure 7.2a)). When comparing the model with experiment (figure 7.2b)), we account for inaccuracies of DFT and the ambiguity of the experimental chemical potential in the determination of each of these parameters.

#### 7.5.1 The vacancy-vacancy interaction term, $\alpha$

The defect-defect term was defined in equation 7.1 to include interactions other than electrostatic. Therefore to determine  $\alpha$  we performed first principles calculations (see ref (140) for the method) of the charge neutral defect, i.e. oxygen

vacancies in ‘bulk’ LAO which include the double donor electrons. One oxygen vacancy was placed in a simulation cell of  $1 \times 1 \times 8$ ,  $2 \times 2 \times 8$  and  $3 \times 3 \times 8$  unit cells of LAO to approximate 2D arrays of vacancies of various area densities. From the difference in formation energy per vacancy between the three calculations,  $\alpha$  was found to be  $0.8 \text{ eV}/(\text{vac}/\text{f.u.})^2$ , which was used in figure 7.2a).  $\alpha$  is formally defined as the interaction between vacancies at the film surface, however we believe this bulk value to be a good estimate. For the comparison with experiment, to account for any error associated with this determination we choose the range  $0 < \alpha < 8 \text{ eV}/(\text{vac}/\text{f.u.})^2$  in figure 7.2b) of section 7.3.

### 7.5.2 The dielectric constant, $\epsilon$

The dielectric constant,  $\epsilon$ , consists of lattice and electronic contributions. For LAO, we take  $\epsilon=28$  as the total for figure 7.2a), as consistent with ref. (167). When comparing with experiment, we note the error and inconstancy of DFT calculations of  $\epsilon$ , and additionally the effect of strain as highlighted in ref. (50). Due to this we choose the range  $21 < \epsilon < 46$  for figure 7.2b).

### 7.5.3 The surface/interface chemistry term, $C$

$C$  consists of three terms,

$$C = E_{\text{form},\mu=0}^0 + \mu + 2(E_{CV} - W) \quad (7.8)$$

From the electronic structure presented by Li *et al.* (LDA calculations of the LAO-STO slab including surface oxygen vacancies (200)), the last term is found to be approximately -1.2 eV. From first principles calculations of ref. (208) the formation energy of an isolated oxygen vacancy at the surface of LAO (in the absence of a field) with reference to oxygen in an isolated molecule ( $1/2E[O_2]$ ),  $E_{\text{form},\mu=0}^0$ , is approx. 6.0 eV. We define the zero of chemical potential relative to this reference state, which is appropriate for the DFT comparison and hence the

## 7. SURFACE DEFECTS AND CONDUCTION IN POLAR OXIDE HETEROSTRUCTURES

---

value of  $C$  used in figure 7.2a) is taken as 4.8 eV.

The DFT underestimation of the band gap requires corrections to both  $E_{\text{form},\mu=0}^0$  (see ref. (209)) and  $W$  for the comparison with experiment in figure 7.2b). At this point we note the difficulties and variation in first principles determination of formation energies of donor/acceptor states (see for example ref. (210)).

From ref. (209), the formation energy correction of a donor defect, required due to DFT band gap underestimation is simply:

$$\Delta E_{\text{form}}^0 = Z\Delta E_c \quad (7.9)$$

where  $\Delta E_c$  is the change in conduction band edge between LDA and experiment (or corrected DFT). By comparing the electronic structure presented in Li *et al.* and ref. (211), this correction could be as large as 1.0 eV. Therefore we take  $6.0 \text{ eV} < E_{\text{form},\mu=0}^0 < 7.0 \text{ eV}$ .

From experimental band alignment (78) and theoretical calculations determining the gap states (211), the third term in equation 7.8 is approximately 2.0 eV (not 1.2 eV). Correcting for these DFT errors we take,

$$4.0 \text{ eV} + \mu < C < 5.0 \text{ eV} + \mu \quad (7.10)$$

The chemical potential of oxygen in the growth conditions used in ref. (59) ( $T = 1073 \text{ K}$  and  $p = 2.0 \times 10^{-8} \text{ atm}$ ) relative to the zero reference defined above is calculated to be -1.9 eV assuming the environment acts as an ideal gas-like reservoir. The effect of post-annealing and cooling to room temperature and pressure is to shift the chemical potential towards zero. With these limits on the chemical potential and the inequality in Eq. 7.10, the range of  $C$  becomes  $2.1 \text{ eV} < C < 5.0 \text{ eV}$ , as used in figure 7.2b).

# Chapter 8

## Chemical and electrochemical ferroelectric switching

### Chapter Summary

In the previous chapter we discussed the stability of surface redox defects in LAO thin films. This chapter extends the discussion to ferroelectric BaTiO<sub>3</sub> (BTO) thin films with switchable polarisation. Against expectations, robust switchable ferroelectricity has been recently observed in ultrathin (1 nm) BTO films exposed to air [V. Garcia *et al.*, Nature (London) **460**, 81 (2009) (5)]. Based on first-principles calculations, we show that the system does not polarise unless charged defects or adsorbates form at the surface. We propose electrochemical processes as the most likely origin of this charge. The ferroelectric polarisation of the film adapts to the external ionic charge generated on its surface by redox processes when poling the film. This, in turn, alters the band alignment at the bottom electrode interface, explaining the observed tunnelling electroresistance. A magnetoelectric effect is also predicted. Our conclusions are supported by energetics calculated for varied electrochemical scenarios. <sup>1</sup>

---

<sup>1</sup>The results presented in this chapter have been published in the article of Bristowe, Stengel, Littlewood, Pruneda and Artacho Phys. Rev. B **85**, 024106 (2012) (212).

## 8. CHEMICAL AND ELECTROCHEMICAL FERROELECTRIC SWITCHING

---

### 8.1 Introduction

Complex oxides have long been viewed as possible candidates for the next generation of electronic devices, which require reduced feature sizes, enhanced operating speeds and low consumption. Amongst oxides, ferroelectrics offer the ability to store information in a non-volatile manner via fast reversible polarisation switching in ferroelectric random-access memory (FeRAM). The observation of giant tunnelling electroresistance (TER) (5) in ultrathin (3 unit cells) ferroelectric films has recently opened a novel paradigm for device design based on these materials (6; 7).

Although the experiments (5) ascribed TER to ferroelectricity, which appeared robust and switchable, how the polar state is stabilised in such thin films is by no means established. In principle, a ferroelectric film with an exposed surface cannot sustain a monodomain polarisation perpendicular to the surface, because of the strong depolarising field that would inevitably arise<sup>1</sup>. Charged particles from the environment could in principle cancel the depolarising field (213) (figure 8.1 left). So far, however, the only chemical control of switching in air relates to neutral species, O<sub>2</sub> (32; 33; 34) (figure 8.1 centre). It is then not clear how neutral gas-phase molecules could interact with a biased atomic force microscopy (AFM) tip to produce the polar state.

Here we argue that the voltage applied with the AFM tip induces electrochemical switching (figure 8.1 right), i.e. redox processes that are essential to liberate free charge and therefore screen the depolarising field. This process would act as a nanobattery, rather than a nanocapacitor. Note that the same mechanism could explain other effects at oxide interfaces, such as the switchable two-dimensional electron gas (2DEG) at the LaAlO<sub>3</sub>/SrTiO<sub>3</sub> interface (70; 148) (see chapter 7), where the switching appears to be mediated by surface charge (75).

To explore this mechanism we consider the system studied experimentally in

---

<sup>1</sup> The polarisation is clearly observed to be perpendicular to the interface, consistent with the expected behaviour of compressively strained films (23).

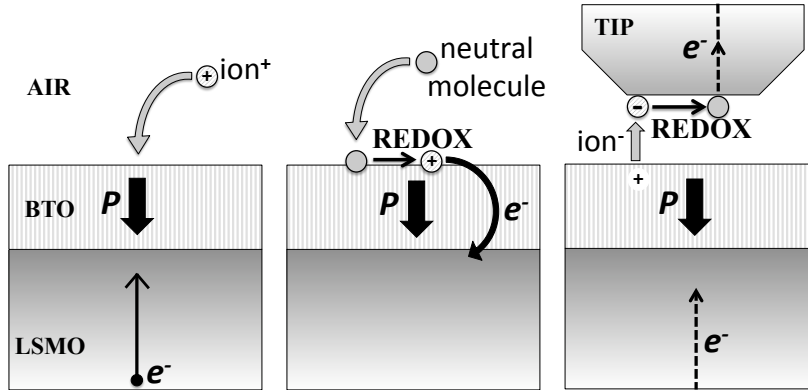


Figure 8.1: Schematic illustration of the conventional (left) and redox (centre) mechanisms for ferroelectric screening in the absence of a top electrode. The presence of a biased tip can promote an alternative redox mechanism that provides an external circuit for the screening electrons (right).

Ref. (5), consisting of a compressively strained nanometer-thick  $\text{BaTiO}_3$  (BTO) film on a  $\text{La}_{0.7}\text{Sr}_{0.3}\text{MnO}_3$  (LSMO) bottom electrode. Here we show, using first principles calculations, that (i) the pristine system (clean BTO surface with an ideal  $\text{TiO}_2$  termination) does not allow for a ferroelectric polarisation,  $P$ , normal to the surface despite the large compressive strain; (ii) a non-zero  $P$  is crucially dependent on the presence of a surface external ionic charge, in the form of defects or adsorbates; and (iii) the energetics for the formation of oxidised or reduced surface defects support the electrochemical switching model. We also find (iv) a systematic change in band offset with screening charge density, which we identify as the microscopic mechanism behind the experimentally observed TER (5), and (v) a large magnetoelectric coupling, due to the accumulation or depletion of spin-polarised carriers at the interface with ferromagnetic LSMO. The connection between these effects can be summarised as follows: under open-circuit boundary conditions the electric displacement field  $D$  within the film, the change in magnetisation at the interface  $\Delta M$  and the interface dipole, are all proportional (or equal) to the external ionic charge density,  $Q$  per unit surface

## 8. CHEMICAL AND ELECTROCHEMICAL FERROELECTRIC SWITCHING

---

$S$ , produced by the redox processes.

### 8.2 Methods

The density-functional theory (DFT) calculations are performed using the spin-polarised Wu-Cohen (WC) exchange-correlation functional (172), as implemented in the SIESTA code (114; 115)<sup>1</sup>. We find GGA-WC to reproduce bulk (214) and surface (214; 216) properties of LSMO that were calculated using the Perdew-Burke-Ernzerhof (PBE) scheme (191); at the same time, GGA-WC is more appropriate for ferroelectric oxides (mainly due to the improved ground state lattice parameter over other GGA's, for which ferroelectricity is extremely sensitive to, see ref. (172)). The LSMO/BTO system consists of 5.5 unit cells of LSMO (MnO<sub>2</sub>-terminated) stacked with 3 unit cells of BTO along the  $c$  direction in a slab geometry. The supercell contains a 15 Å thick vacuum layer and has either  $2\times 2$  or  $\sqrt{2}\times\sqrt{2}$  in-plane periodicity (see figure 8.2). The 5.5 unit cells of LSMO are thick enough to show bulk-like features in the center, and 3 unit cells of BTO was experimentally shown to be thick enough for ferroelectricity (5). We use a dipole correction to simulate open-circuit boundary conditions, enforcing zero macroscopic electric field in the vacuum layer. We constrain the in-plane lattice parameter to experimental bulk NdGaO<sub>3</sub> (NGO) to reproduce the experimental conditions of Ref. (5); this imposes a large (3%) compressive strain on BTO. Based on this slab geometry, we perform a number of calculations where we vary the surface composition by introducing defects or adsorbates. In particular, we simulate the clean TiO<sub>2</sub>-terminated surface (we shall refer to this structure as “pristine” henceforth); one O vacancy (“O-vac”) or adatom (“O-ads”) per  $2\times 2$  surface cell; one H adatom (“H”) or OH group (“OH”) per  $\sqrt{2}\times\sqrt{2}$  cell<sup>2</sup>. Hereafter we shall discuss the results with special regard for the presence or absence

---

<sup>1</sup> Details of the pseudopotentials, numerical atomic orbitals and LSMO doping are given in Ref. (214) and (215).

<sup>2</sup>Atomic forces were relaxed to less than 40 meV/Å.

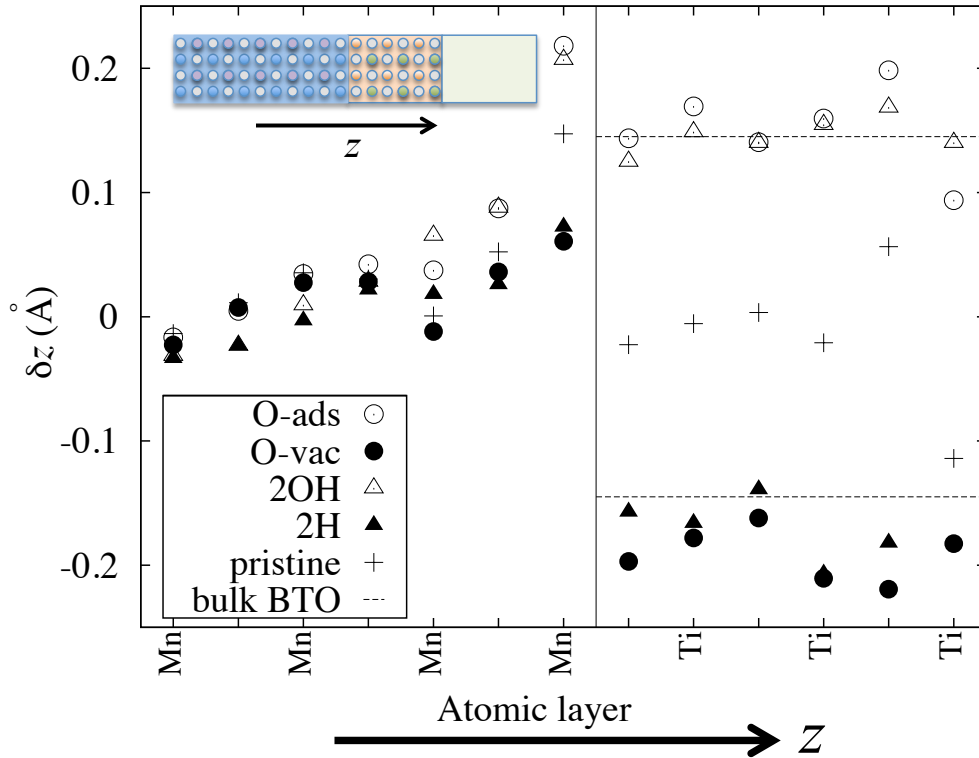


Figure 8.2: Cation-anion splittings,  $\delta z = z_{\text{cation}} - z_{\text{anion}}$  through the LSMO/BTO slab (the bottom half of LSMO is not shown). The dotted lines correspond to the average of the AO and  $\text{BO}_2$  layer anion-cation splitting for the inwards and outwards  $P$  in bulk BTO, strained to NGO.

of ferroelectric polarisation in each case.

## 8.3 Discussion

### 8.3.1 The pristine system

Figure 8.2 shows the relaxed out-of-plane structural distortions as a function of the surface chemical environment. The pristine system is characterised by negligible distortions in the interior of the BTO film, suggesting the absence of macroscopic  $P$  in this system. Only a surface rumpling is present, resulting in a

## 8. CHEMICAL AND ELECTROCHEMICAL FERROELECTRIC SWITCHING

---

small net inwards dipole (non-switchable) that decays rapidly towards the bulk (a surface rumpling is a known general feature of oxide surfaces, in particular the  $\text{TiO}_2$  termination of BTO (217; 218)). A vanishing  $P$  is consistent with the open-circuit boundary conditions, despite the large compressive strain. In absence of a top electrode the macroscopic electric displacement field  $D$  in BTO is equal and opposite to the density of external surface charge. As this charge is zero at the clean  $\text{TiO}_2$  surface, the film is constrained to a paraelectric state. It can be illustrative to consider briefly the thermodynamics of the problem within Landau-Ginzburg-Devonshire (LGD) theory (15; 16) (see chapter 1). The free energy density,  $U$ , of a ferroelectric film in open-circuit boundary conditions can be approximated as,

$$U = U_0 + f(T, P) - \boldsymbol{\mathcal{E}}_{\text{D}} \cdot \mathbf{P}, \quad (8.1)$$

where  $U_0$  includes all terms that are independent of the polarisation,  $\boldsymbol{\mathcal{E}}_{\text{D}}$  is the internal electric field or depolarising field within the film and  $f(T, P)$  is the LGD bulk ferroelectric free energy density, which in simplified form can be expressed as,

$$f(T, P) = a_1 P^2 + a_{11} P^4 + a_{111} P^6, \quad (8.2)$$

assuming the polarisation is fixed along the normal direction, where the coefficients of the expansion are both temperature and strain dependent. In absence of the depolarising field effect (such as in closed circuit conditions and perfect screening) and below the transition temperature, the LGB function is a double well (since the quadratic term is negative) and the material spontaneously polarises. However under open-circuit conditions and in the absence of polarisation screening the depolarising field is large,  $\boldsymbol{\mathcal{E}}_{\text{D}} = -\mathbf{P}/\epsilon_0$ , which adds a dominating positive contribution to the quadratic term. The energy density function becomes a single well for practically all accessible temperatures and strains, rendering the material unpolarised.

### 8.3.2 Chemical switching

To illustrate possible screening scenarios, we now include representative surface defects <sup>1</sup>. The O-vac and O-ads systems are both characterised by large ferroelectric distortions (figure 8.2). These are comparable to the strained bulk, where we calculate a spontaneous polarisation  $P_s=0.369$  C/m<sup>2</sup> ( $0.35$  e/S). This result is again consistent with the constraint that  $D = -Q/S$ . In fact, one oxygen defect for every  $2\times 2$  unit cells ( $0.5$  e/S) yields a larger surface charge than what would be sufficient to screen  $P_s$ . This justifies the larger cation-anion rumpings that we obtain in the film compared with the bulk (figure 8.2). OH and H adatoms (with  $\sqrt{2}\times\sqrt{2}$  coverage to maintain  $Q/S$ ) produce distortions of similar magnitude (figure 8.2). This confirms the generality of the ferroelectric switching mechanism: the ferroelectric state really depends on the net surface charge, and not on the chemical identity of the adsorbed species.

In order to study the electrochemical switching (figure 8.1 right), we commence by analysing *chemical* switching (figure 8.1 centre). Both are controlled by redox processes that transform bound charge into free charge, allowing for an electronic transfer between the surface defect and the metal substrate, but have different associated chemical sources/drains and energetics. Chemical switching was recently shown in a system consisting of PbTiO<sub>3</sub> on SrRuO<sub>3</sub> (32; 33) and BTO films on Au or vacuum (34).

To assess whether these redox reactions are thermodynamically accessible in typical experimental conditions, we estimate the formation energy of the defective systems taking the reactions: 1) Slab(pristine)  $\rightarrow$  Slab(O-vac)+1/2O<sub>2</sub> and equivalent for O-ads, 2) 1/2H<sub>2</sub>O+1/4O<sub>2</sub>+Slab(pristine)  $\rightarrow$  Slab(OH) and 3) 1/2H<sub>2</sub>O+Slab(pristine)  $\rightarrow$  Slab(H)+1/4O<sub>2</sub>. The chemical potential of the relevant molecular species is set to the calculated total energy of the spin-polarised

---

<sup>1</sup> Sampling the entire phase space (redox species and density, temperature, partial pressure, polarisation) is beyond the scope of this work, but can be done within thermodynamic theory (see Ref. (219)).

## 8. CHEMICAL AND ELECTROCHEMICAL FERROELECTRIC SWITCHING

---

Table 8.1: The formation energy,  $E_{\text{form}}$ , of the defective systems for  $\text{O}_2$  and  $\text{H}_2\text{O}$  rich conditions (see text for definitions).

	O-vac	O-ads	OH	H
$E_{\text{form}}$ (eV)	+3.6	-0.4	-1.5	+0.9

molecule in a large cubic box <sup>1</sup>. At this point we note the difficulties and variation in first principles determination of formation energies of donor/acceptor states (see for example ref. (210)). The results are summarised in Table 8.1. They suggest that, whilst the oxygen adatom is likely to form under oxygen-rich conditions, the formation energy for the oxygen vacancy is possibly too high to form even in oxygen-poor conditions. The calculated OH and H formation energies suggest that water is a very likely redox intermediate. Note that  $\text{H}_2\text{O}$  is ubiquitous in most experiments performed in air, and was recently found to play a crucial role in AFM experiments performed on  $\text{LaAlO}_3/\text{SrTiO}_3$  (76). Since both sets of reactions involve oxygen, we therefore expect that altering the surrounding oxygen partial pressure would affect the stability of reduction or oxidation processes, consistent with the recently observed chemical switching (32).

### 8.3.3 Electrochemical switching

Now we discuss how the electrochemical processes could proceed in practice during the AFM switching experiments of Ref. (5) (general electrochemical processes on oxide surfaces are reviewed in Ref. (221; 222)). As schematically shown in figure 8.1 (right), a biased tip close to contact can remove surface ions. These would then undergo a redox reaction at the tip surface. This process is favoured by the energy associated with the biased external circuit,  $\sigma V_{\text{ext}}$ , but costs an en-

---

<sup>1</sup>We note an alternative method to determine the oxygen chemical potential, which bypasses the need for a first principles calculation of  $\text{O}_2$  in ref. (220).

ergy equal to the change in binding energy of the ion to the ferroelectric surface and to the tip surface,  $\Delta E_{\text{form}}$  (this effectively redefines the relevant chemical potential). Assuming a planar geometry, the Gibbs free energy of the system can be written as (see e.g. Ref. (219) or (223)) ,

$$\mathcal{G} = tf(P) + \mathcal{G}(\mathcal{E}) - \sigma V_{\text{ext}} + \frac{\Delta E_{\text{form}}}{S} \quad (8.3)$$

where  $t$  is the thickness of the film,  $f(P)$  is the LGD free energy density (see equation 8.2),  $\mathcal{G}(\mathcal{E})$  includes terms dependent on the electric field within the film and within the air region between film and biased tip surface and  $\sigma$  is the density of free carriers on the tip surface. Using the electrical boundary conditions (fixed bias) and Gauss's law, this energy can be minimised with respect to  $\sigma$  and  $P$ . We find that poling can stabilise redox defects if  $V_{\text{ext}} > \Delta E_{\text{form}}/Q$ , after which the equilibrium redox charge density,  $Q/S$ , and polarisation both grow with  $V_{\text{ext}}$ , from approximately  $P_s$ . This electrochemical process would then act as a nanobattery, rather than a nanocapacitor. By controlling the environment (species and chemical potential) and  $V_{\text{ext}}$ , one may be also able to selectively control the active redox reaction, potentially opening new routes to surface redox catalysis. After removal of the tip, the surface redox density from poling can remain, since the reverse reaction is now blocked by key reactants being removed with the tip. This would explain the observation of Ref. (5) that the domains are stable for a very long time after “writing”. Of course, lateral charge diffusion across domain boundaries (224) may still occur in principle, but kinetic barriers are likely to hinder such processes. Therefore the bulk polarisation,  $P_s$ , is expected to be an estimate of the equilibrium polarisation after poling. We note that unlike in the  $\text{LaAlO}_3/\text{SrTiO}_3$  system where the polarisation is driving the surface chemistry (148) (see chapter 7), in ferroelectric films we expect it is the surface chemistry (and poling) that is driving the polarisation. This is because the energy scale for changing the polarisation is much larger in  $\text{LaAlO}_3$  than in the ferroelectric.

## 8. CHEMICAL AND ELECTROCHEMICAL FERROELECTRIC SWITCHING

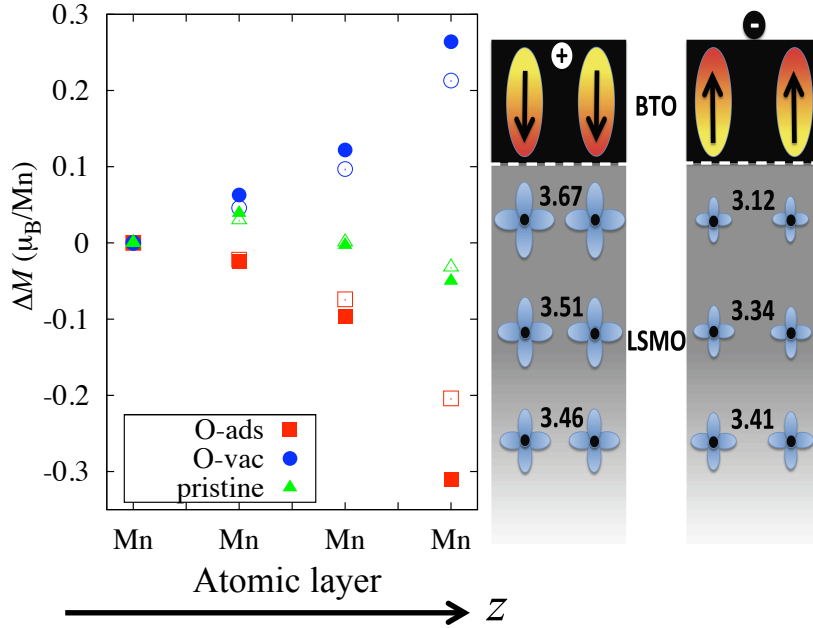


Figure 8.3: Change in Mn magnetic moment (left),  $\Delta M$ , near the interface (the interface  $\text{MnO}_2$  layer is on the right). Open symbols represent the change in  $3d e_g$  occupation, and closed symbols the total magnetic moment. A schematic illustration (right) of the effect of O-vac and O-ads on the BTO polarisation (arrows) and the Mn  $3d e_g$  occupation (blue lobes) and total Mn magnetic moment (numbers).

### 8.3.4 Magnetolectric coupling

The electronic transfer mechanism can be quantitatively estimated through the change in magnetisation of LSMO. LSMO is a half-metal with only Mn  $3d e_g$  majority spin levels around the Fermi level. As the screening carriers are fully spin-polarised, an electronic transfer between LSMO and the BTO surface results in a systematic change of the magnetisation near the interface. We calculate the change in magnetisation from the pristine to the O-vac and O-ads systems and to the 2OH and 2H systems,  $\Delta M$ , as  $\pm 1.7 \mu_B$  and  $\pm 1.5 \mu_B$  in the supercell, equivalent to  $\pm 0.42 e/S$  and  $\pm 0.37 e/S$  respectively (the remaining 0.1 electrons/holes stay in BTO, see section 8.5). This extra electron density (which

corresponds to the electric displacement,  $D$ , because of the half-metallic nature of LSMO) resides in the interface region, decaying into the electrode with an associated Thomas-Fermi screening length (see figure 8.3). This situation is similar to the carrier-mediated magnetoelectricity already predicted at SrTiO<sub>3</sub>/SrRuO<sub>3</sub> interfaces (225) and in LSMO/BTO superlattices (226).

In the latter it was recognised that LSMO has a magnetic phase transition at a doping concentration of approximately 0.5, opening the opportunity for not only a change in magnitude but also the ordering of the local magnetic moments. To check for a similar magnetic reconstruction, the alignment of the Mn magnetic moments were altered from parallel to various configurations. It should be noted that the transition to other spin alignments is expected to be disfavoured by GGA's. In agreement with Ref. (226) the ferromagnetic alignment was preferential except for the case when BTO is polarised outwards (surface O-ads and OH) which is very close to a ground state with interface Mn moments aligned anti-parallel to all other bulk Mn moments (called  $A_1$  in Table 1 of Ref. (226)). A similar magnetoelectric effect has recently been experimentally realised (227; 228). These effects could be utilised for spintronics applications. By engineering the LSMO surface with a ferroelectric capping layer, one may be able to enhance the Curie temperature of the LSMO surface (which is lower than the bulk (229)) and alter the interface spin density of states by switching the magnetic phase through ferroelectric polarisation reversal.

### 8.3.5 Tunneling Electroresistance

We now discuss how the electrochemical switching process may lead to the giant TER observed in the LSMO/BTO system (5). In the simplest semiclassical approximation, TER has an exponential dependence on the tunneling barrier shape (230). The interface dipole, and hence band offset ( $E_{VO} = E_{VBM} - E_f$ ), at a metal/ferroelectric interface depends linearly on the electric displacement field,  $D$ , in a way that can be expressed with an effective screening length (231; 232; 233),

## 8. CHEMICAL AND ELECTROCHEMICAL FERROELECTRIC SWITCHING

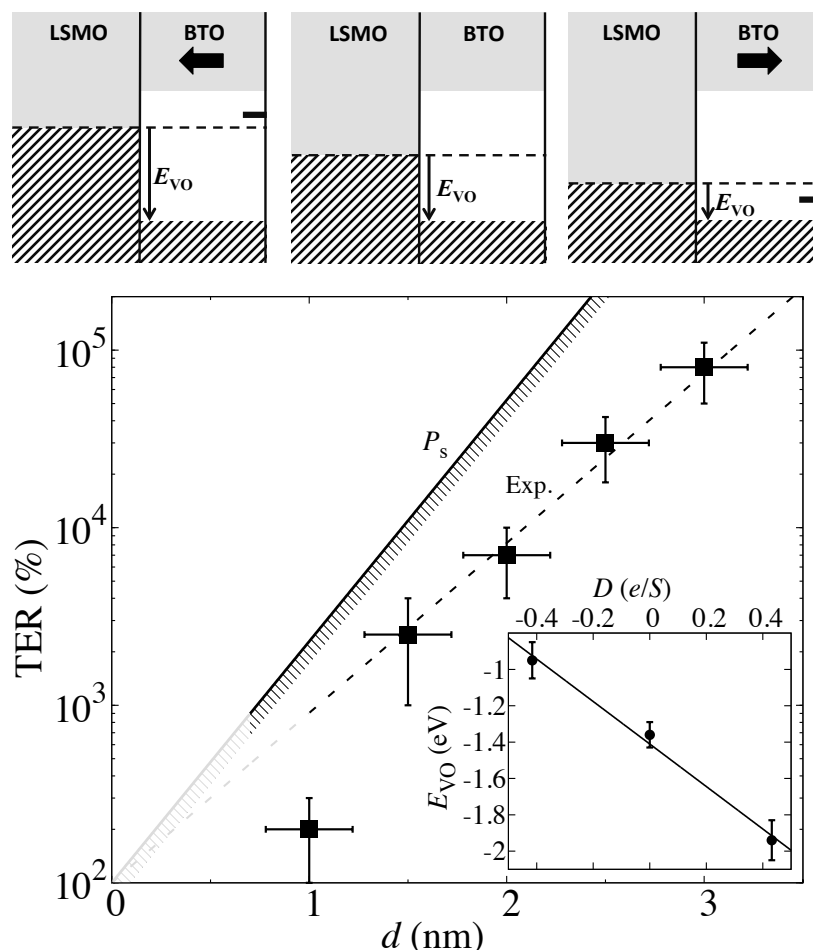


Figure 8.4: Top: Schematic illustration of the change in band offset,  $E_{VO}$ , with polarisation reversal. Bottom: Tunnel electroresistance (TER) vs BTO thickness. Experimental points taken from Garcia *et al.* (5) (squares with dashed line fit) are compared with a theoretical expression (230) which uses the tunneling barrier height expected from the BTO bulk polarisation,  $P_s$  (solid line). Inset: Calculated band offset against electric displacement field for the three BTO states. The straight line fit is used to determine the band offset (and hence barrier height) at  $\pm P_s$  for the TER plot.

$\lambda_{\text{eff}}$ . For LSMO-BTO we calculate  $\lambda_{\text{eff}} = 0.11 \text{ \AA}$ . Using the calculated values of the band offset (figure 8.4 inset) and the experimental band gap of BTO, we obtain the change in barrier height upon complete polarisation reversal (for  $D = \pm P_s$  the potential in BTO is flat, i.e. the tunneling barrier shape is rectangular),  $\Delta\varphi$ , and the average barrier height,  $\bar{\varphi} = (\varphi_{\text{out}} + \varphi_{\text{in}})/2$ . These values then yield an estimate of the TER using the exponential dependence (230) on the barrier thickness,  $d$ , for large TER,

$$\text{TER} \approx \exp \left[ \frac{\sqrt{2m} \Delta\varphi}{\hbar} \frac{d}{\sqrt{\bar{\varphi}}} \right]. \quad (8.4)$$

Figure 8.4 compares this estimate with the experimental data (5) showing that this simple model captures remarkably well the essential physics of TER in this system. We note a recent study reported comparable shifts in  $E_{\text{VO}}$  (measured using photoelectron spectroscopy) on a similar ferroelectric/LSMO system upon polarisation reversal (234). The origin of electroresistance effects in oxide nanotubes has also recently been suggested as redox reactions (235). However the redox arguments there are fundamentally different - it is proposed that the electrons yielded by oxygen vacancies are directly available for conduction.

## 8.4 Conclusions

In conclusion we have studied an electrochemical mechanism for ferroelectric switching in thin films and proposed it as the origin of switchable ferroelectricity, TER and magnetoelectricity in a prototypical system. This work opens several avenues for future research. From the experimental point of view, it would be interesting to investigate the composition of a ferroelectric surface before and after switching (e.g. via the AFM tip), to verify whether reduced or oxidised gas-phase species are present (as suggested by our results). Also, this point could be indirectly checked by performing the AFM-mediated switching experiments in a controlled atmosphere, in analogy to the experiments of Bi et al. (76) on

## 8. CHEMICAL AND ELECTROCHEMICAL FERROELECTRIC SWITCHING

---

LAO/STO. From the theoretical point of view, a natural next step would be to perform a more detailed thermodynamic analysis of the stability of a ferroelectric surface (either pristine or decorated with adsorbates). This would involve exploring different coverages, possible inhomogeneous polarisation states, and the effect of temperature and other external perturbations. We hope that our results will stimulate further investigations along these (and possibly other) directions.

### 8.5 Structural details

Here we provide details of the electronic structure of the various LSMO/BTO systems. Figure 8.5 (a)-(e) shows the spin-resolved layer-by-layer density of states for the pristine, O-ads, O-vac, 2OH and 2H systems. As discussed in section 8.3, the electric displacement and polarisation within BTO,  $D$  and  $P$ , and hence the valence band offset,  $E_{VO}$ , depend only on  $Q/S$ , the surface defect charge density, and not the surface chemistry. However, as discussed in Ref. (157), this is not strictly the case once  $E_{VO}$  becomes negative or reaches the band gap of BTO. At this point electrons or holes “spill out” in to the BTO layer. This “charge spill out” regime is favoured by DFT, which often underestimates the band gap, and therefore can be an artefact of the calculation.

In our case, due to the presence of a free surface, there is a further issue that was not explicitly considered in (157), i.e. the effect of surface states. In many cases, these fall within the bulk band gap of the ferroelectric film, and might cross the Fermi level of the metal, thus causing a significant spill-out of charge even when the bulk electronic bands are not directly affected. Note that surface states in ferroelectrics typically have a marked localised orbital character (either the atomic orbital of an adsorbate, or the  $3d$  orbitals of the transition metal cation). Therefore, it is reasonable to suspect that DFT might introduce systematic errors in their ionisation energies (similarly to the energy location of the bulk band edges discussed in (157)), and the metallisation of a surface state

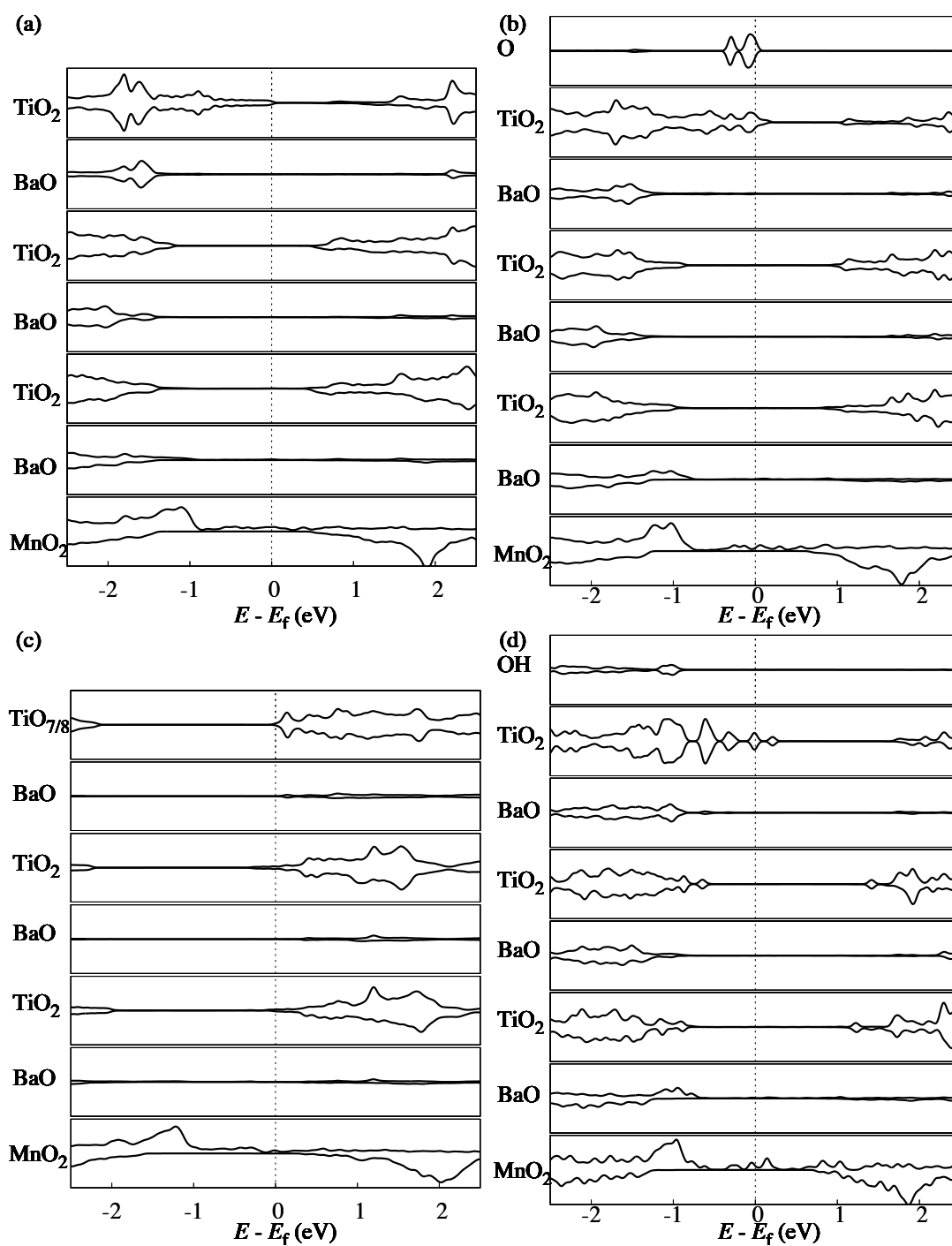


Figure 8.5 (see over)

## 8. CHEMICAL AND ELECTROCHEMICAL FERROELECTRIC SWITCHING

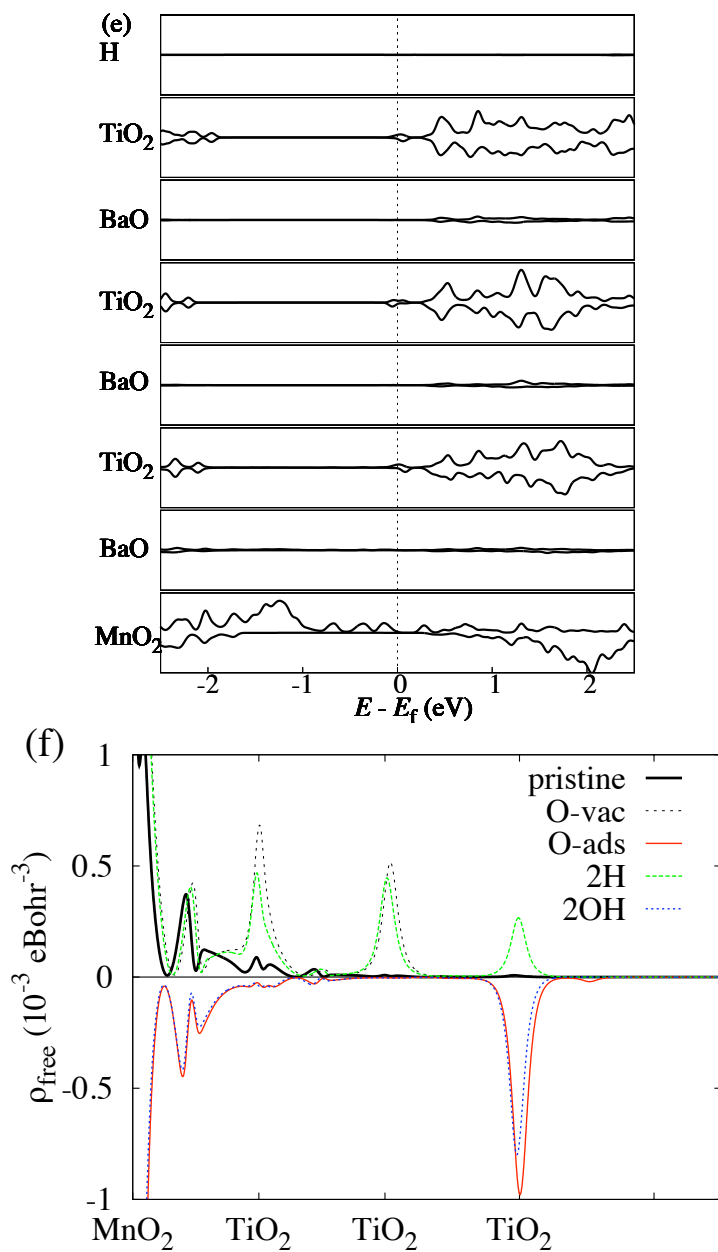


Figure 8.5: Spin-resolved layer-by-layer density of states centred around  $E_f$  for the LSMO/BTO systems. Positive DOS represents majority spin, negative DOS minority spin. Only the BTO layers (and 1 LSMO layer) are shown for clarity. Panels (a)-(e) correspond to pristine, O-ads, O-vac, 2OH and 2H systems respectively. Panel (f) shows a profile of  $\rho_{\text{free}}$  through the various LSMO/BTO systems.

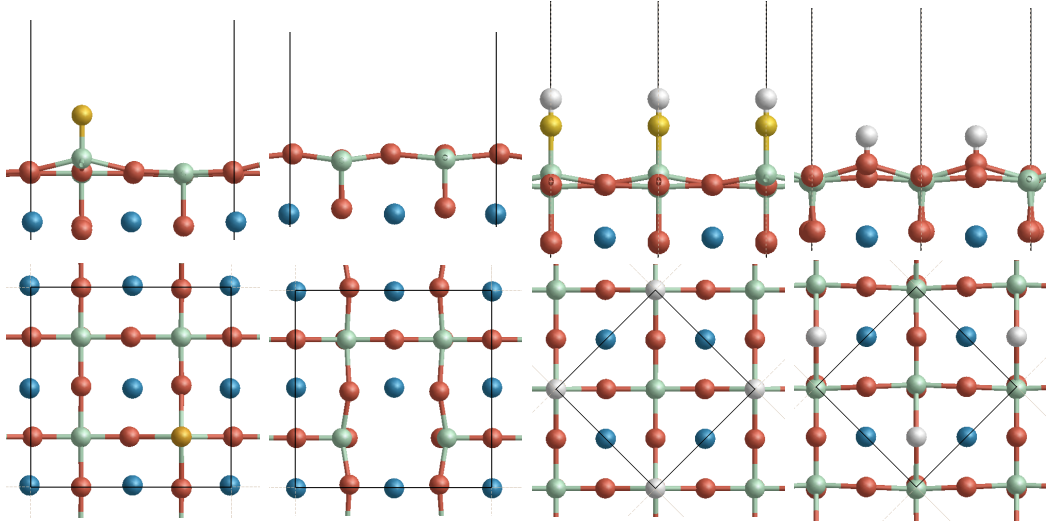


Figure 8.6: Relaxed surface LSMO/BTO structure. Top: view along the  $[100]$  direction. Bottom: birds-eye view along the  $[001]$  direction. Only the top BTO layer is shown for clarity. Sr (blue), Ti (cyan), O (red), O-ads (orange). Panels correspond to O-ads, O-vac, 2OH and 2H systems respectively (left to right).

should be regarded with analogous caution (for a detailed discussion of charge transfers at surfaces see, e.g., Ref. (29)).

Refs. (157) and (29) prescribe an analysis of the hole- and electron-like charge spill out. Following this prescription, we determine the free electron density profile,  $\rho_{\text{free}}$ , within BTO in figure 8.5(f) (using Eq. 25 and 26 of Ref. (157) and Eq. 19 of Ref. (29) for hole spill out). Out of all the five systems, the pristine one is unaffected, the negatively polarised (O-vac and 2H) systems are affected by electron spill out into the conduction band, and the two positively polarised (O-ads and 2OH) ones are affected by hole spill out into surface states (see figure 8.5). In both O-vac and 2H  $\rho_{\text{free}}$  amounts to approximately 0.03 electrons per unit cell of BTO, which is a fairly mild effect (compare with approximately 0.15 electrons per unit cell in the KNO/SRO system of Ref. (157)). In the case of O-ads and 2OH, the surface O( $2p$ ) states accommodate a total of approximately 0.1 holes per surface perovskite unit (figure 8.5(f)). Of course, estimating to what degree this charge spill is problematic, depends not only on the magnitude

## 8. CHEMICAL AND ELECTROCHEMICAL FERROELECTRIC SWITCHING

---

but also the purpose of the calculation. The charge spill out induces an error in two quantities that are discussed in this work: the total injected charge into the LSMO electrode, and the band alignment. Considering the total injected charge, the impact of this error is trivial to estimate. In fact, 0.03 electrons per cell times  $N$ , number of BTO cells, corresponds exactly to the difference between the actual induced spin in LSMO and the “ideal” limit of 2 Bohr magnetons per cell. This observation can be directly used to estimate the error in the calculated band offset. In fact, we can assume in a first approximation that the band offset is linear in the electric displacement of the BTO cell adjacent to the interface,  $D_{\text{inter}}$ . Using the above numbers for the O-vac system,

$$D_{\text{inter}} = 2e/S - 0.03e(N/S) = M/S = 1.7e/S, \quad (8.5)$$

where  $M$  is the induced spin, and  $S$  is the supercell surface area (or reciprocal of the defect density). This provides an accurate estimate of the actual electric displacement “felt” by LSMO. Using this information, therefore, we can make a very accurate estimation of the linear band offset dependence with  $D$ . We used this analysis to make the plot shown in figure 8.4 inset of the main text. Therefore, whilst we understand the limitations of DFT, in this case they do not affect significantly our conclusions.

Figure 8.6 displays the relaxed atomic structures of the BTO surface with O-ads, O-vac, 2OH and 2H.

# Chapter 9

## Conclusions and outlook

The objectives of this thesis were summarised by the following questions in the introduction: (i) can the polarisation of LAO be utilised further to create new electronic properties? (chapter 5), (ii) since interfaces between centrosymmetric materials can be charged, are there other symmetries in different materials which also allow polar surfaces? (chapter 6), (iii) are defects instead likely to play a role in the origin of the 2DEG at the LAO-STO interface? (chapter 7), and (iv) can these polarity arguments and screening models also apply to the prototypical polar materials - ferroelectrics? (chapter 8). In each chapter we provide evidence to suggest the answer to each question is indeed ‘yes’. Perhaps the most important conclusion resulting from this thesis is, arguably, that even very simple models for electrostatics and energetics can provide important understanding, along with experiment, for fundamental processes at interfaces between materials.

Since the origin of the LAO-STO interface 2DEG, a key subject of this thesis, has been heavily debated in the literature, I would like to briefly note my perspective on the topic. The reason for the ongoing debate is clear - there is experimental evidence for all four possible origins (intrinsic polar catastrophe, surface redox defects, intermixing and STO vacancies). It is also quite possible that more than one mechanism is involved at once, or under different experimental conditions. Clearly more effort from both theory and experiment is needed,

## 9. CONCLUSIONS AND OUTLOOK

---

especially combined systematic studies making use of all possible techniques. For example a concentrated study on the effect of growth parameters, combined with transport and spectroscopy measurements on the same samples could clarify the issue. In my opinion, the mechanism which conflicts the least with all available data, and agrees at least qualitatively with a large proportion of experiments, is that of 2DEG formation via the formation of surface redox defects, stabilised through the field in LAO. The strongest evidence in favour of this is the 2DEG dependence (from both transport and spectroscopy measurements) on the LAO thickness and oxygen partial pressure, as well as the observation of the writing of surface charge during biased AFM tip field effect measurements.

The specific conclusions and suggestions for further study that have been drawn in this thesis are summarised below.

### **Oxide superlattices with alternating $n$ and $p$ interfaces**

- Density functional theory (DFT) calculations find an insulator to metal transition (IMT) in pristine LAO-STO superlattices with increasing layer thickness, producing two-dimensional electron and hole gases at alternating interfaces.
- The electrostatic potential from the DFT calculations agrees remarkably well with a model of capacitor plates, taking precisely  $\pm 0.5$  electrons per two-dimensional unit cell at alternating interfaces within the insulating regime.
- This net charge is exactly what one obtains by taking formal charges of the ions, irrespective of covalency, which is argued to be correct within the framework of the modern theory of polarisation by taking ion cores and Wannier centres for the electrons.
- Once the potential drop coincides with the band gap at the critical thickness, electrons transfer from the  $p$  to the  $n$  interface, pinning the potential

---

drop.

- Since the IMT is sensitive to the polarisation and dielectric response of each layer, we predict that by utilising epitaxial strain and the paraelectric-ferroelectric phase boundary in STO, a piezoresistance effect may be found, as confirmed by additional DFT calculations.
- These oxide systems are argued to be a promising opportunity to observe the so-far elusive excitonic insulator.
- Suggestions for further study:
  - The effect of the typical oxygen octahedra rotations found in many perovskites such as LAO is usually ignored in the literature of LAO-STO, since it is not thought to affect the dielectric response or the polarisation of LAO. Rotations have been experimentally observed in the LAO film (236), which penetrate into the STO surface, and it could find some surprises on the theoretical front.
  - The possible polaronic effects of the 2DEG hinted by experiment (81), have not yet been fully investigated theoretically.
  - Further theoretical and experimental investigation into excitonic properties of oxide superlattices is needed.

### **Proposal of a one-dimensional electron gas in the steps at the $\text{LaAlO}_3$ - $\text{SrTiO}_3$ interface**

- Vicinal LAO (001) surfaces with steps of 1 unit cell in height (as observed in most grown samples) are argued to affect the surface net charge. This is due to a charge density at the step edge, in addition to the terrace, of magnitude  $\pm 0.5$  electrons per two-dimensional unit cell. An equivalent picture takes the component perpendicular to the stepped surface of the formal polarisation of LAO.

## 9. CONCLUSIONS AND OUTLOOK

---

- The electrostatics of the stepped interface are studied with a capacitor plate model, supported by DFT calculations, showing an alteration of the interface carrier density with miscut angle.
- A one-dimensional electron gas is predicted for small miscut angles and a LAO thickness near the pristine critical.
- Suggestions for further study:
  - This prediction welcomes both experimental and theoretical attempts for the search of the 1DEG and, if found, the properties of the 1DEGs.
  - It remains to be seen whether excitonic properties can be found in oxide superlattices with 2D electron hole gases, but it would be interesting to see whether the change in dimensions to 1D electron and hole gases could affect possible excitonic effects.

### **Polarisation classes of two-dimensional honeycomb compounds**

- The formal polarisation in two-dimensional II-VI, III-V and IV-IV honeycomb compounds is found to be equivalent to that of taking the formal ionic charge of each species, irrespective of covalency.
- Due to the three-fold rotational symmetry, we formulate three distinct classes of honeycomb compounds based on their polarisation.
- Interfaces between materials from different classes are charged, and an electronic screening mechanism not dissimilar to that observed in oxides (see chapter 4) is found beyond a critical thickness.
- The result is one-dimensional electron and hole gasses at alternating interfaces, which in some cases are predicted to be half-metallic.
- Suggestions for further study:

- 
- Axial epitaxial strain (and many other types for example sheet bending) removes the three-fold rotational symmetry in these honeycomb compounds, potentially inducing a non-trivial electronic polarisation component on top of the one mentioned above. These piezoelectric (or flexoelectric) properties would be an interesting area of research.
  - The stray field in these honeycomb superlattices could be potentially utilised to modulate the carrier density of a graphene sheet lying parallel.

## Surface defects and conduction in polar oxide heterostructures

- A model for the formation of surface redox processes, specifically surface O vacancies, in polar thin films is presented and applied to the LAO/STO system as a potential mechanism for the origin of the two-dimensional electron gas.
- The process is favoured with increasing film thickness through the effect of the electric field within the film, and the growth of the equilibrium density of related surface defects with thickness is predicted past a critical minimum thickness. This is in excellent agreement with first principles calculations and in reasonable agreement with experimental measurements of Ti  $3d$  occupation.
- The potential drop across the film does not change substantially with thickness once vacancies start to appear in agreement with XPS measurements.
- The onset for conduction is predicted to be at a higher film thickness than the one for interfacial carrier population, due to trapping of the electrons in the potential generated by the vacancies for thin films.
- Suggestions for further study:

## 9. CONCLUSIONS AND OUTLOOK

---

- Direct experimental observation of the surface composition of the LAO surface as a function of thickness and atmospheric environment would be very enlightening as to whether surface processes are at play.
- Recent PFM and electrochemical strain microscopy experiments on LAO-STO suggest a PFM-like response. The removal of surface oxygen ions with the biased tip could be potentially one possible explanation. Further modelling and experiments will be required to understand these processes.
- The 2DEG at the LAO-STO interface has only been reproduced with a few polar films other than LAO (such as  $\text{LaGaO}_3$  and  $\text{DyScO}_3$ ). Much is to be done to confirm the generality of the mechanism as originating in the polarity, and not anything else (such as intermixing or STO vacancies).

### Chemical and electrochemical ferroelectric switching

- First principles calculations show that an ultrathin  $\text{BaTiO}_3$  film on a  $\text{La}_{0.7}\text{Sr}_{0.3}\text{MnO}_3$  (LSMO) bottom electrode does not allow for a ferroelectric polarisation normal to the surface despite large compressive strain, in the absence of surface external charges.
- A non-zero polarisation is crucially dependent on the presence of external ionic charges at the surface, in the form of defects or adsorbates. The energetics for the formation of several representative processes support chemical and electrochemical switching models.
- The first principles calculations show a systematic change in interface band offset with screening charge density, which we identify as the microscopic mechanism behind experimentally observed giant tunnelling electroresistance.

- 
- The calculations also show a large magnetoelectric coupling due to the accumulation or depletion of spin-polarised carriers at the interface with ferromagnetic LSMO upon BTO polarisation reversal.
  - Suggestions for further study:
    - Direct experimental observation of the surface ferroelectric composition after switching would verify whether reduced or oxidised gas-phase species are present, as predicted.
    - The growth of SrTiO<sub>3</sub> and BaTiO<sub>3</sub> thin films on Si surfaces is becoming a popular field of research for potential ferroelectric field effect transistors. The ferroelectric stability of these thin films in air will also be related to surface defects, as highlighted here.
    - The LSMO electrode is a highly studied material with a complex phase diagram. Understanding the structural, electronic and magnetic properties of the bare LSMO surface is a challenging but important step.

## 9. CONCLUSIONS AND OUTLOOK

---

# Bibliography

- [1] C. Howard and H. Stokes, “Group-theoretical analysis of octahedral tilting in perovskites,” *Acta Crystallographica Section B: Structural Science* **54**, 782 (1998). 2
- [2] H. Hwang, S. Cheong, P. Radaelli, M. Marezio, and B. Batlogg, “Lattice Effects on the Magnetoresistance in Doped LaMnO<sub>3</sub>,” *Phys. Rev. Lett.* **75**, 914 (1995). 3
- [3] Y. Tokura and Y. Tomioka, “Colossal magnetoresistive manganites,” *J. Magn. Mater.* **200**, 1 (1999). 3
- [4] B. Wul and J. M. Goldman, “Dielectric hysteresis in barium titanate,” *C.R. Acad. Sci URSS* **46**, 139 (1945). 3, 5
- [5] V. Garcia, S. Fusil, K. Bouzehouane, S. Enouz-Vedrenne, N. Mathur, A. Barthélémy, and M. Bibes, “Giant tunnel electroresistance for non-destructive readout of ferroelectric states,” *Nature* **460**, 81 (2009). 4, 108, 111, 112, 113, 114, 118, 119, 121, 122, 123
- [6] P. Zubko and J. Triscone, “Applied physics: A leak of information,” *Nature* **460**, 45 (2009). 4, 112
- [7] M. Segal, “Ferroelectric memory: Slim fast,” *Nature Nanotechnology* (2009). 4, 112

## BIBLIOGRAPHY

---

- [8] A. Chanthbouala, A. Crassous, V. Garcia, K. Bouzehouane, S. Fusil, X. Moya, J. Allibe, B. Dlubak, J. Grollier, S. Xavier, C. Deranlot, A. Moshar, R. Proksch, N. Mathur, N. Bibes, and A. Barthélémy, “Solid-state memories based on ferroelectric tunnel junctions,” *Nature Nanotechnology* **7**, 101 (2011). 4
- [9] J. Valasek, “Piezoelectric and Allied Phenomena in Rochelle Salt,” *Phys. Rev.* **15**, 537 (1920). 5
- [10] J. Valasek, “Piezo-Electric and Allied Phenomena in Rochelle Salt,” *Phys. Rev.* **17**, 475 (1921). 5
- [11] J. Valasek, “Piezo-electric activity of Rochelle salt under various conditions,” *Phys. Rev.* **19**, 478 (1922). 5
- [12] P. Tasker, “The stability of ionic crystal surfaces,” *Journal of Physics C: Solid State Physics* **12**, 4977 (1979). 5, 11, 12, 28
- [13] R. Comes, M. Lambert, and A. Guinier, “The chain structure of BaTiO<sub>3</sub> and KNbO<sub>3</sub>,” *Solid State Communications* **6**, 715 (1968). 6
- [14] R. Cohen, “Origin of ferroelectricity in perovskite oxides,” *Nature* **358**, 136 (1992). 6
- [15] A. Devonshire, “XCVI. Theory of barium titanate,” *Philos. Mag.* **40**, 1040 (1949). 8, 116
- [16] A. Devonshire, “CIX. Theory of barium titanate Part II,” *Philos. Mag.* **42**, 1065 (1951). 8, 116
- [17] M. Kawasaki, K. Takahashi, T. Maeda, R. Tsuchiya, M. Shinohara, O. Ishiyama, T. Yonezawa, M. Yoshimoto, and H. Koinuma, “Atomic control of the SrTiO<sub>3</sub> crystal surface,” *Science* **266**, 1540 (1994). 9

## BIBLIOGRAPHY

---

- [18] G. Koster, B. Kropman, G. Rijnders, D. Blank, and H. Rogalla, “Influence of the surface treatment on the homoepitaxial growth of SrTiO<sub>3</sub>,” *Materials Science and Engineering B* **56**, 209 (1998). 9
- [19] L. Freund and S. Suresh, *Thin film materials: stress, defect formation, and surface evolution* (Cambridge Univ Pr, 2003). 10
- [20] D. Chrisey and G. Hubler, editors, *Pulsed laser deposition of thin films* (John Wiley & Sons, Inc., New York, 1994). 10
- [21] C. Fennie and K. Rabe, “Magnetic and Electric Phase Control in Epitaxial EuTiO<sub>3</sub> from First Principles,” *Phys. Rev. Lett.* **97**, 267602 (2006). 11
- [22] J. Lee, L. Fang, E. Vlahos, X. Ke, Y. Jung, L. Kourkoutis, J. Kim, P. Ryan, T. Heeg, M. Roeckerath, V. Goian, M. Bernhagen, R. Uecker, P. Hammel, K. Rabe, S. Kamba, J. Schubert, J. Freeland, D. Muller, C. Fennie, P. Schiffer, V. Gopalan, E. Johnston-Halperin, and D. Schlom, “A strong ferroelectric ferromagnet created by means of spin-lattice coupling,” *Nature* **466**, 954 (2010). 11
- [23] D. Schlom, L. Chen, C. Eom, K. Rabe, S. Streiffer, and J. Triscone, “Strain Tuning of Ferroelectric Thin Films,” *Annu. Rev. Mater. Res.* **37**, 589 (2007). 11, 112
- [24] N. Pertsev, A. Zembilgotov, and A. Tagantsev, “Effect of mechanical boundary conditions on phase diagrams of epitaxial ferroelectric thin films,” *Phys. Rev. Lett.* **80**, 1988 (1998). 11
- [25] D. Schlom, L. Chen, X. Pan, A. Schmehl, and M. Zurbuchen, “A thin film approach to engineering functionality into oxides,” *J. Am. Ceram. Soc.* **91**, 2429 (2008). 11
- [26] P. Zubko, S. Gariglio, M. Gabay, P. Ghosez, and J. Triscone, “Interface

## BIBLIOGRAPHY

---

- physics in complex oxide heterostructures,” *Annu. Rev. Condens. Matter Phys.* **2**, 141 (2011). 11
- [27] J. Goniakowski, F. Finocchi, and C. Noguera, “Polarity of oxide surfaces and nanostructures,” *Rep. Prog. Phys.* **71** (2008). 11, 12, 28, 46, 47, 53, 60, 68
- [28] N. Bristowe, P. Littlewood, and E. Artacho, “The net charge at interfaces between insulators,” *J. Phys.: Condens. Matter* **23**, 081001 (2011). 13, 45, 74, 88, 98, 101, 106
- [29] M. Stengel, “Electrostatic stability of insulating surfaces: Theory and applications,” *Phys. Rev. B* **84**, 205432 (2011). 13, 76, 88, 127
- [30] D. Vanderbilt and R. King-Smith, “Electric polarization as a bulk quantity and its relation to surface charge,” *Phys. Rev. B* **48**, 4442 (1993). 13, 40, 47, 51, 74, 90
- [31] W. Harrison, E. Kraut, J. Waldrop, and R. Grant, “Polar heterojunction interfaces,” *Phys. Rev. B* **18**, 4402 (1978). 13
- [32] R. Wang, D. Fong, F. Jiang, M. Highland, P. Fuoss, C. Thompson, A. Kolpak, J. Eastman, S. Streiffer, and A. Rappe, “Reversible Chemical Switching of a Ferroelectric Film,” *Phys. Rev. Lett.* **102**, 47601 (2009). 13, 101, 108, 112, 117, 118
- [33] D. Fong, A. Kolpak, J. Eastman, S. Streiffer, P. Fuoss, G. Stephenson, C. Thompson, D. Kim, K. Choi, C. Eom, I. Grinberg, and A. Rappe, “Stabilization of Monodomain Polarization in Ultrathin PbTiO<sub>3</sub> Films,” *Phys. Rev. Lett.* **96**, 127601 (2006). 13, 112, 117
- [34] J. Spanier, A. Kolpak, J. Urban, I. Grinberg, L. Ouyang, W. Yun, A. Rappe, and H. Park, “Ferroelectric phase transition in individual single-crystalline BaTiO<sub>3</sub> nanowires,” *Nano Lett.* **6**, 735 (2006). 13, 112, 117

- [35] A. Ohtomo and H. Y. Hwang, “A high-mobility electron gas at the  $\text{LaAlO}_3/\text{SrTiO}_3$  heterointerface,” *Nature* **427**, 423 (2004). 13, 14, 16, 22, 46, 47, 49, 60, 74, 88, 98
- [36] N. Nakagawa, H. Hwang, and D. Muller, “Why some interfaces cannot be sharp,” *Nat. Mater.* **5**, 204 (2006). 13, 15, 16, 17, 18, 20, 23, 24, 26, 28, 54, 74, 98
- [37] K. Hellwege and A. Hellwege, editors, *Landolt-Brönstein* volume 16a (Springer-Verlag, Berlin, Germany, 1981). 14
- [38] S. Hayward, F. Morrison, S. Redfern, E. Salje, J. Scott, K. Knight, S. Tarantino, A. Glazer, V. Shuvaeva, P. Daniel, M. Zhang, and M. Carpenter, “Transformation processes in  $\text{LaAlO}_3$ : Neutron diffraction, dielectric, thermal, optical, and Raman studies,” *Phys. Rev. B* **72** (2005). 14
- [39] J. Noland, “Optical absorption of single-crystal strontium titanate,” *Phys. Rev.* **94**, 724 (1954). 14
- [40] M. Capizzi and A. Frova, “Optical gap of strontium titanate (deviation from Urbach tail behavior),” *Phys. Rev. Lett.* **25**, 1298 (1970). 14
- [41] A. Kahn and A. Leyendecker, “Electronic energy bands in strontium titanate,” *Phys. Rev.* **135**, A1321 (1964). 14
- [42] S. Lim, S. Kriventsov, T. Jackson, J. Haeni, D. Schlom, A. Balbashov, R. Uecker, P. Reiche, J. Freeouf, and G. Lucovsky, “Dielectric functions and optical bandgaps of high-K dielectrics for metal-oxide-semiconductor field-effect transistors by far ultraviolet spectroscopic ellipsometry,” *J. Appl. Phys.* **91**, 4500 (2002). 14
- [43] D. de Ligny and P. Richet, “High-temperature heat capacity and thermal expansion of  $\text{SrTiO}_3$  and  $\text{SrZrO}_3$  perovskites,” *Phys. Rev. B* **53**, 3013 (1996). 14

## BIBLIOGRAPHY

---

- [44] B. Chakoumakos, D. Schlom, M. Urbanik, and J. Luine, “Thermal expansion of  $\text{LaAlO}_3$  and  $(\text{La,Sr})(\text{Al,Ta})\text{O}_3$ , substrate materials for superconducting thin-film device applications,” *J. Appl. Phys.* **83**, 1979 (1998). 14
- [45] H. Y. Hwang, “Tuning interface states,” *Science* **313**, 1895 (2006). 14, 15, 60
- [46] S. A. Pauli and P. R. Willmott, “Conducting interfaces between polar and non-polar insulating perovskites,” *J. Phys.: Condens. Matter* **20**, 264012 (2008). 14, 60
- [47] M. Huijben, A. Brinkman, G. Koster, G. Rijnders, H. Hilgenkamp, and D. Blank, “Structure–Property Relation of  $\text{SrTiO}_3/\text{LaAlO}_3$  Interfaces,” *Adv. Mater* **21**, 1665 (2009). 14, 17, 24, 29, 46, 60
- [48] J. Mannhart and D. Schlom, “Oxide Interfaces—An Opportunity for Electronics,” *Science* **327**, 1607 (2010). 14, 46, 60, 98
- [49] R. Pentcheva and W. Pickett, “Electronic phenomena at complex oxide interfaces: insights from first principles,” *J. Phys.: Condens. Matter* **22**, 043001 (2010). 14, 46, 60
- [50] H. Chen, A. M. Kolpak, and S. Ismail-Beigi, “Electronic and Magnetic Properties of  $\text{SrTiO}_3/\text{LaAlO}_3$  Interfaces from First Principles,” *Advanced Materials* **22**, 2881 (2010). 14, 16, 20, 24, 26, 27, 46, 60, 98, 105, 109
- [51] D. Schlom and J. Mannhart, “Oxide electronics: Interface takes charge over Si,” *Nat. Mater.* **10**, 168 (2011). 14, 24, 27, 46, 60, 74
- [52] A. Kalabukhov, R. Gunnarsson, J. Borjesson, E. Olsson, T. Claeson, and D. Winkler, “Effect of oxygen vacancies in the  $\text{SrTiO}_3$  substrate on the electrical properties of the  $\text{LaAlO}_3/\text{SrTiO}_3$  interface,” *Phys. Rev. B* **75** (2007). 16, 98

- [53] W. Siemons, G. Koster, H. Yamamoto, W. A. Harrison, G. Lucovsky, T. H. Geballe, D. H. A. Blank, and M. R. Beasley, “Origin of charge density at LaAlO<sub>3</sub> on SrTiO<sub>3</sub> heterointerfaces: Possibility of intrinsic doping,” *Phys. Rev. Lett.* **98** (2007). 16, 98
- [54] G. Herranz, M. Basletic, M. Bibes, C. Carretero, E. Tafrá, E. Jacquet, K. Bouzehouane, C. Deranlot, A. Hamzic, J.-M. Broto, A. Barthelemy, and A. Fert, “High mobility in LaAlO<sub>3</sub>/SrTiO<sub>3</sub> heterostructures: Origin, dimensionality, and perspectives,” *Phys. Rev. Lett.* **98** (2007). 16, 22, 98
- [55] W. Siemons, G. Koster, H. Yamamoto, T. H. Geballe, D. H. A. Blank, and M. R. Beasley, “Experimental investigation of electronic properties of buried heterointerfaces of LaAlO<sub>3</sub> on SrTiO<sub>3</sub>,” *Phys. Rev. B* **76** (2007). 16
- [56] M. Basletic, J. L. Maurice, C. Carretero, G. Herranz, O. Copie, M. Bibes, E. Jacquet, K. Bouzehouane, S. Fusil, and A. Barthelemy, “Mapping the spatial distribution of charge carriers in LaAlO<sub>3</sub>/SrTiO<sub>3</sub> heterostructures,” *Nat. Mater.* **7**, 621 (2008). 16, 17, 22, 25, 60
- [57] C. Cancellieri, N. Reyren, S. Gariglio, A. Caviglia, A. Fête, and J. Triscone, “Influence of the growth conditions on the LaAlO<sub>3</sub>/SrTiO<sub>3</sub> interface electronic properties,” *EPL (Europhysics Letters)* **91**, 17004 (2010). 17
- [58] S. Thiel, G. Hammerl, A. Schmehl, C. W. Schneider, and J. Mannhart, “Tunable quasi-two-dimensional electron gases in oxide heterostructures,” *Science* **313**, 1942 (2006). 17, 18, 21, 24, 27, 60, 74, 83, 98, 104, 105, 107
- [59] M. Sing, G. Berner, K. Goß, A. Müller, A. Ruff, A. Wetscherek, S. Thiel, J. Mannhart, S. Pauli, C. Schneider, P. R. Willmott, M. Gorgoi, F. Schafers, and R. Claessen, “Profiling the Interface Electron Gas of LaAlO<sub>3</sub>/SrTiO<sub>3</sub> Heterostructures with Hard X-Ray Photoelectron Spectroscopy,” *Phys. Rev. Lett.* **102**, 176805 (2009). 18, 19, 22, 24, 27, 99, 103, 104, 105, 110

## BIBLIOGRAPHY

---

- [60] G. Berner, S. Glawion, J. Walde, F. Pfaff, H. Hollmark, L. Duda, S. Paetel, C. Richter, J. Mannhart, M. Sing, and R. Claessen, “LaAlO<sub>3</sub>/SrTiO<sub>3</sub> oxide heterostructures studied by resonant inelastic x-ray scattering,” *Phys. Rev. B* **82**, 241405 (2010). 18, 19, 24, 27, 99, 105
- [61] Y. Segal, J. Ngai, J. Reiner, F. Walker, and C. Ahn, “X-ray photoemission studies of the metal-insulator transition in LaAlO<sub>3</sub>/SrTiO<sub>3</sub> structures grown by molecular beam epitaxy,” *Phys. Rev. B* **80**, 241107 (2009). 18, 27, 105
- [62] M. Huijben, G. Rijnders, D. Blank, S. Bals, S. Van Aert, J. Verbeeck, G. Van Tendeloo, A. Brinkman, and H. Hilgenkamp, “Electronically coupled complementary interfaces between perovskite band insulators,” *Nat. Mater.* **5**, 556 (2006). 18, 60, 69, 70, 71
- [63] R. Pentcheva, M. Huijben, K. Otte, W. Pickett, J. Kleibeuker, J. Huijben, H. Boschker, D. Kockmann, W. Siemons, G. Koster, H. Zandvliet, G. Rijnders, D. Blank, H. Hilgenkamp, and A. Brinkman, “Parallel electron-hole bilayer conductivity from electronic interface reconstruction,” *Phys. Rev. Lett.* **104**, 166804 (2010). 19, 27
- [64] M. Takizawa, S. Tsuda, T. Susaki, H. Y. Hwang, and A. Fujimori, “Electronic charges and electric potential at LaAlO<sub>3</sub>/SrTiO<sub>3</sub> interfaces studied by core-level photoemission spectroscopy,” *Phys. Rev. B* **84**, 245124 (2011). 19, 24, 27, 99, 105
- [65] G. Drera, F. Banfi, F. Canova, P. Borghetti, L. Sangaletti, F. Bondino, E. Magnano, J. Huijben, M. Huijben, G. Rijnders, D. Blank, H. Hilgenkamp, and A. Brinkman, “Spectroscopic evidence of in-gap states at the SrTiO<sub>3</sub>/LaAlO<sub>3</sub> ultrathin interfaces,” *Appl. Phys. Lett.* **98**, 2907 (2011). 19, 23, 106

- [66] C. Merckling, M. El-Kazzi, G. Delhayé, V. Favre-Nicolin, Y. Robach, M. Gendry, G. Grenet, G. Saint-Girons, and G. Hollinger, “Strain relaxation and critical thickness for epitaxial  $\text{LaAlO}_3$  thin films grown on  $\text{SrTiO}_3$  (001) substrates by molecular beam epitaxy,” *J. Cryst. Growth* **306**, 47 (2007). 19
- [67] S. Thiel, C. W. Schneider, L. F. Kourkoutis, D. A. Muller, N. Reyren, A. D. Caviglia, S. Gariglio, J. M. Triscone, and J. Mannhart, “Electron scattering at dislocations in  $\text{LaAlO}_3/\text{SrTiO}_3$  interfaces,” *Phys. Rev. Lett.* **102** (2009). 19
- [68] S. A. Pauli, S. J. Leake, B. Delley, M. Björck, C. W. Schneider, C. M. Schlepütz, D. Martocchia, S. Paetel, J. Mannhart, and P. R. Willmott, “Evolution of the Interfacial Structure of  $\text{LaAlO}_3$  on  $\text{SrTiO}_3$ ,” *Phys. Rev. Lett.* **106**, 036101 (2011). 20, 27, 105
- [69] C. Cancellieri, D. Fontaine, S. Gariglio, N. Reyren, A. Caviglia, A. Fête, S. Leake, S. Pauli, P. Willmott, M. Stengel, P. Ghosez, and J. Triscone, “Electrostriction at the  $\text{LaAlO}_3/\text{SrTiO}_3$  Interface,” *Phys. Rev. Lett.* **107**, 56102 (2011). 20, 27
- [70] C. Cen, S. Thiel, G. Hammerl, C. W. Schneider, K. E. Andersen, C. S. Hellberg, J. Mannhart, and J. Levy, “Nanoscale control of an interfacial metal-insulator transition at room temperature,” *Nat. Mater.* **7**, 298 (2008). 20, 21, 26, 27, 57, 74, 83, 98, 99, 103, 107, 112
- [71] S. Ishibashi and K. Terakura, “Analysis of Screening Mechanisms for Polar Discontinuity for  $\text{LaAlO}_3/\text{SrTiO}_3$  Thin Films Based on Ab initio Calculations,” *J. Phys. Soc. Jpn.* **77** (2008). 20, 23, 26
- [72] J. Lee and A. A. Demkov, “Charge origin and localization at the n-type  $\text{SrTiO}_3/\text{LaAlO}_3$  interface,” *Phys. Rev. B* **78**, 193104 (2008). 20, 21, 26, 60, 61

## BIBLIOGRAPHY

---

- [73] R. Pentcheva and W. Pickett, “Avoiding the Polarization Catastrophe in LaAlO<sub>3</sub> Overlayers on SrTiO<sub>3</sub>(001) through Polar Distortion,” *Phys. Rev. Lett.* **102**, 107602 (2009). 20, 26, 61
- [74] G. Rijnders and D. H. A. Blank, “Perovskite oxides - An atomic force pencil and eraser,” *Nat. Mater.* **7**, 270 (2008). 21
- [75] Y. Xie, C. Bell, T. Yajima, Y. Hikita, and H. Hwang, “Charge writing at the LaAlO<sub>3</sub>/SrTiO<sub>3</sub> surface,” *Nano Lett.* , 930 (2010). 21, 107, 112
- [76] F. Bi, D. Bogorin, C. Cen, C. Bark, J. Park, C. Eom, and J. Levy, “Water-cycle mechanism for writing and erasing nanostructures at the LaAlO<sub>3</sub>/SrTiO<sub>3</sub> interface,” *Appl. Phys. Lett.* **97**, 173110 (2010). 21, 118, 123
- [77] A. D. Caviglia, S. Gariglio, N. Reyren, D. Jaccard, T. Schneider, M. Gabay, S. Thiel, G. Hammerl, J. Mannhart, and J. M. Triscone, “Electric field control of the LaAlO<sub>3</sub>/SrTiO<sub>3</sub> interface ground state,” *Nature* **456**, 624 (2008). 21, 24
- [78] K. Yoshimatsu, R. Yasuhara, H. Kumigashira, and M. Oshima, “Origin of metallic states at the heterointerface between the band insulators LaAlO<sub>3</sub> and SrTiO<sub>3</sub>,” *Phys. Rev. Lett.* **101** (2008). 22, 110
- [79] O. Copie, V. Garcia, C. Bödefeld, C. Carrétéro, M. Bibes, G. Herranz, E. Jacquet, J. Maurice, B. Vinter, S. Fusil, K. Bouzehouane, H. Jaffrés, and A. Barthélémy, “Towards Two-Dimensional Metallic Behavior at LaAlO<sub>3</sub>/SrTiO<sub>3</sub> Interfaces,” *Phys. Rev. Lett.* **102**, 216804 (2009). 22
- [80] T. Fix, F. Schoofs, J. MacManus-Driscoll, and M. Blamire, “Charge confinement and doping at LaAlO<sub>3</sub>/SrTiO<sub>3</sub> interfaces,” *Phys. Rev. Lett.* **103**, 166802 (2009). 22

- [81] A. Dubroka, M. Rössle, K. Kim, V. Malik, L. Schultz, S. Thiel, C. Schneider, J. Mannhart, G. Herranz, O. Copie, M. Bibes, A. Barthélémy, and C. Bernhard, “Dynamical Response and Confinement of the Electrons at the  $\text{LaAlO}_3/\text{SrTiO}_3$  Interface,” *Phys. Rev. Lett.* **104**, 156807 (2010). 22, 23, 106, 131
- [82] R. Pentcheva and W. E. Pickett, “Charge localization or itineracy at  $\text{LaAlO}_3/\text{SrTiO}_3$  interfaces: Hole polarons, oxygen vacancies, and mobile electrons,” *Phys. Rev. B* **74**, 035112 (2006). 23, 24, 61
- [83] U. Schwingenschloegl and C. Schuster, “Exponential decay of relaxation effects at  $\text{LaAlO}_3/\text{SrTiO}_3$  heterointerfaces,” *Chem. Phys. Lett.* **467**, 354 (2009). 23
- [84] K. Janicka, J. Velez, and E. Tsybal, “Quantum Nature of Two-Dimensional Electron Gas Confinement at  $\text{LaAlO}_3/\text{SrTiO}_3$  Interfaces,” *Phys. Rev. Lett.* **102**, 106803 (2009). 23, 60, 61, 77
- [85] H. Chen, A. M. Kolpak, and S. Ismail-Beigi, “Fundamental asymmetry in interfacial electronic reconstruction between insulating oxides: An ab initio study,” *Phys. Rev. B* **79**, 161402 (2009). 23, 27, 60, 61
- [86] W. Son, E. Cho, B. Lee, J. Lee, and S. Han, “Density and spatial distribution of charge carriers in the intrinsic n-type  $\text{LaAlO}_3\text{-SrTiO}_3$  interface,” *Phys. Rev. B* **79**, 245411 (2009). 23, 71
- [87] M. Stengel, “First-principles modeling of electrostatically doped perovskite systems,” *Phys. Rev. Lett.* **106**, 136803 (2011). 23
- [88] J. Verbeeck, S. Bals, A. Kravtsova, D. Lamoen, M. Luysberg, M. Huijben, G. Rijnders, A. Brinkman, H. Hilgenkamp, D. Blank, and G. Van Tendeloo, “Electronic reconstruction at n-type  $\text{SrTiO}_3/\text{LaAlO}_3$  interfaces,” *Phys. Rev. B* **81**, 085113 (2010). 23

## BIBLIOGRAPHY

---

- [89] M. Salluzzo, J. Cezar, N. Brookes, V. Bisogni, G. De Luca, C. Richter, S. Thiel, J. Mannhart, M. Huijben, A. Brinkman, G. Rijnders, and G. Ghiringhelli, “Orbital Reconstruction and the Two-Dimensional Electron Gas at the  $\text{LaAlO}_3/\text{SrTiO}_3$  Interface,” *Phys. Rev. Lett.* **102**, 166804 (2009). 23
- [90] A. Savoia, D. Paparo, P. Perna, Z. Ristic, M. Salluzzo, F. Granozio, U. di Uccio, C. Richter, S. Thiel, J. Mannhart, and L. Marrucci, “Polar catastrophe and electronic reconstructions at the  $\text{LaAlO}_3/\text{SrTiO}_3$  interface: Evidence from optical second harmonic generation,” *Phys. Rev. B* **80**, 075110 (2009). 23
- [91] K. Zhou, M. Radovic, J. Schlappa, V. Strocov, R. Frison, J. Mesot, L. Patthey, and T. Schmitt, “Localized and delocalized Ti 3d carriers in  $\text{LaAlO}_3/\text{SrTiO}_3$  superlattices revealed by resonant inelastic x-ray scattering,” *Phys. Rev. B* **83**, 201402 (2011). 23
- [92] S. Gemming and G. Seifert, “ $\text{SrTiO}_3(001)|\text{LaAlO}_3(001)$  multilayers: A density-functional investigation,” *Acta Mater.* **54**, 4299 (2006). 23, 61
- [93] U. Schwingenschloegl and C. Schuster, “Surface effects on oxide heterostructures,” *Europhys. Lett.* **81** (2008). 23
- [94] Z. S. Popovic, S. Satpathy, and R. M. Martin, “Origin of the Two-Dimensional Electron Gas Carrier Density at the  $\text{LaAlO}_3$  on  $\text{SrTiO}_3$  Interface,” *Phys. Rev. Lett.* **101**, 256801 (2008). 23, 24, 60, 61, 77, 106
- [95] A. Brinkman, M. Huijben, M. Van Zalk, J. Huijben, U. Zeitler, J. C. Maan, W. G. Van der Wiel, G. Rijnders, D. H. A. Blank, and H. Hilgenkamp, “Magnetic effects at the interface between non-magnetic oxides,” *Nat. Mater.* **6**, 493 (2007). 24, 74
- [96] K. Janicka, J. P. Velev, and E. Y. Tsymbal, “Magnetism of  $\text{LaAlO}_3/\text{SrTiO}_3$  superlattices,” *J. Appl. Phys.* **103** (2008). 24

- [97] Z. Zhong and P. J. Kelly, “Electronic-structure induced reconstruction and magnetic ordering at the  $\text{LaAlO}_3$ — $\text{SrTiO}_3$  interface,” *Europhys. Lett.* **84**, 27001 (2008). 24
- [98] N. Reyren, S. Thiel, A. D. Caviglia, L. F. Kourkoutis, G. Hammerl, C. Richter, C. W. Schneider, T. Kopp, A.-S. Ruetschi, D. Jaccard, M. Gabay, D. A. Muller, J.-M. Triscone, and J. Mannhart, “Superconducting interfaces between insulating oxides,” *Science* **317**, 1196 (2007). 24, 74
- [99] L. Li, C. Richter, J. Mannhart, and R. Ashoori, “Coexistence of Magnetic Order and Two-dimensional Superconductivity at  $\text{LaAlO}_3/\text{SrTiO}_3$  Interfaces,” *Nature Physics* **7**, 762 (2011). 24, 74
- [100] J. Bert, B. Kalisky, C. Bell, M. Kim, Y. Hikita, H. Hwang, and K. Moler, “Direct imaging of the coexistence of ferromagnetism and superconductivity at the  $\text{LaAlO}_3/\text{SrTiO}_3$  interface,” *Nature Physics* **7**, 767 (2011). 24, 74
- [101] Ariando, X. Wang, G. Baskaran, Z. Liu, J. Huijben, J. Yi, A. Annadi, A. Barman, A. Rusydi, S. Dhar, Y. Feng, J. Ding, H. Hilgenkamp, and T. Venkatesan, “Electronic phase separation at the  $\text{LaAlO}_3/\text{SrTiO}_3$  interface,” *Nature Communications* **2**, 188 (2011). 24
- [102] P. R. Willmott, S. A. Pauli, R. Herger, C. M. Schlepuetz, D. Martoccia, B. D. Patterson, B. Delley, R. Clarke, D. Kumah, C. Cionca, and Y. Yacoby, “Structural basis for the conducting interface between  $\text{LaAlO}_3$  and  $\text{SrTiO}_3$ ,” *Phys. Rev. Lett.* **99** (2007). 25, 54, 98
- [103] A. Kalabukhov, Y. Boikov, I. Serenkov, V. Sakharov, V. Popok, R. Gunnarsson, J. Börjesson, N. Ljustina, E. Olsson, and D. Winkler, “Cationic Disorder and Phase Segregation in  $\text{LaAlO}_3/\text{SrTiO}_3$  Heterointerfaces Evidenced by Medium-Energy Ion Spectroscopy,” *Phys. Rev. Lett.* **103**, 146101 (2009). 25, 54, 98

## BIBLIOGRAPHY

---

- [104] F. Gunkel, S. Hoffmann-Eifert, R. Dittmann, S. Mi, C. Jia, P. Meuffels, and R. Waser, “High temperature conductance characteristics of  $\text{LaAlO}_3/\text{SrTiO}_3$ -heterostructures under equilibrium oxygen atmospheres,” *Appl. Phys. Lett.* **97**, 012103 (2010). 25
- [105] L. Qiao, T. Droubay, V. Shutthanandan, Z. Zhu, P. Sushko, and S. Chambers, “Thermodynamic instability at the stoichiometric  $\text{LaAlO}_3/\text{SrTiO}_3$  (001) interface,” *J. Phys.: Condens. Matter* **22**, 312201 (2010). 25, 54, 98
- [106] S. Chambers, M. Engelhard, V. Shutthanandan, Z. Zhu, T. Droubay, L. Qiao, P. Sushko, T. Feng, H. Lee, T. Gustafsson, E. Garfunkel, A. Shah, J. Zuo, and Q. Ramasse, “Instability, intermixing and electronic structure at the epitaxial  $\text{LaAlO}_3/\text{SrTiO}_3$  (001) heterojunction,” *Surf. Sci. Rep.* **65**, 317 (2010). 25
- [107] A. Kalabukhov, Y. Boikov, I. Serenkov, V. Sakharov, J. Börjesson, N. Ljustina, E. Olsson, D. Winkler, and T. Claeson, “Improved cationic stoichiometry and insulating behavior at the interface of  $\text{LaAlO}_3/\text{SrTiO}_3$  formed at high oxygen pressure during pulsed-laser deposition,” *EPL (Europhysics Letters)* **93**, 37001 (2011). 25
- [108] A. Ohtomo, D. Muller, J. Grazul, and H. Hwang, “Artificial charge-modulation in atomic-scale perovskite titanate superlattices,” *Nature* **419**, 378 (2002). 26
- [109] P. Perna, D. Maccariello, M. Radovic, U. Scotti di Uccio, I. Pallecchi, M. Codda, D. Marre, C. Cantoni, J. Gazquez, and M. Varela, “Conducting interfaces between band insulating oxides: The  $\text{LaGaO}_3/\text{SrTiO}_3$  heterostructure,” *Appl. Phys. Lett.* **97**, 152111 (2010). 26, 83
- [110] Y. Hotta, T. Susaki, and H. Hwang, “Polar Discontinuity Doping of the  $\text{LaVO}_3/\text{SrTiO}_3$  Interface,” *Phys. Rev. Lett.* **99**, 236805 (2007). 26

- [111] G. Singh-Bhalla, C. Bell, J. Ravichandran, W. Siemons, Y. Hikita, S. Salahuddin, A. Hebard, H. Hwang, and R. Ramesh, “Built-in and induced polarization across  $\text{LaAlO}_3/\text{SrTiO}_3$  heterojunctions,” *Nature Physics* **7**, 80 (2010). 27
- [112] P. Brinks, W. Siemons, J. Kleibeuker, G. Koster, G. Rijnders, and M. Huijben, “Anisotropic electrical transport properties of a two-dimensional electron gas at  $\text{SrTiO}_3$ - $\text{LaAlO}_3$  interfaces,” *Appl. Phys. Lett.* **98**, 242904 (2011). 29, 76, 83
- [113] T. Fix, F. Schoofs, Z. Bi, A. Chen, H. Wang, J. MacManus-Driscoll, and M. Blamire, “Influence of  $\text{SrTiO}_3$  substrate miscut angle on the transport properties of  $\text{LaAlO}_3/\text{SrTiO}_3$  interfaces,” *Appl. Phys. Lett.* **99**, 022103 (2011). 29, 76, 83
- [114] P. Ordejon, E. Artacho, and J. M. Soler, “Self-consistent order-N density-functional calculations for very large systems,” *Phys. Rev. B* **53**, 10441 (1996). 31, 35, 61, 77, 88, 90, 114
- [115] J. Soler, E. Artacho, J. Gale, A. Garcia, J. Junquera, P. Ordejon, and D. Sanchez-Portal, “The SIESTA method for ab initio order-N materials simulation,” *J. Phys.: Condens. Matter* **14**, 2745 (2002). 31, 34, 35, 61, 77, 88, 90, 114
- [116] R. Martin, *Electronic structure: basic theory and practical methods* (Cambridge Univ Pr, 2004). 31
- [117] M. Born and R. Oppenheimer, “On the quantum theory of molecules,” *Annalen der Physik* **84**, 457 (1927). 32
- [118] P. Hohenberg and W. Kohn, “Inhomogeneous electron gas,” *Phys. Rev.* **136**, B864 (1964). 32

## BIBLIOGRAPHY

---

- [119] W. Kohn and L. Sham, “Self-consistent equations including exchange and correlation effects,” *Phys. Rev.* **140**, A1133 (1965). 32, 33
- [120] A. Dal Corso, S. Baroni, R. Resta, and S. de Gironcoli, “Ab initio calculation of phonon dispersions in II-VI semiconductors,” *Phys. Rev. B* **47**, 3588 (1993). 33
- [121] A. Khein, D. Singh, and C. Umrigar, “All-electron study of gradient corrections to the local-density functional in metallic systems,” *Phys. Rev. B* **51**, 4105 (1995). 33
- [122] M. Payne, M. Teter, D. Allan, T. Arias, and J. Joannopoulos, “Iterative minimization techniques for ab initio total-energy calculations: molecular dynamics and conjugate gradients,” *Reviews of Modern Physics* **64**, 1045 (1992). 34, 38
- [123] H. Monkhorst and J. Pack, “Special points for Brillouin-zone integrations,” *Phys. Rev. B* **13**, 5188 (1976). 34
- [124] J. F. Janak, “Proof that  $\frac{\partial E}{\partial n_i} = \epsilon$  in density-functional theory,” *Phys. Rev. B* **18**, 7165 (1978). 34
- [125] O. Sankey and D. Niklewski, “Abinitio multicenter tight-binding model for molecular-dynamics simulations and other applications in covalent systems,” *Phys. Rev. B* **40**, 3979 (1989). 35
- [126] J. Junquera, Ó. Paz, D. Sánchez-Portal, and E. Artacho, “Numerical atomic orbitals for linear-scaling calculations,” *Phys. Rev. B* **64**, 235111 (2001). 35
- [127] N. Troullier and J. Martins, “Efficient pseudopotentials for plane-wave calculations,” *Phys. Rev. B* **43**, 1993 (1991). 36, 61, 90
- [128] S. Louie, S. Froyen, and M. Cohen, “Nonlinear ionic pseudopotentials in spin-density-functional calculations,” *Phys. Rev. B* **26**, 1738 (1982). 36

## BIBLIOGRAPHY

---

- [129] H. Hellmann, “Einführung in die Quantumchemie,” *Franz Deutsche, Leipzig* (1937). 38
- [130] R. Feynman, “Forces in molecules,” *Phys. Rev.* **56**, 340 (1939). 38
- [131] P. Pulay, “Ab initio calculation of force constants and equilibrium geometries in polyatomic molecules,” *Mol. Phys.* **17**, 197 (1969). 38
- [132] M. Posternak, R. Resta, and A. Baldereschi, “Role of covalent bonding in the polarization of perovskite oxides: The case of  $\text{KNbO}_3$ ,” *Phys. Rev. B* **50**, 8911 (1994). 39
- [133] R. M. Martin, “Comment on calculations of electric polarization in crystals,” *Phys. Rev. B* **9**, 1998 (1974). 39, 49
- [134] R. Resta, “Theory of the electric polarization in crystals,” *Ferroelectrics* **136**, 51 (1992). 40, 42
- [135] R. D. King-Smith and D. Vanderbilt, “Theory of polarization of crystalline solids,” *Phys. Rev. B* **47**, 1651 (1993). 40, 41, 42, 50, 51, 67, 76, 88
- [136] R. Resta, “Macroscopic polarization in crystalline dielectrics: the geometric phase approach,” *Rev. Mod. Phys.* **66**, 899 (1994). 40, 50, 76, 88
- [137] M. Berry, “Quantal phase factors accompanying adiabatic changes,” *Proceedings of the Royal Society of London. A. Mathematical and Physical Sciences* **392**, 45 (1984). 41
- [138] N. Marzari and D. Vanderbilt, “Maximally localized generalized Wannier functions for composite energy bands,” *Phys. Rev. B* **56**, 12847 (1997). 42, 47, 50, 51, 76, 88
- [139] E. Blount, “Formalisms of band theory,” *Solid State Physics* **13**, 305 (1962). 42

## BIBLIOGRAPHY

---

- [140] N. Bristowe, E. Artacho, and P. Littlewood, “Oxide superlattices with alternating p and n interfaces,” *Phys. Rev. B* **80**, 045425 (2009). 47, 48, 59, 69, 76, 77, 80, 83, 93, 98, 101, 108
- [141] M. Stengel and D. Vanderbilt, “Berry-phase theory of polar discontinuities at oxide-oxide interfaces,” *Phys. Rev. B* **80**, 241103 (2009). 47, 49, 50, 51, 52, 74, 88, 91, 98, 101
- [142] G. A. Baraff, J. A. Appelbaum, and D. R. Hamann, “Self-consistent calculation of the electronic structure at an abrupt GaAs-Ge interface,” *Phys. Rev. Lett.* **38**, 237 (1977). 47, 51, 68
- [143] A. Baldereschi, S. Baroni, and R. Resta, “Band offsets in lattice-matched heterojunctions - a model and 1st principles calculations for GaAs/AlAs,” *Phys. Rev. Lett.* **61**, 734 (1988). 48, 62, 64
- [144] X. Wu, M. Stengel, K. M. Rabe, and D. Vanderbilt, “Predicting polarization and nonlinear dielectric response of arbitrary perovskite superlattice sequences,” *Phys. Rev. Lett.* **101**, 087601 (2008). 48
- [145] É. Murray and D. Vanderbilt, “Theoretical investigation of polarization-compensated II-IV/IV perovskite superlattices,” *Phys. Rev. B* **79**, 100102 (2009). 48, 76
- [146] M. Finnis, “Accessing the excess: an atomistic approach to excesses at planar defects and dislocations in ordered compounds,” *Physica status solidi (a)* **166**, 397 (1998). 49
- [147] W. Frensley and H. Kroemer, “Theory of the energy-band lineup at an abrupt semiconductor heterojunction,” *Phys. Rev. B* **16**, 2642 (1977). 51, 53
- [148] N. C. Bristowe, P. B. Littlewood, and E. Artacho, “Surface defects and con-

- duction in polar oxide heterostructures,” *Phys. Rev. B* **83**, 205405 (2011).  
57, 74, 77, 83, 95, 97, 112, 119
- [149] P. B. Littlewood and X. Zhu, “Possibilities for exciton condensation in semiconductor quantum-well structures,” *Physica Scripta* **T68**, 56 (1996).  
60, 71
- [150] M. S. Park, S. H. Rhim, and A. J. Freeman, “Charge compensation and mixed valency in LaAlO<sub>3</sub>/SrTiO<sub>3</sub> heterointerfaces studied by the FLAPW method,” *Phys. Rev. B* **74**, 205416 (2006). 61
- [151] D. Ceperley and B. Alder, “Ground state of the electron gas by a stochastic method,” *Phys. Rev. Lett.* **45**, 566 (1980). 61
- [152] E. Anglada, J. M. Soler, J. Junquera, and E. Artacho, “Systematic generation of finite-range atomic basis sets for linear-scaling calculations,” *Phys. Rev. B* **66**, 205101 (2002). 61, 90
- [153] J. Moreno and J. M. Soler, “Optimal meshes for integrals in real- and reciprocal-space unit cells,” *Phys. Rev. B* **45**, 13891 (1992). 61
- [154] J. M. Albina, M. Mrovec, B. Meyer, and C. Elsaesser, “Structure, stability, and electronic properties of SrTiO<sub>3</sub>/LaAlO<sub>3</sub> and SrTiO<sub>3</sub>/SrRuO<sub>3</sub> interfaces,” *Phys. Rev. B* **76**, 165103 (2007). 61
- [155] P. Larson, Z. S. Popovic, and S. Satpathy, “Lattice relaxation effects on the interface electron states in the perovskite oxide heterostructures: LaTiO<sub>3</sub> monolayer embedded in SrTiO<sub>3</sub>,” *Phys. Rev. B* **77**, 245122 (2008). 61
- [156] R. Pentcheva and W. E. Pickett, “Ionic relaxation contribution to the electronic reconstruction at the n-type LaAlO<sub>3</sub>/SrTiO<sub>3</sub> interface,” *Phys. Rev. B* **78**, 205106 (2008). 61

## BIBLIOGRAPHY

---

- [157] M. Stengel, P. Aguado-Puente, N. A. Spaldin, and J. Junquera, “Band alignment at metal/ferroelectric interfaces: Insights and artifacts from first principles,” *Phys. Rev. B* **83**, 235112 (2011). 62, 124, 127
- [158] Z. Popovic and S. Satpathy, “Wedge-shaped potential and airy-function electron localization in oxide superlattices,” *Phys. Rev. Lett* **94**, 176805 (2005). 62
- [159] L. Sham and M. Schlüter, “Density-functional theory of the energy gap,” *Phys. Rev. Lett.* **51**, 1888 (1983). 62
- [160] Q. Wu and T. Van Voorhis, “Direct calculation of electron transfer parameters through constrained density functional theory,” *J. Phys. Chem. A* **110**, 9212 (2006). 62
- [161] S. Kang and H. Ishiwara, “Characteristics of LaAlO<sub>3</sub> as Insulating Buffer Layers of Ferroelectric-Gate Field Effect Transistors,” *Japanese journal of applied physics* **41**, 6899 (2002). 65
- [162] B. Hung, K. Chiang, C. Huang, A. Chin, and S. McAlister, “High-performance poly-silicon TFTs incorporating LaAlO<sub>3</sub> as the gate dielectric,” *Electron Device Letters, IEEE* **26**, 384 (2005). 65
- [163] J. Haeni, P. Irvin, W. Chang, R. Uecker, P. Reiche, Y. Li, S. Choudhury, W. Tian, M. Hawley, B. Craigo, A. Tagantsev, X. Pan, S. Streiffer, L. Chen, S. Kirchoefer, J. Levy, and D. Schlom, “Room-temperature ferroelectricity in strained SrTiO<sub>3</sub>,” *Nature* **430**, 758 (2004). 67
- [164] A. Antons, J. Neaton, K. Rabe, and D. Vanderbilt, “Structure, structural phase transitions, mechanical properties, defects - tunability of the dielectric response of epitaxially strained SrTiO<sub>3</sub> from first principles,” *Phys. Rev. B* **71**, 24102 (2005). 67

- [165] D. Fernandez-Torre, R. Escribano, T. Archer, J. Pruneda, and E. Artacho, “First-principles infrared spectrum of nitric acid and nitric acid monohydrate crystals,” *J Phys Chem A* **108**, 10535 (2004). 67
- [166] W. Zhong, R. Kingsmith, and D. Vanderbilt, “Giant LO-TO splittings in perovskite ferroelectrics,” *Phys. Rev. Lett.* **72**, 3618 (1994). 67
- [167] P. Delugas, V. Fiorentini, and A. Filippetti, “Dielectric properties and long-wavelength optical modes of the high- $\kappa$  oxide LaAlO<sub>3</sub>,” *Phys. Rev. B* **71**, 134302 (2005). 67, 109
- [168] C. Bark, D. Felker, Y. Wang, Y. Zhang, H. Jang, C. Folkman, J. Park, S. Baek, H. Zhou, and D. Fong, “Tailoring a two-dimensional electron gas at the LaAlO<sub>3</sub>/SrTiO<sub>3</sub> (001) interface by epitaxial strain,” *Proceedings of the National Academy of Sciences* **108**, 4720 (2011). 69, 83
- [169] N. C. Bristowe, T. Fix, M. G. Blamire, P. B. Littlewood, and E. Artacho, “Proposal of a One-Dimensional Electron Gas in the Steps at the LaAlO<sub>3</sub>–SrTiO<sub>3</sub> Interface,” *Phys. Rev. Lett.* **108**, 166802 (2012). 73
- [170] Y. Xie, Y. Hikita, C. Bell, and H. Hwang, “Control of electronic conduction at an oxide heterointerface using surface polar adsorbates,” *Nature Communications* **2**, 494 (2011). 74
- [171] P. Irvin, Y. Ma, D. Bogorin, C. Cen, C. Bark, C. Folkman, C. Eom, and J. Levy, “Rewritable nanoscale oxide photodetector,” *Nature Photonics* **4**, 849 (2010). 74
- [172] Z. Wu and R. Cohen, “More accurate generalized gradient approximation for solids,” *Phys. Rev. B* **73**, 235116 (2006). 77, 114
- [173] K. Novoselov, A. Geim, S. Morozov, D. Jiang, Y. Zhang, S. Dubonos, I. Grigorieva, and A. Firsov, “Electric field effect in atomically thin carbon films,” *Science* **306**, 666 (2004). 86

## BIBLIOGRAPHY

---

- [174] K. Novoselov, D. Jiang, F. Schedin, T. Booth, V. Khotkevich, S. Morozov, and A. Geim, “Two-dimensional atomic crystals,” *Proc. Natl. Acad. Sci. U. S. A.* **102**, 10451 (2005). 86
- [175] D. Pacilé, J. C. Meyer, C. O. Girit, and A. Zettl, “The two-dimensional phase of boron nitride: Few-atomic-layer sheets and suspended membranes,” *Appl. Phys. Lett.* **92**, 133107 (2008). 86
- [176] M. Osada and T. Sasaki, “Exfoliated oxide nanosheets: new solution to nanoelectronics,” *J. Mater. Chem.* **19**, 2503 (2009). 86
- [177] C. Lee, H. Yan, L. E. Brus, T. F. Heinz, J. Hone, and S. Ryu, “Anomalous Lattice Vibrations of Single- and Few-Layer MoS<sub>2</sub>,” *ACS Nano* **4**, 2695 (2010). 86
- [178] J. C. Coleman, M. Lotya, A. O’Neill, S. D. Bergin, P. J. King, U. Khan, K. Young, A. Gaucher, S. De, R. J. Smith, I. V. Shvets, S. K. Arora, G. Stanton, H.-Y. Kim, K. Lee, G. T. Kim, G. S. Duesberg, T. Hallam, J. J. Boland, J. J. Wang, J. F. Donegan, J. C. Grunlan, G. Moriarty, A. Shmeliov, R. J. Nichols, J. M. Perkins, E. M. G. K. Theuwissen, D. W. McComb, P. D. Nellist, and V. Nicolosi, “Two-dimensional nanosheets produced by liquid exfoliation of layered materials,” *Science* **331**, 568 (2011). 86
- [179] D. Teweldebrhan, V. Goyal, M. Rahman, and A. A. Balandin, “Atomically-thin crystalline films and ribbons of bismuth telluride,” *Appl. Phys. Lett.* **96**, 053107 (2010). 86
- [180] L. Ci, L. Song, C. Jin, D. Jariwala, D. Wu, Y. Li, A. Srivastava, Z. F. Wang, K. Storr, L. Balicas, F. Liu, and P. M. Ajayan, “Atomic layers of hybridized boron nitride and graphene domains,” *Nat. Mater.* **9**, 430 (2010). 86
- [181] C. R. Dean, A. F. Young, I. Meric, C. Lee, L. Wang, S. Sorgenfrei, K. Watanabe, T. Taniguchi, P. Kim, K. L. Shepard, and J. Hone, “Boron

- nitride substrates for high-quality graphene electronics,” *Nat. Nano* **5**, 722 (2010). 86
- [182] M. Kawaguchi, “B/C/N materials based on the graphite network,” *Advanced Materials* **9**, 615 (1997). 86
- [183] M. Cañas-Ventura, W. Xiao, D. Wasserfallen, K. Müllen, H. Brune, J. Barth, and R. Fasel, “Self-Assembly of Periodic Bicomponent Wires and Ribbons,” *Angewandte Chemie International Edition* **46**, 1814 (2007). 86
- [184] J. Zhang, J. Jiang, and X. S. Zhao, “Synthesis and Capacitive Properties of Manganese Oxide Nanosheets Dispersed on Functionalized Graphene Sheets,” *J. Phys. Chem. C* **115**, 6448 (2011). 86
- [185] J. Goniakowski, C. Noguera, and L. Giordano, “Using polarity for engineering oxide nanostructures: structural phase diagram in free and supported MgO (111) ultrathin films,” *Phys. Rev. Lett.* **93**, 215702 (2004). 86
- [186] C. Freeman, F. Claeysens, N. Allan, and J. Harding, “Graphitic nanofilms as precursors to wurtzite films: Theory,” *Phys. Rev. Lett.* **96**, 66102 (2006). 86, 87
- [187] C. Tusche, H. Meyerheim, and J. Kirschner, “Observation of depolarized ZnO (0001) monolayers: Formation of unreconstructed planar sheets,” *Phys. Rev. Lett.* **99**, 26102 (2007). 86
- [188] H. Şahin, S. Cahangirov, M. Topsakal, E. Bekaroglu, E. Akturk, R. Senger, and S. Ciraci, “Monolayer honeycomb structures of group-IV elements and III-V binary compounds: First-principles calculations,” *Phys. Rev. B* **80**, 155453 (2009). 87
- [189] M. Topsakal, S. Cahangirov, E. Bekaroglu, and S. Ciraci, “First-principles

## BIBLIOGRAPHY

---

- study of zinc oxide honeycomb structures,” *Phys. Rev. B* **80**, 235119 (2009). 87
- [190] A. Mostofi, J. Yates, Y. Lee, I. Souza, D. Vanderbilt, and N. Marzari, “wannier90: A tool for obtaining maximally-localised Wannier functions,” *Comput. Phys. Commun.* **178**, 685 (2008). 88
- [191] J. Perdew, K. Burke, and M. Ernzerhof, “Generalized gradient approximation made simple,” *Phys. Rev. Lett.* **77**, 3865 (1996). 90, 114
- [192] M. Fujita, K. Wakabayashi, K. Nakada, and K. Kusakabe, “Peculiar localized state at zigzag graphite edge,” *J. Phys. Soc. Jpn.* **65**, 1920 (1996). 93, 94
- [193] F. Zheng, G. Zhou, Z. Liu, J. Wu, W. Duan, B. Gu, and S. Zhang, “Half metallicity along the edge of zigzag boron nitride nanoribbons,” *Phys. Rev. B* **78**, 205415 (2008). 94
- [194] Q. Chen, L. Zhu, and J. Wang, “Edge-passivation induced half-metallicity of zigzag zinc oxide nanoribbons,” *Appl. Phys. Lett.* **95**, 133116 (2009). 94
- [195] J. Pruneda, “Origin of half-semimetallicity induced at interfaces of C-BN heterostructures,” *Phys. Rev. B* **81**, 161409 (2010). 94
- [196] M. Wu, Z. Zhang, and X. Zeng, “Charge-injection induced magnetism and half metallicity in single-layer hexagonal group III/V (BN, BP, AlN, AlP) systems,” *Appl. Phys. Lett.* **97**, 093109 (2010). 94
- [197] V. Barone and J. Peralta, “Magnetic boron nitride nanoribbons with tunable electronic properties,” *Nano Lett.* **8**, 2210 (2008). 94
- [198] S. Bhowmick, A. Singh, and B. Yakobson, “Quantum Dots and Nanoroads of Graphene Embedded in Hexagonal Boron Nitride,” *Journal of Physical Chemistry C* **115**, 9889 (2011). 94

## BIBLIOGRAPHY

---

- [199] H. Takagi and H. Hwang, “An Emergent Change of Phase for Electronics,” *Science* **327**, 1601 (2010). 98
- [200] Y. Li, S. Phattalung, S. Limpijumnong, and J. Yu, “Oxygen-vacancy-induced charge carrier in n-type interface of LaAlO<sub>3</sub> overlayer on SrTiO<sub>3</sub> (001): interface vs bulk doping carrier,” *Arxiv preprint arXiv:0912.4805* (2009). 98, 99, 103, 104, 109
- [201] Z. Zhong, P. Xu, and P. Kelly, “Polarity-induced oxygen vacancies at LaAlO<sub>3</sub>/SrTiO<sub>3</sub> interfaces,” *Phys. Rev. B* **82**, 165127 (2010). 98, 99
- [202] L. Zhang, X. Zhou, H. Wang, J. Xu, J. Li, E. Wang, and S. Wei, “Origin of insulating behavior of the p-type LaAlO<sub>3</sub>/SrTiO<sub>3</sub> interface: Polarization-induced asymmetric distribution of oxygen vacancies,” *Phys. Rev. B* **82**, 125412 (2010). 98, 99, 103
- [203] W. J. Son, E. Cho, J. Lee, and S. Han, “Hydrogen adsorption and carrier generation in LaAlO<sub>3</sub>/SrTiO<sub>3</sub> heterointerfaces: a first-principles study,” *J. Phys.: Condens. Matter* **22**, 315501 (2010). 99
- [204] R. Anez, A. Sierraalta, G. Martorell, and P. Sautet, “Stabilization of the (110) tetragonal zirconia surface by hydroxyl chemical transformation,” *Surf. Sci.* **603**, 25262531 (2009). 99
- [205] N. C. Bristowe, P. B. Littlewood, and E. Artacho, *in preparation* (2012). 103
- [206] J. Krupka, R. Geyer, M. Kuhn, and J. Hinken, “Dielectric Properties of Single Crystals of Al<sub>2</sub>O<sub>3</sub>, LaAlO<sub>3</sub>, NdGaO<sub>3</sub>, SrTiO<sub>3</sub>, and MgO at Cryogenic Temperatures,” *IEEE Trans. Microwave Theory Tech.* **42**, 2418 (1994). 105
- [207] V. Popok, A. Kalabukhov, R. Gunnarsson, S. Lemeshko, T. Claeson, and D. Winkler, “Kelvin Probe Force Microscopy Study of LaAlO<sub>3</sub>/SrTiO<sub>3</sub>

## BIBLIOGRAPHY

---

- Heterointerfaces,” *Journal of Advanced Microscopy Research* **5**, 26 (2010). 107
- [208] T. Jin-Long, Z. Jun, Q. Wen-Feng, X. Jie, and L. Yan-Rong, “Ab initio study of oxygen-vacancy  $\text{LaAlO}_3$  (001) surface,” *Chinese Physics B* **17**, 655 (2008). 109
- [209] C. Persson, Y. Zhao, S. Lany, and A. Zunger, “n-type doping of  $\text{CuInSe}_2$  and  $\text{CuGaSe}_2$ ,” *Phys. Rev. B* **72**, 35211 (2005). 110
- [210] P. Deák, B. Aradi, T. Frauenheim, and A. Gali, “Challenges for ab initio defect modeling,” *Materials Science and Engineering: B* **154**, 187 (2008). 110, 118
- [211] K. Xiong, J. Robertson, and S. Clark, “Electronic defects in  $\text{LaAlO}_3$ ,” *Microelectron. Eng.* **85**, 65 (2008). 110
- [212] N. Bristowe, M. Stengel, P. Littlewood, J. Pruneda, and E. Artacho, “Electrochemical ferroelectric switching: Origin of polarization reversal in ultrathin films,” *Phys. Rev. B* **85**, 024106 (2012). 111
- [213] V. Fridkin, *Ferroelectric semiconductors* (Consultants Bureau, 1980). 112
- [214] V. Ferrari, J. Pruneda, and E. Artacho, “Density functionals and half-metallicity in  $\text{La}_{2/3}\text{Sr}_{1/3}\text{MnO}_3$ ,” *Physica Status Solidi (a)* **203**, 1437 (2006). 114
- [215] J. Junquera, M. Zimmer, P. Ordejon, and P. Ghosez, “First-principles calculation of the band offset at  $\text{BaO}/\text{BaTiO}_3$  and  $\text{SrO}/\text{SrTiO}_3$  interfaces,” *Phys. Rev. B* **67** (2003). 114
- [216] J. Pruneda, V. Ferrari, R. Rurali, P. Littlewood, N. Spaldin, and E. Artacho, “Ferrodistortive instability at the (001) surface of half-metallic manganites,” *Phys. Rev. Lett.* **99**, 226101 (2007). 114

- [217] J. Padilla and D. Vanderbilt, “Ab initio study of BaTiO<sub>3</sub> surfaces,” *Phys. Rev. B* **56**, 1625 (1997). 116
- [218] E. Heifets, S. Dorfman, D. Fuks, and E. Kotomin, “Atomistic simulation of the [001] surface structure in BaTiO<sub>3</sub>,” *Thin Solid Films* **296**, 76 (1997). 116
- [219] G. B. Stephenson and M. J. Highland, “Equilibrium and stability of polarization in ultrathin ferroelectric films with ionic surface compensation,” *Phys. Rev. B* **84**, 064107 (2011). 117, 119
- [220] M. Finnis, A. Lozovoi, and A. Alavi, “THE OXIDATION OF NIAL: What Can We Learn from Ab Initio Calculations?,” *Annu. Rev. Mater. Res.* **35**, 167 (2005). 118
- [221] S. Kalinin, S. Jesse, A. Tselev, A. Baddorf, and N. Balke, “The Role of Electrochemical Phenomena in Scanning Probe Microscopy of Ferroelectric Thin Films,” *ACS nano* **5**, 5683 (2011). 118
- [222] R. Waser, R. Dittmann, G. Staikov, and K. Szot, “Redox-Based Resistive Switching Memories—Nanoionic Mechanisms, Prospects, and Challenges,” *Advanced Materials* **21**, 2632 (2009). 118
- [223] A. Morozovska, E. Eliseev, S. Svechnikov, A. Krutov, V. Shur, A. Borisevich, P. Maksymovych, and S. Kalinin, “Finite size and intrinsic field effect on the polar-active properties of ferroelectric-semiconductor heterostructures,” *Phys. Rev. B* **81**, 205308 (2010). 119
- [224] S. Kalinin and D. Bonnell, “Screening phenomena on oxide surfaces and its implications for local electrostatic and transport measurements,” *Nano Lett.* **4**, 555 (2004). 119
- [225] J. Rondinelli, M. Stengel, and N. Spaldin, “Carrier-mediated magnetoelec-

## BIBLIOGRAPHY

---

- tricity in complex oxide heterostructures,” *Nature Nanotechnology* **3**, 46 (2007). 121
- [226] J. D. Burton and E. Y. Tsymbal, “Prediction of electrically induced magnetic reconstruction at the manganite/ferroelectric interface,” *Phys. Rev. B* **80**, 174406 (2009). 121
- [227] C. A. F. Vaz, J. Hoffman, Y. Segal, J. W. Reiner, R. D. Grober, Z. Zhang, C. H. Ahn, and F. J. Walker, “Origin of the Magnetoelectric Coupling Effect in  $Pb(Zr_{0.2}Ti_{0.8})O_3/La_{0.8}Sr_{0.2}MnO_3$  Multiferroic Heterostructures,” *Phys. Rev. Lett.* **104**, 127202 (2010). 121
- [228] H. Molegraaf, J. Hoffman, C. Vaz, S. Gariglio, D. van der Marel, C. Ahn, and J. Triscone, “Magnetoelectric Effects in Complex Oxides with Competing Ground States,” *Advanced Materials* **21**, 3470 (2009). 121
- [229] J. Park, E. Vescovo, H. Kim, C. Kwon, R. Ramesh, and T. Venkatesan, “Magnetic Properties at Surface Boundary of a Half-Metallic Ferromagnet  $La_{0.7}Sr_{0.3}MnO_3$ ,” *Phys. Rev. Lett.* **81**, 1953 (1998). 121
- [230] A. Gruverman, D. Wu, H. Lu, Y. Wang, H. Jang, C. Folkman, M. Zhuravlev, D. Felker, M. Rzchowski, and C. Eom, “Tunneling electroresistance effect in ferroelectric tunnel junctions at the nanoscale,” *Nano Lett.* **9**, 3539 (2009). 121, 122, 123
- [231] J. Junquera and P. Ghosez, “Critical thickness for ferroelectricity in perovskite ultrathin films,” *Nature* **422**, 506 (2003). 121
- [232] M. Zhuravlev, R. Sabirianov, S. Jaswal, and E. Tsymbal, “Giant electroresistance in ferroelectric tunnel junctions,” *Phys. Rev. Lett.* **94**, 246802 (2005). 121
- [233] H. Kohlstedt, N. Pertsev, J. Rodríguez Contreras, and R. Waser, “Theoret-

- ical current-voltage characteristics of ferroelectric tunnel junctions,” *Phys. Rev. B* **72**, 125341 (2005). 121
- [234] C.-L. Wu, P.-W. Lee, Y.-C. Chen, L.-Y. Chang, C.-H. Chen, C.-W. Liang, P. Yu, Q. He, R. Ramesh, and Y.-H. Chu, “Direct spectroscopic evidence of charge reversal at the  $\text{Pb}(\text{Zr}_{0.2}\text{Ti}_{0.8})\text{O}_3/\text{La}_{0.7}\text{Sr}_{0.3}\text{MnO}_3$  heterointerface,” *Phys. Rev. B* **83**, 020103 (2011). 123
- [235] S. Nonnenmann, E. Gallo, and J. Spanier, “Redox-based resistive switching in ferroelectric perovskite nanotubes,” *Appl. Phys. Lett.* **97**, 102904 (2010). 123
- [236] C. Jia, S. Mi, M. Faley, U. Poppe, J. Schubert, and K. Urban, “Oxygen octahedron reconstruction in the  $\text{SrTiO}_3/\text{LaAlO}_3$  heterointerfaces investigated using aberration-corrected ultrahigh-resolution transmission electron microscopy,” *Phys. Rev. B* **79**, 081405 (2009). 131